Spring 1-1-2013

Impact of Strain Rate on the Shear Strength and Excess Pore Water Pressure Generation of Clays and Sands

Jenna S. Svoboda
University of Colorado at Boulder, jsvoboda77@gmail.com

IMPACT OF STRAIN RATE ON THE SHEAR STRENGTH AND PORE WATER PRESSURE GENERATION OF CLAYS AND SANDS

by

Jenna Svoboda

B.S., Oregon State University

A thesis submitted to the

Faculty of the Graduate School of the

University of Colorado in partial fulfillment

of the requirement for the degree of

Master of Science

Department of Civil, Environmental, and Architectural Engineering

2013

This thesis entitled:

Impact of Strain Rate on the Shear Strength and

Pore Water Pressure Generation of Clays and Sands

written by Jenna Svoboda

has been approved by the Department of Civil, Environmental, and Architectural Engineering

_____

Professor John McCartney (committee chair)

_____

Professor Richard Regueiro

_____

Professor Ronald Pak

Date_____

The final copy of this thesis has been examined by the signatories, and we find that both the content and the form meet the acceptable presentation standards of scholarly work in the above mentioned discipline.

Jenna Svoboda (M.S. Civil Engineering, Department of Civil, Environmental, and Architectural Engineering)

Impact of Strain Rate on the Shear Strength and Pore Water Pressure Generation of Clays and Sands

Thesis directed by Professor John S. McCartney

Abstract

The purpose of this study was to investigate changes in shear strength and excess pore water pressure of unsaturated clay and dense sand subject to increased strain rates. Consolidated undrained (CU) and unconsolidated undrained (UU) triaxial compression tests were performed on specimens of compacted clay performed at axial strain rates ranging from 0.1 %/min to 14.5 %/min at degrees of saturation ranging from 100% to 75%. In addition, CU tests were performed on saturated, dense sand at axial strain rates ranging between 1.1 %/min and 220 %/min, and consolidated drained (CD) tests were performed on oven-dry sand at axial strain rates ranging from 1.1 %/min to 4.4 %/min.

Results from the CU tests on saturated clay (degree of saturation equal to 100 %) show an increase in undrained shear strength of 13.8% and a decrease in the magnitude of positive excess pore water pressure with increasing axial strain rate. These findings are consistent with results from classic studies on normally consolidated soils by Casagrande and Shannon (1948) and Richardson and Whitman (1963) as well as compacted soils by Olson and Parola (1967). The undrained shear strength of unsaturated compacted clay also increases with increasing axial strain rate as well as increases in matric suction. However, the excess pore water pressure at failure measured for unsaturated tests at a higher strain rate first increased from the saturated value at a low suction and then decreased at a higher suction (lower degree of saturation). The

rate of increase in the shear strength of unsaturated clays having suction values up to 140 kPa (degrees of saturation greater than 75%) was found to be less than that of the clay under saturated conditions. UU tests on compacted clay at different initial compaction water contents confirms the trend of shear strength increase with increased strain rate and lower degree of saturation. Overall, the results from these tests support the hypothesis that rate effects in clays occur due to the difference in the hydraulic conductivity of the soil, which affects the rate of drainage of excess pore water pressure, and the axial strain rate, which affects the rate of generation of excess pore water pressure. The difference in these two rate effects leads to a decrease in the positive excess pore water pressure at failure for faster axial strain rates, which causes the effective stress to increase within an undrained clay specimen.

The results from the CU tests on saturated sand show an increase of 33% in undrained shear strength and a decrease in the magnitude of negative pore water pressure at failure with increasing axial strain rate. However, CD tests performed on dry sand indicate that the shear strength at failure does not change with increasing axial strain rate. These observations indicate that the rate effect in saturated dense sand likely occurs due to an increase in the amount of dilation with increasing axial strain rate, which affects the magnitude of negative pore water pressure. Similar to the clay specimens, the lower magnitude of negative excess pore water pressure at failure at faster axial strain rates leads to an increase in effective stress in an undrained sand specimen.

Acknowledgements:

I would like to express with my greatest regard and gratitude to Professor John McCartney for his guidance and patience through my research endeavors during these last two years of work at the University of Colorado Boulder. I would also like to thank the Office of Naval Research for the funding provided through the grant N00014-11-1-0691. This funding is gratefully acknowledged.

Table of Contents:

List of Figures:

List of Tables

1.0 Introduction

Soil specimens are usually sheared in triaxial compression tests at axial strain rates intended to ensure that excess pore water pressures generated due to shearing will dissipate at a steady rate in the case of consolidated-drained tests (Gibson and Henkel 1954; ASTM D7181) or to ensure enough time for pore water pressures to equilibrate throughout a specimen in the case of consolidated-undrained tests (ASTM D4767). These rates are generally quite slow, ranging from tens of minutes to months depending on the soil type, and are slower in the case of consolidated-drained tests than in consolidated-undrained tests. The reason behind selecting these axial strain rates is so that the shear strength values measured in a triaxial compression test with either drainage condition can be interpreted such that they correspond to "effective" or fully-drained conditions. In fully-drained conditions, the shear strength of soils arises primarily from friction where the magnitude of shear strength depends on the effective stress state. In this case, the shear strength parameters that describe the change in shear strength with effective stress are referred to as the effective shear strength parameters.

In field applications, fully-drained conditions are usually expected in the long-term or during very slow loading. It is acknowledged that fully-drained conditions are not always encountered in the field, in which case the loading conditions are referred to as undrained conditions. Examples of undrained loading include rapid excavation, rapid application of a surcharge, earthquake loading, blast loading, or penetration of a projectile. During undrained loading, the excess pore water pressure generated during shearing affects the effective stress within a soil element, leading to a change in shear strength depending on the sign of excess pore water pressures (positive for contractive specimens and negative for dilative specimens). The evolution of shear strength during undrained loading can be interpreted using effective stress parameters if

the pore water pressure is known. Alternatively, a shear strength value referred to as the undrained shear strength can be defined, which depends on the soil structure and excess pore water pressure generation (not the effective stress state). An important issue that has been evaluated in the classic studies of Casagrande and Shannon (1948), Richardson and Whitman (1963), and Olson and Parola (1967) is whether or not the magnitude of excess pore water pressure during shearing affects the undrained shear strength of soils subjected to different elevated strain rates.

The over-arching goal of this study is to evaluate the role of increased axial strain rates on the undrained shear strength and excess pore water pressure during consolidated-undrained triaxial compression tests on a clay and a sand in saturated and unsaturated conditions. The undrained shear strength, excess pore water pressure, and the effective shear strength properties from consolidated undrained (CU) triaxial tests on saturated clay and sand were compared to CU triaxial compression tests with conventional loading rates in order to determine the rate effect mechanisms. Rate effects were also evaluated on dry sand specimens in consolidated drained (CD) triaxial compression tests to further investigate the role of excess pore water pressure generation for sand. Similarly, CU test were performed on unsaturated clay at a constant net stress under different matric suctions. The undrained shear strength and excess pore water pressure from the unsaturated clay tests were then compared to the saturated clay test results run at the same strain rates. Unsaturated clay specimens prepared using different compaction water contents were also evaluated in unconsolidated-undrained (UU) triaxial compression to evaluate the roles of initial suction and soil structure imposed by compaction.

A summary of the results from previous studies on cohesive and cohesionless soils in triaxial compression performed at different strain rates is presented in Chapter 2 of this thesis. The

results were discussed to identify gaps in the literature and to synthesize the rate effect mechanisms noted for different soil types. The material characteristics for the two soils evaluated in this study are presented in Chapter 3. A detailed description of the testing apparatuses used is given in Chapter 4. The testing procedures and results from tests at quasi static and intermediate strain rates for the sand and clay are provided in Chapters 5 and 6. The analysis for both soils is given in Chapter 7. A summary of the conclusions from this investigation are presented in Chapter 8.

2.0 Background

2.1 Overview

An overview of the results from previous studies focused on the effect of strain rate on the shear strength of soils is presented in this chapter. The first section of this chapter focuses on studies performed on cohesive soils, and includes a summary of the results to identify common trends amongst the studies. The second section of this chapter focuses on studies performed on cohesionless soils, and also includes a summary of the results to identify common trends. The third section of this chapter includes a synthesis of the different rate effect mechanisms for different soil types.

2.2 Strain Rate Effects on Cohesive Soils

2.2.1 Review of Previous Studies on Cohesive Soils

Casagrande and Shannon (1948) were the first to develop testing apparatuses and procedures to investigate the effects of increased strain rate on the shear strength of cohesive soils. Specimens of three different clays, Cambridge clay, Boston clay and Stockton clay, were tested in either unconfined compression (UC), unconsolidated undrained (UU) compression, or consolidated undrained (CU) triaxial compression tests. Cambridge clay is a medium soft clay with liquid limits ranging from 44 to 59 and plastic limits ranging from 21 to 27. Boston Clay is similar to the Cambridge clay but with average liquid and plastic limits of 42 and 20. Stockton Clay is a stiff clay from a nearly saturated compacted fill with liquid limit of 62 and plastic limit of 22. Their paper did not indicate if the CU triaxial samples were saturated before consolidation or not, although the common practice for CU tests at the time was to use back-pressure saturation. Times to failure were defined in this study as the time required to reach a certain magnitude of axial strain (typically 7%), and ranged from 0.02 seconds for the fastest rate to 300 seconds for the slowest rate.

The test results for all three clays showed an increase in undrained shear strength with decreasing time to failure. Typical relationships between undrained shear strength (quantified as the principal stress difference at failure) and the logarithm of time to failure from Casagrande and Shannon (1948) for the three clays is shown in Figure 2.1. The data shown in Figure 2.1 suggests that the undrained shear strength at failure, defined using the maximum principal stress difference, increases at approximately 10% per log cycle of time to failure. Although excess pore water pressure was not measured during testing, it was postulated that the increase in undrained shear strength for faster tests was due to negative excess pore water pressure during shear. This decrease in excess pore water pressure would increase the effective stress, consequently, increasing the clay shear strength. A summary of the triaxial tests perform on Cambridge, Boston, and Stockton clay including the type of test performed, the confining pressure or consolidation stress, and the slope of the shear strength at failure versus logarithm time to failure is provided in Table 2.1.

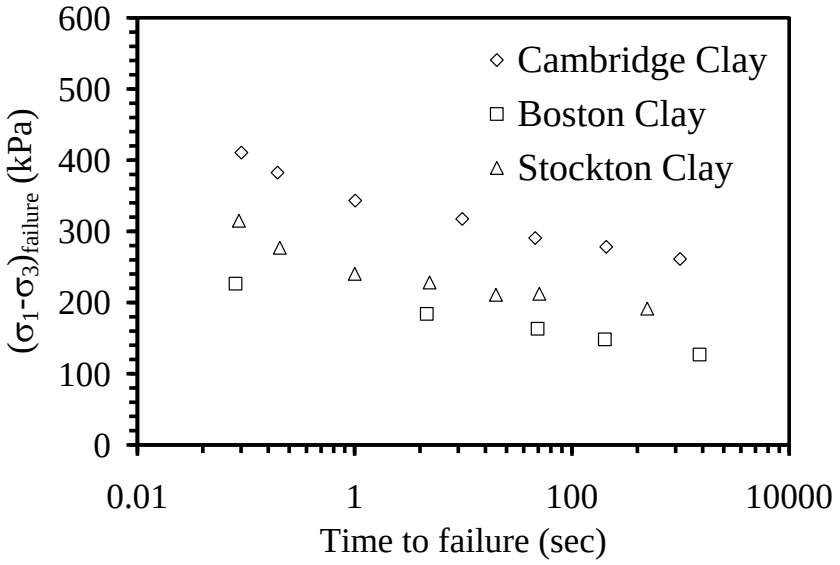

Figure 2.1: Variation in undrained shear strength of a soft clay with time to failure (after Casagrande and Shannon 1948).

Table 2.1: Summary of triaxial test performed on Cambridge, Boston and Stockton clay (Casagrande and Shannon 1948)

	Type of test	σ_3' (kPa)	Slope of $(\sigma_1 - \sigma_3)_f$ versus logarithm time to failure (kPa/sec)
Cambridge clay	CU	588	15.4
Boston clay	UU	300	13.0
Stockton clay	UU	300	10.0

Richardson and Whitman (1963) investigated the effects of axial strain rate upon undrained shear strength of remolded clay in CU triaxial tests. The testing material was alluvial clay with liquid limit of 62 and plasticity index of 38. Unlike Casagrande and Shannon (1948), changes in excess pore water pressure were measured during shear. Tests were run at two different times to 1% strain (t_1%): $t_{1\%}$ = 500 minutes and $t_{1\%}$ = 1 minute. The average principal stress difference and average excess pore water pressure versus axial strain reported by Richardson and Whitman (1963) is shown in Figure 2.2 for the two different strain rates. The excess pore water pressure corresponding to the shear strength at failure (maximum principal stress difference) for the 1 minute test is notably less than the pore pressure corresponding to the shear strength at failure for the 500 minute test. This study reinforces the notion that the observed increase in undrained shear strength with increasing strain rate is associated with a decrease in excess pore water pressure during shearing, which leads to an increased effective stress. A summary of the results from these tests is provided in Table 2.2.

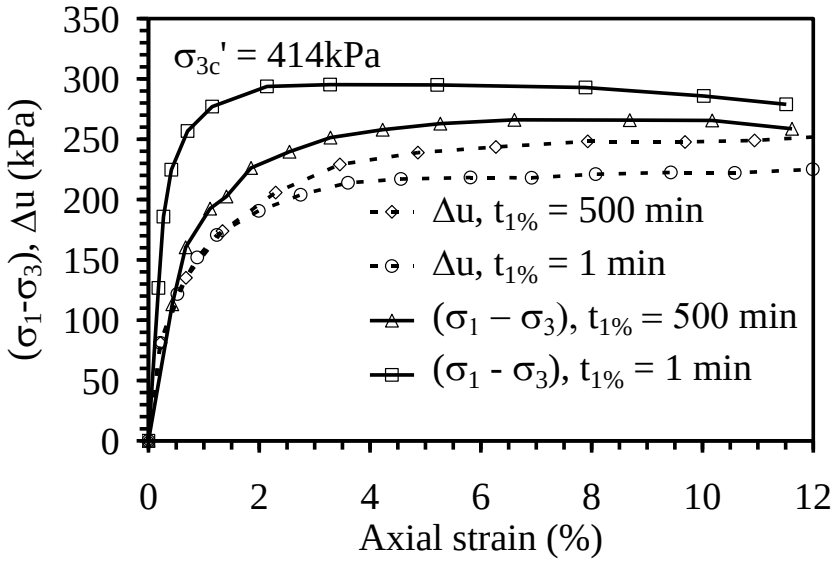

Figure 2.2: Results from Richardson and Whitman (1963) for average principal stress difference and excess pore water pressure versus axial strain for times to 1% strain of 1 minute and 500 minutes

Table 2.2: Results from CU triaxial tests performed by Richardson and Whitman (1963) on remolded alluvial clay

$t_{1\%}$ (min)	ε_{af} (%)	$(\sigma_1-\sigma_3)_f$ (kPa)	% increase in shear strength	Δu_f (kPa)	% decrease in excess pore water pressure
1	3.2	295	11.0	209	-14.4
500	6.6	266	-	244	-

Lefebvre and LeBoeuf (1987) investigated the strain rate effect on the undrained shear strength of intact field samples of three different over consolidated (OC) lacustrine or marine post-glacial clays under different consolidation stress states. The samples were tested in either an over consolidated "structured" state or in a normally consolidated (NC) state where each sample was consolidated beyond its in-situ preconsolidation pressure. For the structured samples, each sample was isotropically consolidated under a pressure equal to the in situ vertical effective stress, σ'_{v0}. For remolded specimens, the consolidation pressure ranged from 1.8 to 2 times the

preconsolidation stress of the remolded clay, σ_p'. After consolidation, the samples were sheared at strain rates ranging from 0.1 %/hour to nearly 6000 %/hour. The soil properties and consolidation details are provided in Table 2.3.

Table 2.3: Soil properties and consolidation details for CU triaxial tests performed by Lefebvre and Leboeuf (1987)

Name	LL, PL, PI	σ_p' (kPa)	$\sigma'_{c\_structured}$ (kPa)	σ'_{c_NC} (kPa)
Grande Baleine clay	30, 20, 10	112	45	224
Olga clay	68, 28, 40	78	18	137

Note: The effective consolidation stress for structured clays, $\sigma'_{c\_structured}$, is equal to the in situ vertical effective stress, σ'_{v0}

For all of their tests, Lefebvre and LeBoeuf (1987) observed that the undrained shear strength increased with decreasing strain rate. However, the excess pore water pressure response between the structured clay and NC clay was drastically different. For the structured clays, there appeared to be no rate effects on the pore pressure response. In fact, the pore pressure at failure was nearly identical regardless of the strain rate applied for both Olga and Grande Baleine clay. However, when the clays were consolidated to pressures past the in situ vertical effective stress, there was a distinct decrease in pore pressure at failure that accompanied an increase in shear strength with increased strain rate. These trends are illustrated in Figure 2.3 for Olga clay and Figure 2.4 for Grande Baleine clay. The authors hypothesized that the increase in undrained shear strength for the structured clays was due to a decrease in the friction angle which lowered the failure envelope as strain rate decreased rather than a decrease in pore pressure. The NC clay behavior showed a decrease in excess pore water pressure with increasing strain rate, thus increasing the effective stress and increasing the undrained shear strength.

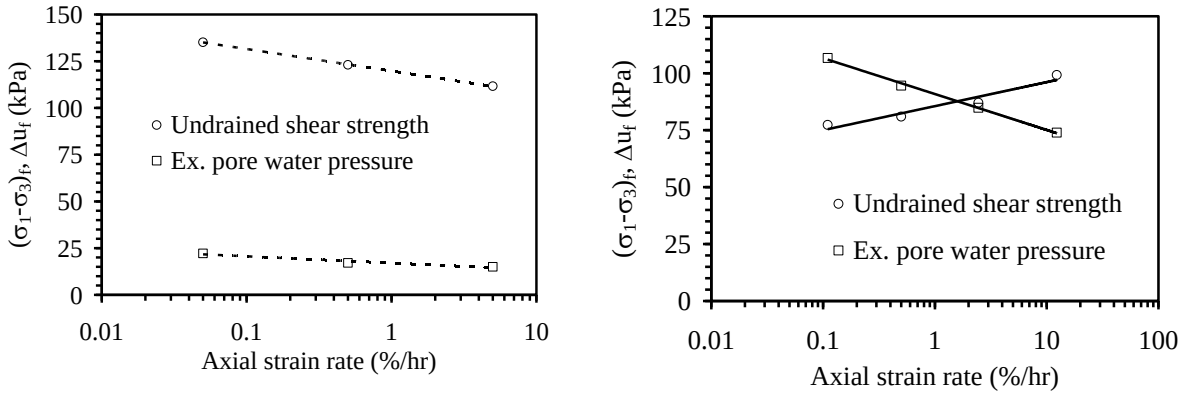

(a) (b)

Figure 2.3: Undrained shear strength $(\sigma_1-\sigma_3)_f$ and excess pore water pressure Δu_f at failure versus axial strain rate (after Lefebvre and LeBoeuf 1987): (a) Structured Olga Clay; and (b) NC Olga clay

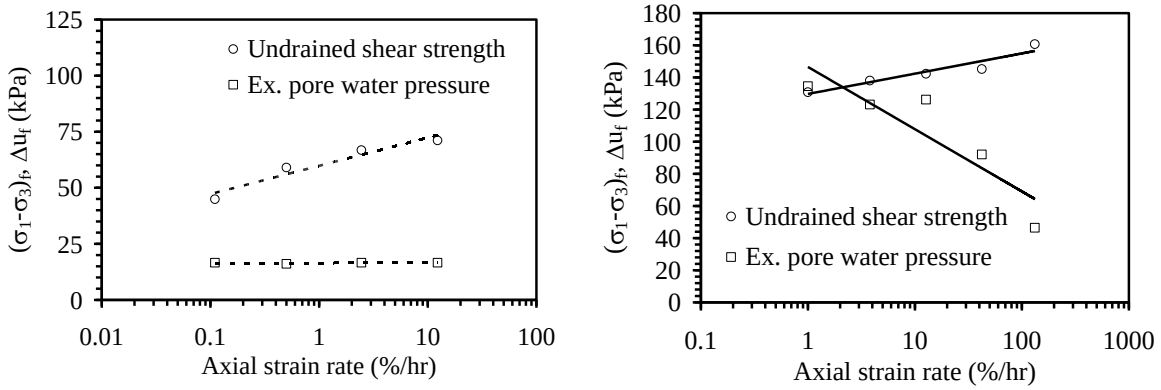

(a) (b)

Figure 2.4: Undrained hear strength $(\sigma_1-\sigma_3)_f$ and excess pore water pressure Δu_f at failure versus axial strain rate (after Lefebvre and LeBoeuf 1987): (a) Structured Grande Baleine clay; and (b) NC Grande Baleine clay

Zhu and Yin (2000) investigated the behavior of Hong Kong marine clay in various Over consolidated conditions focusing on the strain rate effect on undrained shear strength and excess pore water pressure as the over consolidation ratio (OCR) changed. The geotechnical properties reported by Zhu and Yin (2000) for this soil are provided in Table 2.4. The soil was mixed with water, consolidated to a pressure of about 55 kPa, and trimmed to triaxial specimens 100 mm to 50 mm length to diameter. A series of consolidated undrained tests were performed on specimens with OCR values of 1, 2, 4, and 8. To achieve the desired OCR each specimen was

consolidated to a certain pressure and unloaded by a pressure increment which would give the desired OCR. The effective consolidation pressures, σ_c', and pressure after unloading but before shear, σ_0', as reported by Zhu and Yin (2000) are given in Table 2.5.

Table 2.4: Geotechnical properties of Hong Kong marine clay (after Zhu and Yin 2000)

Propety	Value	Units
Description	Soft illitic sity clay	
% clay	27.5	%
% silt	46.5	%
% fine sand	26	%
LL, PL, PI	60, 28, 32	-
ϕ'	31.5	degrees
k	6.15E-10	m/s

Table 2.5: Effective preconsolidation pressure, effective consolidation pressure after unloading for various OCRs (after Zhu and Yin 2000)

OCR	σ_c' (kPa)	σ_0' (kPa)
1	400	400
2	200	100
4	400	100
8	800	100

For each OCR, three strain rates were applied to different specimens: 0.15, 1.5, and 15 %/hour. Since tests conducted with an OCR of 1 were sheared under a higher initial effective stress, σ'_{v0}, than tests with an OCR of 2, 4 or 8, the maximum undrained shear strength and excess pore water pressure was normalized by the initial vertical effective stress. Results for the undrained shear strength and corresponding excess pore water pressure versus strain rate in log scale from Zhu and Yin (2000) are shown in Figure 2.5(a) and Figure 2.5(b). Zhu and Yin (2000) observed an increase in the normalized undrained shear strength with increasing OCR for each individual strain rate as well as an increase in shear strength with increasing strain rate for each individual OCR, as shown in Figure 2.5(a). It was also observed that the rate at which the undrained shear strength increased per log cycle increase in strain rate increased with larger

OCR. The numerical values and slopes of the normalized undrained shear strength with logarithm of strain rate are reported in Table 2.6.

From the excess pore water pressure measurements, Zhu and Yin (2000) reported decreases in normalized excess pore water pressure at the point of maximum normalized shear strength with increased strain rate as well as increased OCR. As with the shear strength, the rate at which the normalized excess pore water pressure at failure decreased with increased strain rate was greater at larger OCRs. The numerical values and slopes of the normalized excess pore water pressure with logarithm of axial strain rate are reported in Table 2.7.

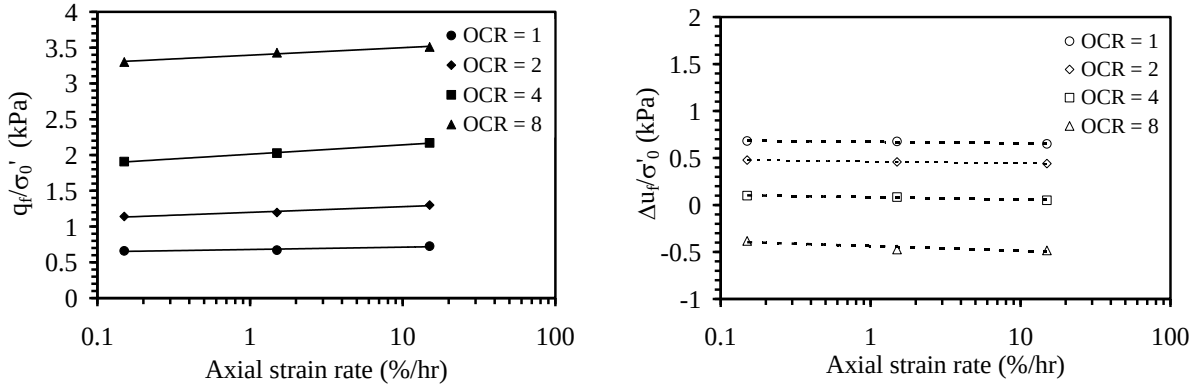

(a) (b)

Figure 2.5: Results from consolidated undrained tests on marine clay with different axial strain rates (after Zhu and Yin 2000): (a) Normalized undrained shear strength; (b) Normalized excess pore water pressure

Table 2.6: Normalized maximum undrained shear strength and slope of the normalized undrained shear strength with logarithm of strain rate at various OCRs for Hong Kong Marine clay (after Zhu and Yin 2000)

Strain rate (%/hr)	0.15	1.5	15	
OCR	q_f/σ_0' (kPa)	q_f/σ_0' (kPa)	q_f/σ_0' (kPa)	Slope of q_u/σ'_0 vs. logarithm of strain rate
1	0.66	0.67	0.73	0.014
2	1.14	1.20	1.30	0.034
4	1.91	2.03	2.17	0.056
8	3.30	3.43	3.51	0.045

Table 2.7: Normalized excess pore water pressure at the point of maximum undrained shear strength and slope of the normalized excess pore water pressure with logarithm of strain rate at various OCRs for Hong Kong Marine clay (after Zhu and Yin 2000)

Strain rate (%/hr)	0.15	1.5	15	
OCR	$\Delta u_f/\sigma'_0$ (kPa)	$\Delta u_f/\sigma'_0$ (kPa)	$\Delta u_f/\sigma'_0$ (kPa)	Slope of $\Delta u_f/\sigma'_0$ vs. logarithm of strain rate
1	0.68	0.68	0.65	-0.007
2	0.48	0.46	0.44	-0.008
4	0.10	0.08	0.05	-0.011
8	-0.38	-0.47	-0.48	-0.022

Olson and Parola (1967) were the only researchers to investigate the strain rate effect on partially-saturated cohesive soils. They performed a number of UU triaxial tests on compacted Goose Lake clay at different water contents and different axial strain rates. A confining pressure of either 690 or 6900 kPa was applied before shear. The geotechnical properties for the clay used by Olson and Parola (1967) are listed in Table 2.8 and the testing details are provided in Table 2.9.

Table 2.8: Geotechnical properties of Goose Lake clay (after Olson and Parola 1967)

Propety	Value	Units
LL, PL, PI	31, 17, 14	-
% clay	9	%
% silt	57	%
% sand	34	%
$\gamma_{d\_optimal}$	13.5	kN/m^3
$w_{optimal}$	14.5	%
c'	10.3	kPa
ϕ'	25.5	degrees

Table 2.9: Specimen details of initial water content, dry unit weight, degree of saturation, void ratio and confining pressure (after Olson and Parola 1967)

w (%)	γ_d (kPa)	S (%)	e	σ_{3c} (kPa)
6.5	12.6	28	1.11	690 or 6900
10.5	12.8	48	1.08	690 or 6900
13.5	13.5	72	0.98	690 or 6900
16	13.7	90	0.95	690
18	13.2	91	1.03	690

The results from Olson and Parola (1967) for the principal stress difference at failure versus time to failure for five difference compaction water contents are shown in Figure 2.6. The time to failure used to by Olson and Parola to shear their specimens refers to the actual testing time it takes to shear a specimen to a specific axial strain. It does not refer to the time required to reach actual failure (maximum deviator stress or the time for the stress path to touch the failure envelope). The increase in undrained shear strength per log cycle of time to failure ranges from 3 to 11%. For the same time to failure, the test that was run with the lowest water content had the greatest shear strength (maximum principal stress difference) at failure. As the compaction water content increased, the shear strength of the clay decreased. These results are not surprising since the matric suction of a soil increases as the degree of saturation and corresponding water content decreases. The general equation for effective stress in unsaturated soils can be written as follows (Bishop 1959):

$$\sigma' = (\sigma - u_a) + \chi(u_a - u_w) \qquad 2.1$$

where $(\sigma - u_a)$ is the net stress, χ is an parameter related to the degree of saturation, and $(u_a - u_w)$ is the matric suction. Using Equation 2.1, it would seem reasonable to believe that with increased matric suction (lower degree of saturation and hence lower water content) there is an increase in the effective stress and hence an increase in shear strength.

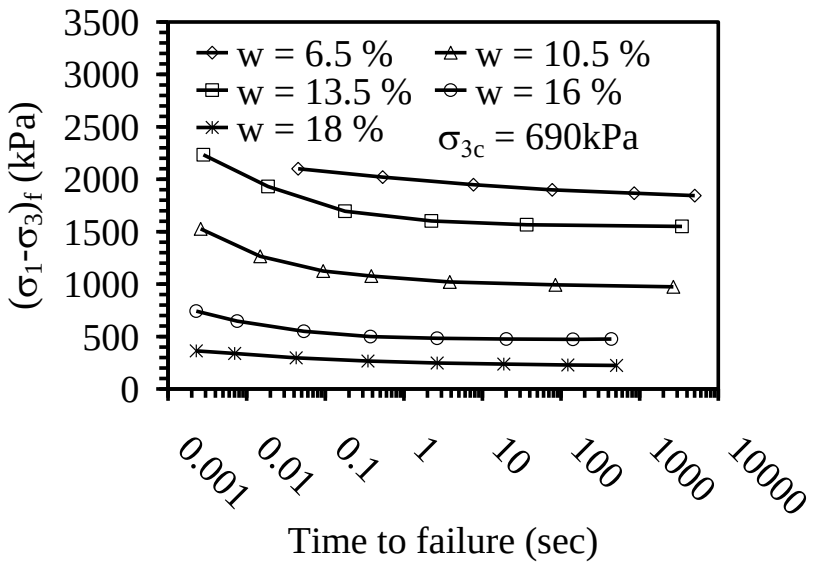

Figure 2.6: Principal stress difference versus time to failure for different compaction water contents (w) (after Olson and Parola 1967)

Although the failure mechanisms under very slow loading rates (creep tests) compared to rapid loading rates could be fundamentally different, understanding the issues involved with triaxial creep tests could help to interpret results of triaxial tests at higher strain rates. Casagrande and Wilson (1951) performed undrained creep tests on a number of different saturated clays and a few unsaturated clays. For the study they found that for tests on saturated clays, the strength decreased as the time of loading increased while for the unsaturated clays, there was an initial decrease in strength to a time of loading of 100 minutes at which point then the trend reversed and the strength increased as the time of loading increased. Casagrande and Wilson (1951) attributed this increase in strength of the unsaturated soil to a decrease in void ratio as the air voids collapsed and densified the soil. However, this increase in strength could also be due to migration of pore water pressure throughout the specimen particularly away from the shear zone or changes in the chemical make-up of the clays during very slow loading.

2.2.2 Conclusions from Previous Studies on Cohesive Soils

It has been well established through the studies of Casagrande and Shannon (1948), Richardson and Whitman (1963), Olson and Parola (1967), Lefebvre and LeBoeuf (1987) and Zhu and Yin (2000) that the undrained shear strength of cohesive soil is dependent upon strain rate applied. Specifically, the undrained shear strength of a NC or OC cohesive soil at failure increases with increasing strain rate. This strength increase is usually accompanied by a decrease in excess pore water pressure which increases the effective stress at failure. For NC soils, as the soil is sheared the excess pore water pressure remains positive regardless of the strain rate. However, the magnitude of the excess pore water pressure generated is less at faster rates than at slower rates. For OC soils, during shear the soil tends to dilate causing the generation of negative excess pore pressures. If the strain rate is increased, these excess pore pressures become more and more negative. The specific aspects and focal points of each of the before mentioned research endeavors investigating the effect of higher strain rate on cohesive soils are summarized in Tables 2.10 and 2.11.

Table 2.10: Summary of geotechnical properties from previous studies on cohesive soils

Author	Year	Soil Name - Description	Test type	Saturated or Unsaturated	Stress State	% increase in shear strength per 10 fold increase in strain rate
Casagrande and Shannon	1948	Cambridge clay - med. soft	UC, UU, CU	NR	NR	15
Casagrande and Shannon	1948	Boston clay - med. soft	UC, UU, CU	NR	NR	13
Casagrande and Shannon	1948	Stockton clay - stiff and compacted	UC, UU, CU	NR	NR	8
Richardson and Whitman	1963	Alluvially deposited clay	CU	Saturated	Remolded NC	11
Olson and Parola	1967	Goose lake clay - manufactured clay	UU	Unsaturated	Compacted	3 - 8
Lefebvre and LeBoeuf	1987	Grande Baleine clay - soft post glacial clay	CU	Saturated	ntact OC and NC	5 - 8
Lefebvre and LeBoeuf	1987	Olga clay - soft post glacial clay	CU	Saturated	ntact OC and NC	8 - 17
Zhu and Yin	2000	Hong Kong Marine clay - Soft marine clay	CU	Saturated	Remolded OC	2 - 8

UC = Unconfined compression UU = Unconsolidated undrained
CU = Consolidated undrained OC = Over consolidated
NC = Normally consolidated NR = Not reported

Table 2.11: Summary of testing details from different studies on clay

Author	Year	Soil Name - Description	LL, PL, PI	e_i	σ'_3 (kPa)
Casagrande and Shannon	1948	Cambridge clay - med. soft	44-59, 21-27, 23-32	NR	588
Casagrande and Shannon	1948	Boston clay - med. soft	42, 20, 22	NR	300
Casagrande and Shannon	1948	Stockton clay - stiff and compacted	62, 22, 40	NR	300
Richardson and Whitman	1963	Alluvially deposited clay	62, 24, 38	NR	414
Olson and Parola	1967	Goose lake clay - manufactured clay	31, 17, 14	1.11-0.95	680 or 6800
Lefebvre and LeBoeuf	1987	Grande Baleine clay - soft post glacial clay	60, 28, 32	NR	224
Lefebvre and LeBoeuf	1987	Olga clay - soft post glacial clay	68, 28, 40	NR	137
Zhu and Yin	2000	Hong Kong Marine clay - Soft marine clay	60, 28, 32	NR	400 or 100

NR = Not reported e_i = Initial void ratio before consolidation

There are three primary mechanisms that influence the shear strength of soil: frictional resistance to movement due to normal forces acting across a particle to particle bond, stress independent cohesion, and effort required to permit dilation (Mitchell 1964). For over-consolidated clay there is a greater tendency to dilate during shear. Thus, larger negative excess pore water pressures are generated. As the strain rate is increased the soil initially becomes stiffer (Casagrande and Shannon 1948; Zhu and Yin 2000; Richardson and Whitman 1963; Olson and Parola 1967) and the tendency for resistance to dilate would also increase. From this assumption it would seem logical to believe that the strain rate effect would be most prominent in OC clays with the greatest tendency for dilation. Zhu and Yin (2000) observed this behavior when the rate of shear strength increased with increased strain rate at greater over consolidation ratios (OCRs).

Lefebvre and LeBoeuf (1987) also investigated the strain rate effect on shear strength between over consolidated (OC) and normally consolidated (NC) specimens. It was believed that the rate effects of the OC structured clay stemmed from lowering of the peak strength envelope rather than generation of lower excess pore water pressure. The lowered failure envelope could be due to the structured nature of the clay which allows for greater inter-particle friction to be generated at higher strain rates. This behavior is different than that of the normally consolidated remolded clay were the result of lower excess pore water pressure at higher rates. This study

highlights the importance of understanding the stress history and inter-particle bonding that may arise for different soil skeleton structures.

Olson and Parola (1967) demonstrated that the shear strength of compacted clay increases with decreased water content as well as increased strain rate. However, no direct correlation between matric suction and shear strength increase was made. Furthermore, since the tests performed were UU triaxial tests, excess pore water pressures generated during shear were not measured.

Although these tests have significantly helped to understand the behavior of clays during shear at elevated strain rates, there still remain a number of unanswered questions not addressed in the currently available literature. Namely, the effect of strain rate on the undrained shear strength of saturated, compacted clays and the effect of strain rate on the undrained shear strength and excess pore water pressure of unsaturated soils at known suction values.

2.3 Strain Rate Effects on Cohesionless Soil

2.3.1 Review of Previous Studies on Cohesive Soils

Due to differences in the structure, particle size, rate of drainage, and pore water interaction behavior of cohesive and cohesionless soils, it is logical to hypothesize that there are differences in the effects of strain rate on the shear strength of these two different types of soil. Thus, it cannot be assumed that observations and conclusion from studies on the rate effects of cohesive soils are valid for cohesionless soils.

Casagrande and Shannon (1948) performed tests on a clean medium sand. The sand was compacted to a relative density of 0.92 with an initial void ratio of 0.62 and tested dry in a vacuum-type triaxial cell. The applied vacuum confining pressure was 30 kPa. From this

investigation, it was found that the strength of the sand increased slightly with increases in strain rate. The maximum strength increase per log cycle reported was 10%.

Lee et al (1969) investigated the effect of confining pressure on the time dependent behavior of dry and saturated sand in both loose and dense configurations. The sand used for dry tests was clean, uniformly graded, fine sand dredged from the Sacramento River near Antioch, CA and is referred to as Antioch sand. The minimum and maximum void ratios were 0.75 and 1.14 respectively. The sand was tested in consolidated drained triaxial compression in either a dense state with a corresponding relative density of 100% or a loose state with a corresponding relative density of 38%. For each relative density, three different consolidation stresses of 102, 589, or 1,472 kPa were applied to the specimens. A number of tests were then performed at different strain rates ranging from 0.02 to 40,000 %/min for each combination of consolidation stress and relative density.

To compare the different test, the shear strength at failure defined at the maximum principal stress difference was normalized by the shear strength at failure at an axial strain rate of 0.1 %/min. The results for tests performed at both relative densities and all confining pressures are shown in Figure 2.7. For the sand tested at a relative density of 100%, a 6% increase in shear strength per log cycle increase in axial strain rate was observed for tests subject to the largest confining stress (1,472 kPa) over strain rates varying from 0.02 %/minute to 15,000 %/minute. However, the observed strength increase was only 2 - 3% per log cycle increase in strain rate over the same range of strain rates for lower confining pressures (102 and 589 kPa). The soil tested in a loose state of 38% relative density showed the same increase in strength with strain rate of 7% regardless of the confining pressure.

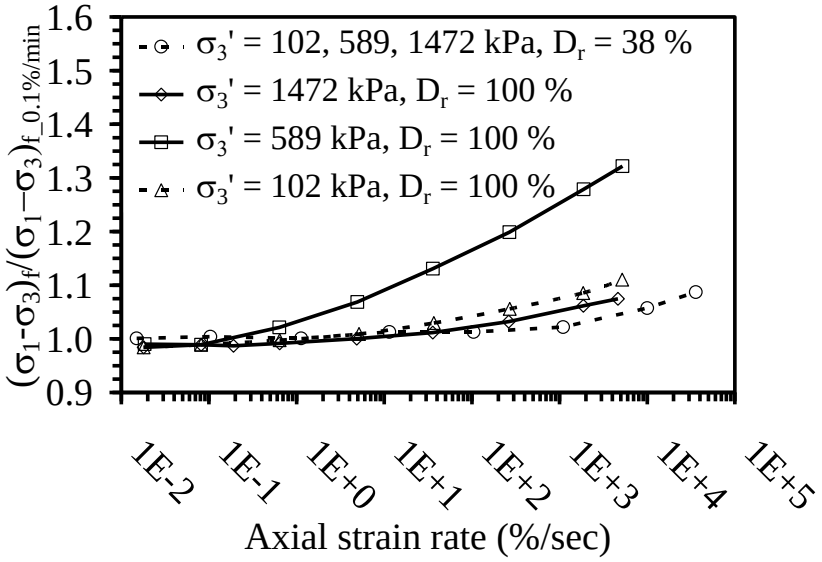

Figure 2.7: Maximum principal stress difference with axial strain rate for dry Antioch sand at different confining pressures and relative densities (after Lee et al. 1969)

The sand used in saturated testing was also dredged from the Sacramento River but at a different location. The grain size distribution and other soil properties were very similar to Antioch sand. The Sacramento River sand was tested in consolidated undrained triaxial compression under constant load conditions. The initial relative density was 78%, and the corresponding void ratio was 0.71. All tests were subject to a consolidation pressure 2943 kPa. After consolidation, the drainage lines to the specimen were closed, an additional load was applied, and the time to failure (maximum deviator stress) was recorded. As the additional applied load increased, the time to failure decreased. The results from these tests showed that the shear strength of saturated Sacramento River sand had a 20 % increase per ten-fold increase in strain rate. The excess pore water pressure response after the drainage lines were closed is shown in Figure 2.8 for two cases: no extra applied load and an extra applied load of 834 kPa. From

Figure 2.8, it is clear that the tests with a sudden increase in applied load and a lower time to failure has a decrease in pore water pressure.

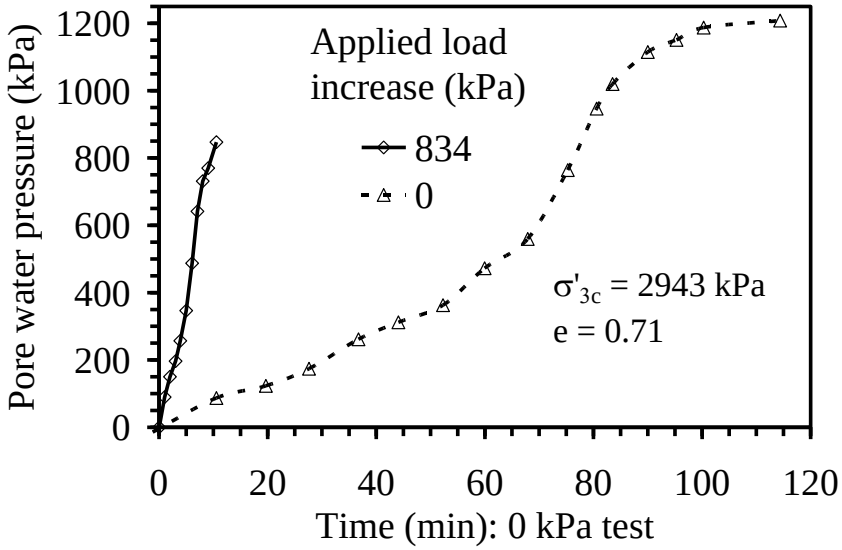

Figure 2.8: Pore water pressure after closure of drainage valve and application of additional load (after Lee et al. 1969)

Lee et al. (1969) believed that the particle crushing characteristics of sand would become a larger contributing factor to the shear strength as the confining pressure increased. The results from both dry and saturated triaxial testing suggested a greater increase in shear strength at higher strain rates for tests conducted at higher confining pressures. As the confining pressure increases, the soil structure is forced to compress into a tighter configuration. Dilatational movement is restricted and the inter-particle stresses increase. When the soil is sheared, in addition to dilating, the particles themselves crush to dissipate the energy. At higher confining pressure there will be two mechanisms working to take the applied stresses and the strain rate effect on the shear strength will be greater.

In a report to the U.S. Army Engineer Waterways Station, Whitman (1970) looked at the effect of strain rate on loose, dry Ottawa sand. Geotechnical properties including minimum and

maximum void ratio and relative density were not given in the report. The dry sand was tested at an initial void ratio of 0.52 with confining stresses of 88 kPa and 34 kPa. Axial strain rates applied ranged from 0.04 %/sec to 170 %/sec. From these tests, Whitman (1970) reported a slight initial decrease in both the shear strength and friction angle from the slowest strain rate to approximately a strain rate of 4 %/sec. At this point, the shear strength and friction angle started to increase with increase strain rate. It was hypothesized that this behavior could be due to a lower coefficient of kinetic friction to static friction at slower strain rates.

Whitman (1970) also performed saturated tests on Ottawa sand. The initial void ratio and confining cell pressure was 0.65 and 350 kPa respectively. The sand was tested at strain rates of 0.001 %/sec or 50 %/sec. The results of deviator stress and excess pore water pressure from these tests is shown in Figure 2.9. The deviator stress at both strain rates continues to increase with axial strain. The 50 %/sec strain rate reaches a larger principal stress difference and lower excess pore water pressure at higher axial strains than the 0.001 %/sec rate. Whitman explained that this behavior was due to a greater tendency for the sand to dilate with axial straining. In undrained conditions, in order to account for this tendency to dilate as well as maintaining constant volume there must be an increase in the effective stress.

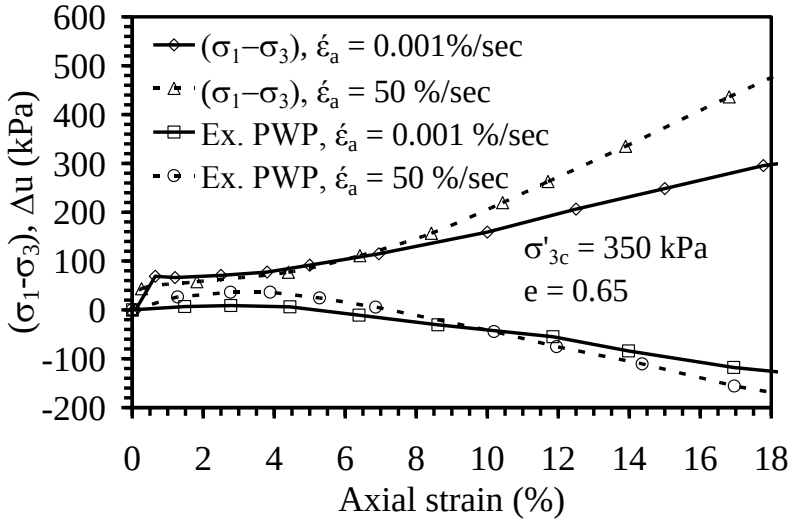

Figure 2.9: Deviator stress and excess pore water pressure of loose, saturated Ottawa sand at strain rates of 0.001 %/sec and 50 %/sec (after Whitman 1970)

Yamamuro et al. (2011) studied the effects of loading rate on loose and medium dense, dry, coral sand. The minimum and maximum void ratios for the coral sand were 0.74 and 1.20. Specimens were created with initial void ratios of either 1.03 or 0.93 corresponding to relative densities of 38 and 58% respectively. All specimens were tested dry in drained conditions under consolidation pressures of either 98 kPa or 350 kPa. Each test was photographed with a high speed camera. The images taken during testing were used along with collected load data to determine the shear strength and volumetric strain of each test. The variation of principal stress difference and volumetric strain with axial strain are shown in Figure 2.10 for tests with a relative density of 38% and Figure 2.11 for tests with a relative density of 58%.

Their findings showed an increase in the principal stress difference with strain rate for both loose and medium dense sands. The loose sand showed an 8% increase in undrained shear strength per log cycle increase in strain rate while the medium dense sand showed a 10 % increase per log cycle increase in strain rate. The dilatancy rate at failure, defined at the point of

maximum principal stress difference, increases with increased strain rate for medium dense specimens and decreases with increased strain rate for loose specimens. The axial strain at failure was reported to decrease with increased strain rate. At very high strain rates with low confining pressure, it was observed that the peak stress value did not correspond to the maximum dilatancy rate, which is inconsistent with traditional behavior. The shear strength parameters values at failure for tests on sand with relative density of 38% are shown in Table 2.12 and for tests on sand with a relative density of 58% are shown in Table 2.13.

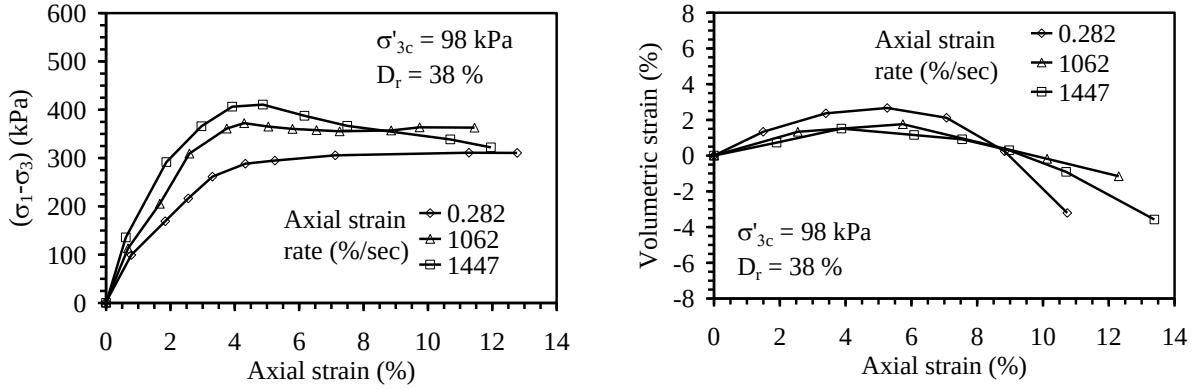

(a) (b)

Figure 2.10: The variation of the principal stress difference with axial strain (a) and volumetric strain with axial strain (b) at various axial strain rates for tests with a relative density of 3 % (after Yamamuro et al. 2011)

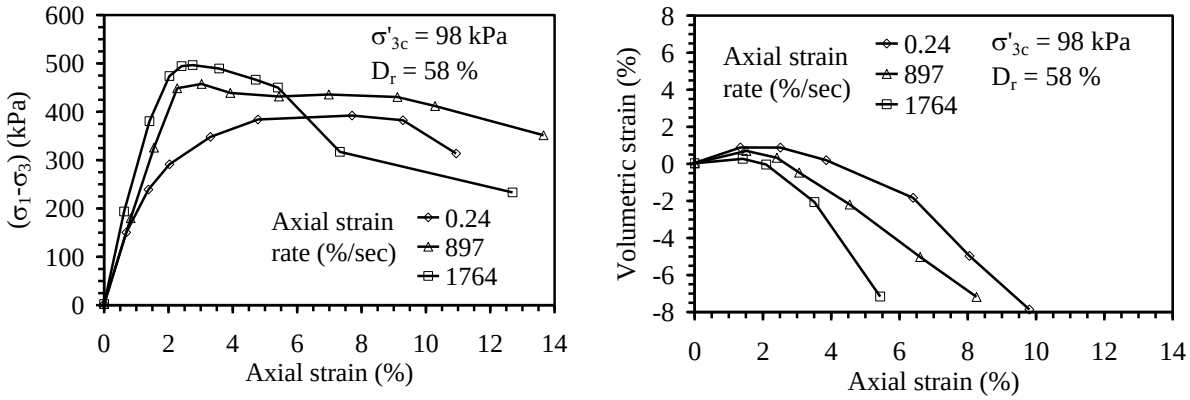

(a) (b)

Figure 2.11: The variation of the principal stress difference with axial strain (a) and volumetric strain with axial strain (b) at various axial strain rates for tests with a relative density of 58% (after Yamamuro et al. 2011)

Table 2.12: Parameters at failure for crushed coral sand specimens with a relative density of 38% (after Yamamuro et al. 2011)

Axial strain rate (%/sec)	$\varepsilon_{a\_failure}$ (%)	$(\sigma_1 - \sigma_3)_{max}$ (kPa)	% increase in shear strength	ε_{vf} (%)	Vol. strain rate at failure
0.282	11.3	311	-	-3.2	-1.82
1062	4.3	372	19.7	1.5	0.13
1447	4.9	411	10.3	1.3	-0.16

Table 2.13: Parameters at failure for crushed coral sand specimens with a relative density of 58% (after Yamamuro et al. 2011)

Axial strain rate (%/sec)	$\varepsilon_{a\_failure}$ (%)	$(\sigma_1 - \sigma_3)_{max}$ (kPa)	% increase in shear strength	ε_v (%)	Vol. strain rate at failure
0.24	7.7	392	-	-3.4	-1.2
897	3.0	458	16.7	-0.5	-1.2
1764	2.8	496	8.5	-1.1	-1.4

2.3.2 Conclusions and Discussion from Previous Studies on Cohesionless Soils

Studies performed by Casagrande and Shannon (1948), Whitman (1957), Lee et al. (1967), and Yamamuro et al. (2011) observed that the undrained shear strength would increase between 0-15% for dry sands at 10-20% for saturated sands depending on the confining pressure. A summary table detailing the geotechnical properties and confining pressures is provided in Table 2.14. A summary of testing details is provided in Table 2.15.

Table 2.14: Geotechnical properties and confining pressure from previous studies on cohesionless soils

Author	Year	Soil name - Description	e_{min}, e_{max}	I_D (%)	$e_{initial}$	σ'_3 (kPa)
Casagrande and Shannon	1948	Manchester sand - clean med. sand	0.60, 0.88	0.92	0.62	30
Lee, Seed and Dunlop	1969	Antioch sand - clean, uniform, fine sand	0.75, 1.14	100 or 38	0.75 or 1.0	100, 589, or 1500
Lee, Seed and Dunlop	1969	Sacramento sand - clean, uniform fine sand	0.75, 1.14	0.78	0.71	3000
Yamamuro, Abrantes and Lade	2011	crushed coral	0.74, 1.20	38 or 58	1.03 or 0.98	98 or 350
Whitman	1970	Ottawa sand - uniform sand	Not given	Not given	0.65	350

Table 2.15: Testing details from previous tests on cohesionless soils

Author		Soil name - Description	Test type	Saturation Condition	% increase in shear strength per 10 fold increase in strain rate
Casagrande and Shannon	1948	Manchester sand - clean med. sand	CD	dry	10
Lee, Seed and Dunlop	1969	Antioch sand - clean, uniform, fine sand	CD	dry	2 - 6
Lee, Seed and Dunlop	1969	clean, uniform fine sand	CU	saturated	10
Yamamuro, Abrantes and Lade	2011	crushed coral	CD	dry	8 -10
Whitman	1970	Ottawa sand	CU	Saturated	20
Whitman	1970	Ottawa sand	CD	Dry	Negligible

CD = Consolidated drained CU = Consolidated undrained

As with cohesive soils, the strength of sand during shear could be broken into three main components: sliding friction, dilatancy, and particle crushing (Lee et al. 1967, Omidvar et al. 2012). Depending on the stress state or soil condition, (i.e. high confining pressure versus low confining pressure or dense versus loose particle packing), the individual contribution of each of the three shear strength factors to the overall undrained shear strength either increases or decreases. The difficulty in understanding the rate effect mechanisms for the strength increases in sand comes from determining which component is being altered at elevated rates and how.

Direct shear tests on dry Ottawa sand have indicated that inter-particle friction is relatively independent of shearing rate ranging from 18 mm/s to 152 mm/s (Horne and Deere 1962). It has been observed that test results at higher strain rates show the friction angle of both dense and loose sand first decreases slightly, possibly due to the lower coefficient of kinetic friction to static friction, and then increases up to two degrees as the tendency to dilate increases at higher strain rates (Whitman 1970; Huy 2006; Omidvar et al. 2012). These findings are indications that

larger friction angles observed at higher rates may occur due to dilatational volume change rather than an actual mechanical/frictional change between particles. Thus, the coefficient of sliding friction can be assumed to be independent on strain rate for all intents and purposes (Bowen and Tabor 1956; Horne and Deere 1962).

Given the above argument, the rate effect on sand must be due to either dilatancy, grain crushing, or a combination of the two. At low confining pressures, the sand particles are much freer move, climb and roll on top of each other causing dilation as the sand is sheared. Furthermore, the stresses between the individual particles are not high enough to cause fracture of the individual grains and the particles will tend to rearrange rather than crush. Therefore, it is generally believed that at low confining pressures the controlling mechanism for rate effects on sand is dilation (Lee et al. 1969; Omidvar et al. 2012).

Previous research has shown that strain rate effect on the shear strength of sands can vary from no effect to a 20 % increase in strength. Assuming that inter-particle friction is independent of strain rate, the magnitude of the strength increase is a function of dilatancy and grain crushing during shear. If the potential for a sand to dilate is high (dense sands at low confining pressures), generation of negative pore pressures in a saturated state would be a major contributing factor to strength increase. For sand in a loose configuration at low confining pressures, the potential for dilatancy will still contribute to the shear strength but to a lower degree. At higher confining pressures, the dilatancy effect will decrease and the effect of grain crushing will become a larger contributor to shear strength.

2.4 Mechanisms of Strain Rate Effects

Along with research dedicated to testing investigating the effect of strain rate on particular soils, work has also be done to generalize these finding and implement them into design. At the particle level, there are three specific sources which contribute to shear strength: frictional

resistance to movement due to normal forces acting across a particle to particle bond, stress independent cohesion, and effort required to permit dilation. Specifically, at a given void ratio, the shear strength is a function of friction angle, void ratio, temperature, strain rate, effective stress and soil structure (Mitchell 1964). Mineralogy can also be a contributing factor to shear strength for both cohesive and cohesionless soils. For instance, Olson (1974) performed a number of triaxial tests on pure clay minerals. It was found that the failure envelopes tended to segregate based upon the mineral being tested. Kaolinite had a range of ϕ angles with the greatest magnitude while smectite had a range with the smallest ϕ angle. The range of Illite ϕ angles fell in between Kaolinite and Smectite. As mentioned in the previous section Horne and Deere (1964) found that the shear resistance of mica decreased upon wetting. Mitchell (1976) noted that even a small percentage of mica present in a sand or silt could experience high compressibility or swelling upon unloading.

From the above discussion, it is clear that shear mechanisms within a soil are very complex. For design purposes, all these factors must be simplified into a useable model or equation. For instance, Mohr-Coulomb theory only takes into account cohesion, effective stress, and friction angle. The problem is amplified when soil is sheared at higher rates and the mechanisms change. The next few paragraphs presents ideas from previous research on how these mechanisms change with changes in strain rate.

As a rule of thumb, the shear strength of cohesive soils increases on average 10% per log cycle increase in strain rate. Furthermore, it is accepted that the elastic limit is also related to strain rate with the following relationship (Leroueil and Marques 1996).

$$\sigma_y = A + \alpha \log(\dot{\varepsilon}) \qquad 2.2$$

where σ_y is the elastic yield stress, $\dot{\varepsilon}$ is the applied strain rate, and A and α are material parameters dependent upon the pore fluid and suction (Pereira and Gennaro 2010).

Pereira and Gennaro (2010) altered the Barcelona Basic Model (BBM) for unsaturated soils to incorporate the effect of strain rate. They explained that at slow rates (10^{-4} to 10^{-8} %/sec), the preconsolidation pressure of a cohesive soil not only increases with suction as introduced through the BBM but also with increasing strain rate. The increase in preconsolidation pressure results in an increase in the yield stress with increasing strain rate under isotropic conditions.

Mitchell (1964) developed a conceptual, rate dependent shear strength model based upon a particulate mechanics approach. Mitchell (1964) altered the traditional Mohr-Coulomb theory to incorporate the effects of strain rate, soil structure, and temperature on shear strength. Starting from the energy required for relative motion between two particles, and expanding this concept to a particle system, Mitchell (1964) argued that straining between two particles is based purely on cohesive (temperature and physico-chemical nature of the soil) and structural components of the soil. In other words, the strength component due to applied strain rate is independent on applied or effective stresses (Mitchell 1964). It should be noted that Mitchell (1964) did not specify a range of strain rates in which he believed his model was valid.

In contrast, Whitman (1970) hypothesized that larger capillary tensions within the soil structure could be sustained during a rapid loading to higher strains than during slow loading. As a result, the effect of strain rate on shear strength will be greatest when negative excess pore water pressures (higher effective stresses) contribute most to shear strength. This hypothesis was based upon experimental results which showed decreases in excess pore water pressure with increased strain rate.

Although it has been well established that the shear strength of both cohesive and cohesionless soils show some rate dependency, there are still a number of gaps in the literature that need to be addressed. Namely, rate effects on excess pore water pressure and shear strength of compacted and unsaturated clay, as well as rate effect on the generation of pore water pressure in saturated dense sand. An even bigger challenge is to understand the mechanisms from which rate dependency stems and possibly how to implement the effects into design.

3.0 Testing Materials

3.1 Overview

Two natural soils, a sand and clay obtained from the region around Boulder, Colorado were chosen as test materials. The clay was obtained from a stockpile of soil from a construction site on the University of Colorado Boulder campus, and is referred to as Boulder clay. The clay was processed after collection to remove all particles greater than the #10 sieve, which provided a more homogeneous and consistent material for experimental testing. The sand was purchased from a local quarry in Longmont, Colorado (Colorado Materials), and is referred to as Mason sand. This section presents the measured geotechnical properties of these two materials, including the grain size distribution, void ratio limits (e_{min} and e_{max}), specific gravity, and shear strength for the Mason sand, and Atterberg limits, grain size distribution, specific gravity, standard Proctor compaction curve, oedometer, swell potential, and soil water retention curve for Boulder clay.

3.2 Mason Sand

3.2.1 Grain Size Analysis

A sieve analysis was performed in accordance with ASTM D422-63 to measure the grain size distribution of the Mason sand. The sieve numbers used in this analysis ranged from #20 (US) to #200 (US). The grain size distribution curve is shown in Figure 3.1 and the values of D_{10}, D_{30}, D_{60}, C_u, and C_z values are shown in Table 3.1. Based on the grain size distribution, the Mason sand is classified as poorly graded sand (SP) according to the Unified Soil Classification System (USCS).

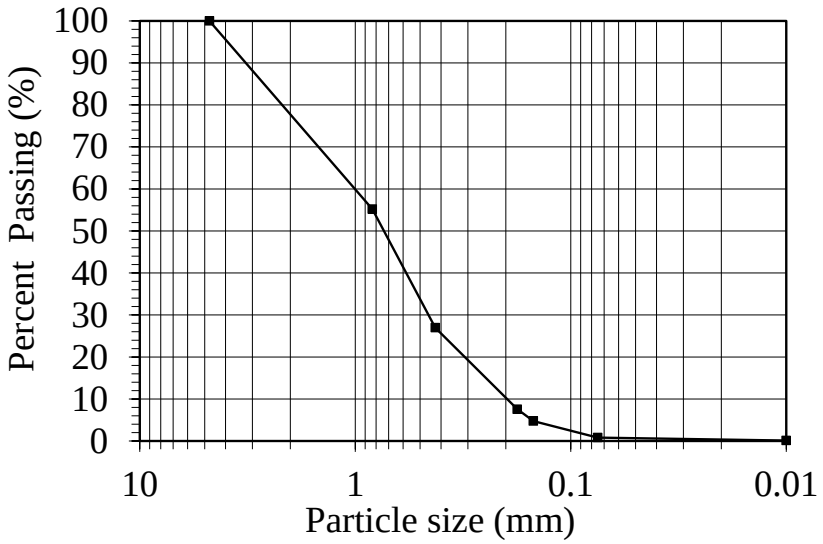

Figure 3.1: Grain size distribution of Mason sand

Table 3.1: Characteristic values from the Mason sand grain size distribution

Property	Value	Units
D_{10}	0.2	mm
D_{30}	0.44	mm
D_{60}	0.9	mm
C_u	4.5	
C_z	1.08	

3.2.2 Specific Gravity

The specific gravity G_s of the sand was measured according to ASTM D 854. To ensure quality and accuracy of the results, the test was repeated three times. The specific gravity is defined as the ratio between the mass of distilled, de-aired water at 20 °C in a volumetric flask to the mass of soil and distilled, de-aired water at 20 °C in the same flask. An average specific gravity of 2.62 was obtained for the Mason sand.

3.2.3 Minimum Void Ratio

The minimum void ratio (maximum dry density) e_{min} of the Mason sand was obtained by pouring oven dry sand into a cylindrical mold 101 mm in diameter and 116 mm high. A 0.91 kg

steel cylinder having the same diameter as the mold was placed on top of the sand layer and the entire assembly was vibrated using a mechanical vibrator for 12 minutes. At the end of vibration, the settlement of the sand layer was measured, and the volume of the sand cylinder was calculated. The dry density was calculated as follows:

$$\rho_d = \frac{m_s}{V} \qquad 3.1$$

where ρ_d is the dry density, m_s is the mass of the dry sand solids, and V is the volume of the sand after densification. This procedure was conducted three times to ensure repeatability of the test. $\rho_{d,max}$ was determined by taking the average of the three values of ρ_d calculated, and was found to be 1.74 kg/m^3. The minimum void ratio corresponding to the maximum dry density was calculated as follows:

$$e_{min} = \frac{\rho_w G_s}{\rho_{d,max}} - 1 \qquad 3.2$$

where ρ_w is the density of water, G_s is the specific gravity of the sand, and $\rho_{d,max}$ is the maximum dry density. $\rho_{d,max}$ was determined by taking the average of the three values of ρ_d calculated using Equation 3.1 for the three individual tests. The minimum void ratio was found to be 0.50.

3.2.4 Maximum Void Ratio

The maximum void ratio (minimum dry density) e_{max} was measured by pluviating 1000 grams of oven dry sand into a 1000mL graduated cylinder. The cylinder was capped, tipped upside down and carefully returned to the original vertical position. The volume was recorded and the minimum dry density was calculated using Equation 3.1. This procedure was repeated three times with a difference between calculated densities of less than 0.7%. The maximum void ratio corresponding to the minimum dry density was calculated as follows:

$$e_{max} = \frac{\rho_w G_s}{\rho_{d,min}} - 1 \qquad 3.3$$

where ρ_w and G_s are the density of water and specific gravity of the sand, respectively and $\rho_{d,min}$ is the calculated minimum dry density of the sand. The minimum dry density was found to be 1.47 kg/m^3 and the maximum void ratio was 0.78.

3.2.5 Shear Strength

A series of four consolidated undrained (CU) triaxial compression tests were performed on the Mason sand in accordance with ASTM D4767. A mechanical vibrator densified each specimen to a target void ratio of 0.54. The relative density corresponding to this void ratio can be calculated as follows:

$$I_d = \frac{\rho_d - \rho_{d,\min}}{\rho_{d,\max} - \rho_{d,\min}} \qquad 3.4$$

A value of I_d of 0.89 corresponds to the target void ratio, indicating that the sand is relatively dense. The specimen was prepared by placing the bottom platen of the triaxial cell on a shaking table, and pouring sand into the latex membrane fitted on the inside of a split mold. The sand was vibrated in three lifts until reaching the target void ratio. The top cap was then placed on the specimen, the membrane was attached, and the specimen was placed under vacuum. After assembly of the cell, the sand was saturated by applying a vacuum to top of the specimen and allowing water under atmospheric pressure to flow upward from the bottom. Once water started to flow from the top of the specimen, it was backpressure saturated until the measured value of Skempton's B parameter reached 0.9 or remained constant with additional incremental increases to the backpressure. The final B-values for each test are summarized in Table 3.2.

Table 3.2: Summary of saturation details

σ'_3 (kPa)	σ_{cell} (kPa)	σ_{back} (kPa)	B
35	310	276	0.8
70	310	276	0.8
201	310	276	0.8
420	310	276	0.74

After saturation, the sand specimens were consolidated to 34, 70, 207, or 420 kPa. After consolidation they were sheared in undrained conditions with pore water pressure measurement at the bottom of the specimen at a rate of 2.57 mm/min until reaching 15% axial strain. This shearing rate corresponds to a time to 15% axial strain of 20 minutes. The initial void ratios at the end of specimen preparation and void ratios after consolidation for each test are presented in Table 3.3. The results indicate that relatively small volume changes occurred during consolidation.

Table 3.3: Initial void ratios after specimen preparation and void ratios after consolidation for the triaxial compression tests on Mason sand

σ_{3c}' (kPa)	e_i	e_{consol}
34	0.54	0.54
70	0.54	0.54
207	0.55	0.54
420	0.54	0.53

During shearing, the principal stress difference, $(\sigma_1-\sigma_3)$, excess pore water pressure, Δu, and principal stress ratio, σ_1'/σ_3', were measured as a function of axial strain. The curves of principal stress difference with axial strain are shown in Figure 3.2, the curves of excess pore water pressure with axial strain are shown in Figure 3.3, and the curves of principal stress ratio with axial strain are shown in Figure 3.4.

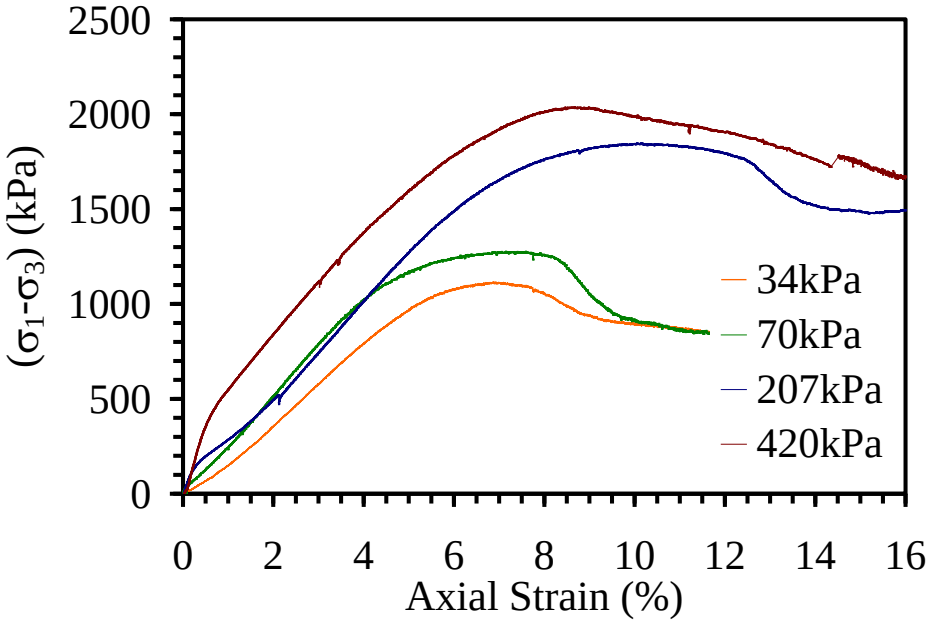

Figure 3.2: Principal stress difference with axial strain for standard triaxial compression tests on saturated Mason sand

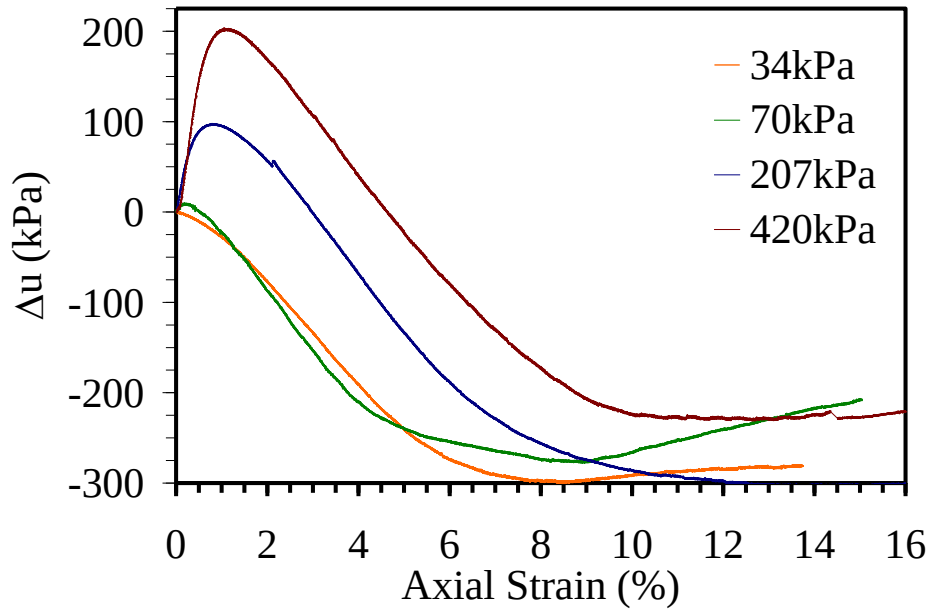

Figure 3.3: Excess pore water pressure with axial strain for standard triaxial compression tests on saturated Mason sand

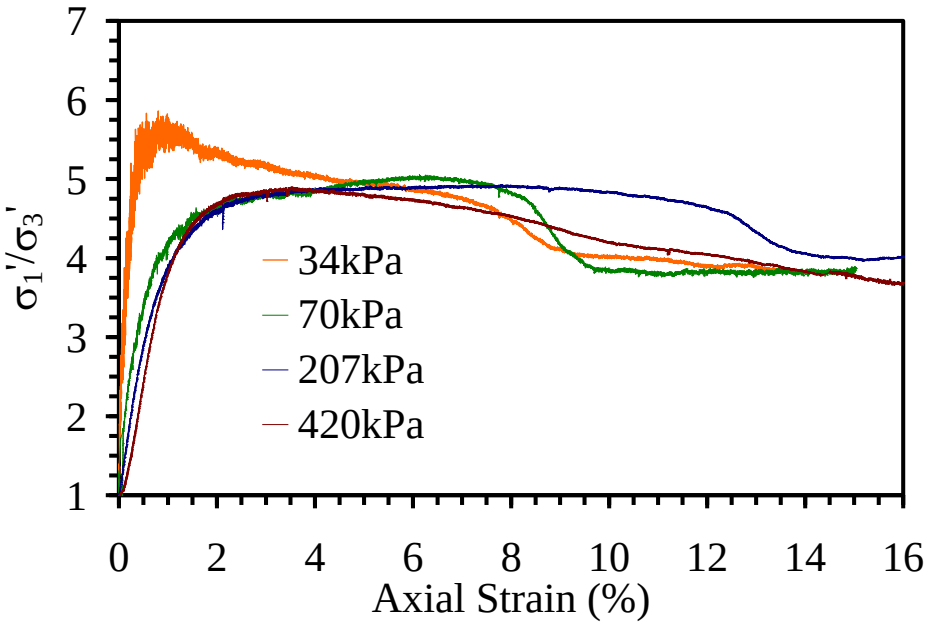

Figure 3.4: Principal stress ratio with axial strain for standard triaxial compression tests on saturated Mason sand

There are two criteria to define shear failure of a specimen during a consolidated undrained triaxial compression test. The first criterion defines failure as the point where the maximum value of internal friction is mobilized, which is referred to as the stress path tangency failure criterion. In a consolidated undrained triaxial compression test, the point where the maximum friction is mobilized occurs at the maximum value of the principal stress ratio, σ_1'/σ_3'. Examination of a Mohr circle at failure indicates that the principal stress ratio is directly proportional to the friction angle [$\sigma_1'/\sigma_3' = \tan^2(45+\phi'/2)$]. The second criterion defines failure as the point where the soil provides the maximum resistance to axial compression, which is referred to the maximum principal stress difference failure criterion. As the name indicates, this point is the point where the maximum principal stress difference is measured. In a consolidated drained shear strength test, these failure criteria occur at the same strain. However, in a consolidated undrained shear strength test, these points occur at different strains because the generation of

shear-induced pore water pressure causes a change in mean effective stress during shearing, which makes it easier or harder to compress the specimen axially.

Table 3.4: Summary of values at failure for Mason sand according to the stress path tangency failure criterion

σ_{3c}' (kPa)	$(\sigma_1'/\sigma_3')_f$	ε_f (%)	$(\sigma_1-\sigma_3)_f$ (kPa)	Δu_f (kPa)	σ_{3f}' (kPa)
34	5.51	0.8	125	-23	28
70	4.81	3.7	953	-195	250
207	4.86	4.0	1026	-71	266
420	4.87	3.5	1250	75	323

Table 3.5: Summary of values at failure for Mason sand according to the maximum principal stress failure criterion

σ_{3c}' (kPa)	$(\sigma_1'/\sigma_3')_f$	ε_f (%)	$(\sigma_1-\sigma_3)_f$ (kPa)	Δu_f (kPa)	σ_{3f}' (kPa)
35	4.78	6.9	1113	-289	294
70	4.91	7.7	1267	-269	324
210	4.81	10.2	1843	-288	483
420	4.40	8.8	2033	-200	598

The stress paths in modified Mohr-Coulomb stress space (effective confining stress versus principal stress difference) for Mason sand specimens consolidated to different initial consolidation stresses are shown in Figure 3.5(a) and Figure 3.5(b). The points of failure of each specimen are identified in Figure 3.6(a) with hollow diamonds for stress path tangency failure criterion and in Figure 3.6(b) with hollow squares for maximum principal stress difference failure criterion.

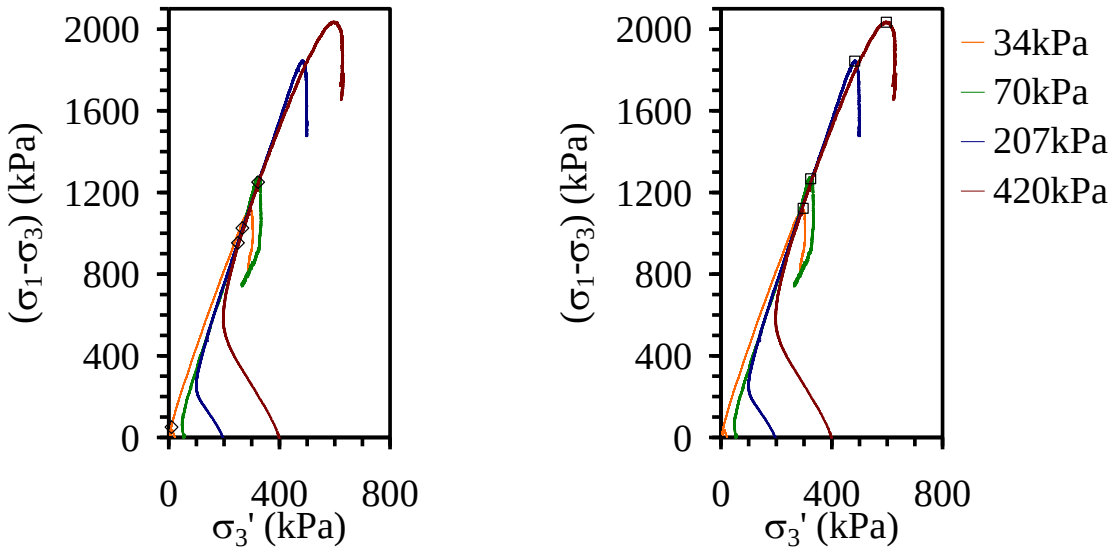

(a) (b)

Figure 3.5: Mason sand stress paths in triaxial stress space: (a) Points of failure corresponding to stress path tangency are indicated by the hollow diamonds; (b) Points of failure corresponding to maximum principal stress difference are indicated by a hollow square.

The failure envelopes for each of the failure criteria in triaxial stress space can be determined by fitting a line through the four failure points. The angle of inclination of this line corresponded to the transformed friction angle, α while the y-intercept corresponded to the transformed apparent cohesion, d as shown in Figure 3.6.

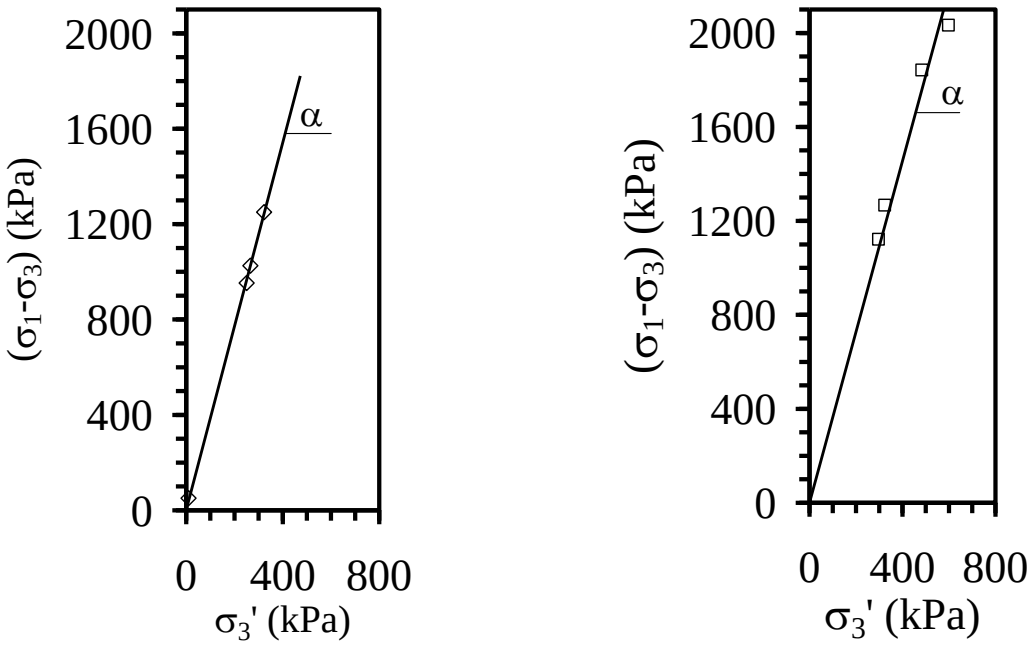

Figure 3.6: Mason sand failure envelopes in triaxial stress space: (a) Stress path tangency failure criterion; (b) Maximum principal stress failure criterion

The following equations were used to convert the modified Mohr-Coulomb parameters of the failure envelope to the conventional Mohr-Coulomb values of c' and ϕ', as follows:

$$\phi' = \sin^{-1}\left(\frac{\tan(\alpha)}{2 + \tan(\alpha)}\right) \qquad 3.5$$

$$c' = \frac{d\,(1 - \sin(\phi'))}{2\cos(\phi')} \qquad 3.6$$

where ϕ′ is the effective angle of internal friction and c′ is the apparent cohesion. The values of α and d determined from the data presented in Figure 3.6 are summarized in Table 3.6. This table also includes the values of ϕ′ and c′ calculated using Equations 3.5 and 3.6.

Table 3.6: Summary of shear strength parameters in transformed triaxial stress space and Mohr-Coulomb failure envelope parameters

Failure criterion	Modified Mohr-Coulomb			Mohr-Coulomb		
	Parameter	Value	Units	Parameter	Value	Unites
Stress path	α	68.5	degrees	ϕ'	69.0	degrees
tangency	d	0	kPa	c'	0	kPa
Maximum	α	34.0	degrees	ϕ'	34.5	degrees
principal stress	d	0	kPa	c'	0	kPa

3.2.6 Mason Sand Soil Water Retention Curve (SWRC)

To determine the degree of saturation suction relationship of Mason sand, two different methods were used to determine the soil water retention curve (SWRC) for Mason sand: a flow pump permeameter and the hanging column technique. The flow pump technique is discussed in detail by McCartney and Znidarčić (2010) and the hanging column technique was performed in accordance with ASTM 6836 method A. The SWRCs determined using both methods included both the wetting and drying paths for the sand. The SWRCs for Mason sand using both techniques during wetting and drying are shown in Figure 3.7.

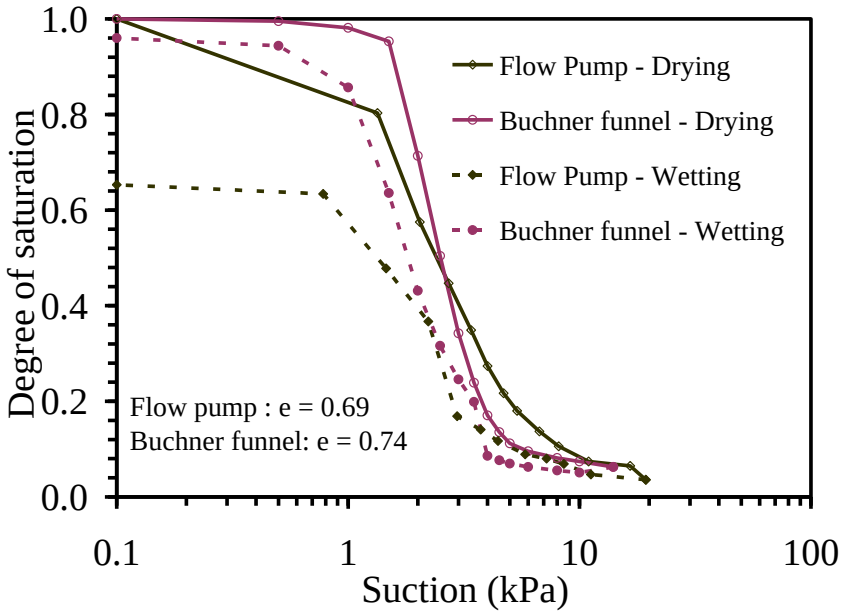

Figure 3.7: SWRCs for Mason sand using the flow pump technique as well as the hanging column (Büchner funnel) for both wetting and drying

3.3 Boulder Clay

The results from the soil characterization testing program for Boulder clay are presented in this section, including the Atterberg limits, grain size distribution, specific gravity, standard Proctor compaction, oedometer, and swell potential. The shear strength of Boulder clay is also summarized in this section, including the results from a series of consolidated undrained triaxial

compression tests performed under the conventional, slow shearing rates, as well as faster shearing rates. The last section presents the results for the soil water retention curve (SWRC) and the corresponding van Genuchten (1980) SWRC parameters and hydraulic conductivity function.

3.3.1 Soil Preparation

The clay used for the Atterberg limit and hydrometer test was air dried, ground using a mortar and pestle, passed through a #200 sieve and then the material was mixed with tap water to create a paste. This paste was allowed rest for 24 hours before being used for testing. For all tests other than Atterberg limits and hydrometer, the following procedure was used to process the Boulder clay. The clay was air-dried and ground using either a mechanical soil grinder or mortar and pestle, then passed through a #10 sieve. The processed soil was then moisture conditioned to the desired water content, which varied depending on the tests. The clay before processing is shown in Figure 3.8(a) and after processing in Figure 3.8(b).

(a) (b)

Figure 3.8: Boulder clay before processing (a) and after processing (b)

3.3.2 Hydrometer

The grain size distribution for Boulder clay was performed in accordance with ASTM D 422. For particle sizes smaller than 75 μm (particles passing #200 sieve), the grain size distribution was determined by hydrometer analysis. The results of the analysis and physical properties are

shown in Figure 3.9 and the key parameters from the grain size distribution are summarized in Table 3.7.

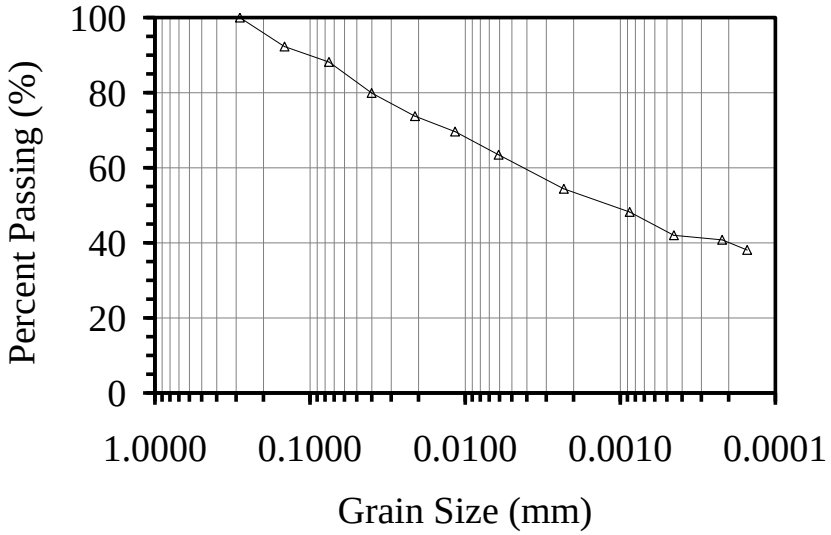

Figure 3.9: Grain size distribution for Boulder clay

Table 3.7: Characteristics of the grain size distribution for Boulder clay

Property	Value	Units
D_{10}	< 0.00015	mm
D_{30}	<0.00015	mm
D_{50}	0.0012	mm
% Passing No. 200 Sieve	90	%
% Clay size < 4 μ	60	%
% Clay size < 2 μ	54	%
% Silt size	40	%
% Sand size	0	%

3.3.3 Atterberg Limits

The liquid and plastic limits for the clay were performed in accordance with ASTM D4318. The results are summarized in Table 3.8. From the results, the clay was classified as low plasticity clay (CL) according to the Unified Soil Classification System (USCS).

Table 3.8: Atterberg limits of Boulder clay.

Liquid Limit (LL)	Plastic Limit (PL)	Plasticity Index (PI)
43	21	22

In addition to the Atterberg limits, the activity of Boulder clay was calculated as follows:

$$A = \frac{PI}{\%\ ClaySizedP\quad articles} \qquad 3.7$$

where PI is the plasticity index and "% of clay sized particles" is the percentage of particles by mass less than 0.02 mm. The activity of Boulder clay was calculated to be 0.29. Clays having activity values less than 0.75 are classified as inactive, and Boulder clay falls into this category.

3.3.4 Specific Gravity

A volumetric flask method was used to measure the specific gravity of Boulder clay in accordance to ASTM D854. This test was repeated three times, and an average specific gravity of 2.70 was measured.

3.3.5 Compaction Curve

The compaction curve for Boulder clay was determined using the standard Proctor compaction effort in accordance to ASTM D698 at the University of Tennessee, Knoxville. The results from this test shown in Figure 3.10 indicate that maximum dry density and corresponding optimum water content are 17.6 kN/m^3 and 16.8%, respectively. The soil specimens in the triaxial testing program were all compacted, so this curve is an important reference.

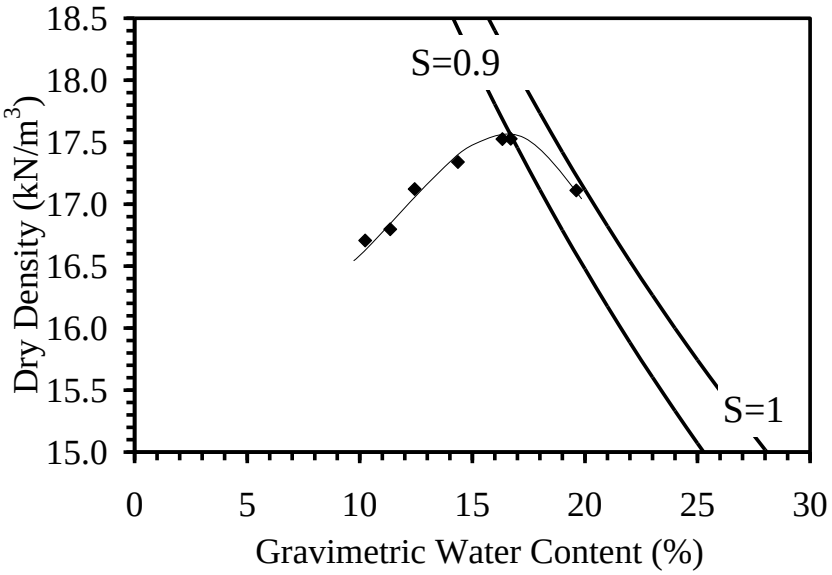

Figure 3.10: Results of the standard Proctor compaction test for Boulder clay

3.3.6 Compression Curve and Consolidation Characteristics

To determine the compression curve and consolidation characteristics of Boulder clay, a one dimensional consolidation test was performed in an oedometer in accordance to ASTM D2435, Method A. The specimen, which had a diameter of 63.5 mm and height of 26.7 mm, was inundated with tap water after application of a seating load of 3 N. The axial stress was increased using a pneumatic loading piston in to apply values of 9, 18, 46, 92, 183, 367, 733, and 1283 kPa to the specimen. After the maximum load was applied, an unloading sequence of 642, 275, 138, 64, 18, and 9 kPa was applied to the specimen. The vertical deformation of the specimen was allowed to equilibrate under each load increment for 24 hours before the next increment was applied.

A load-deformation analysis was performed to estimate the apparent preconsolidation stress (σ_{pc}'), compression index (c_c) and recompression index (c_r). The equilibrium void ratio values calculated from the LVDT measurements in the oedometer test were plotted against the logarithm of stress as shown in Figure 3.11. Using this figure, the apparent preconsolidation

stress of the compacted clay was estimated using Casagrande's method (i.e., intersection of tangent lines fitted to the slope of the curve during initial loading and the slope of the curve in the normally consolidated region). The graphical construction created to determine the apparent preconsolidation stress, σ_{pc}' is shown in the figure, with Point A signifying the apparent preconsolidation stress of the compacted soil.

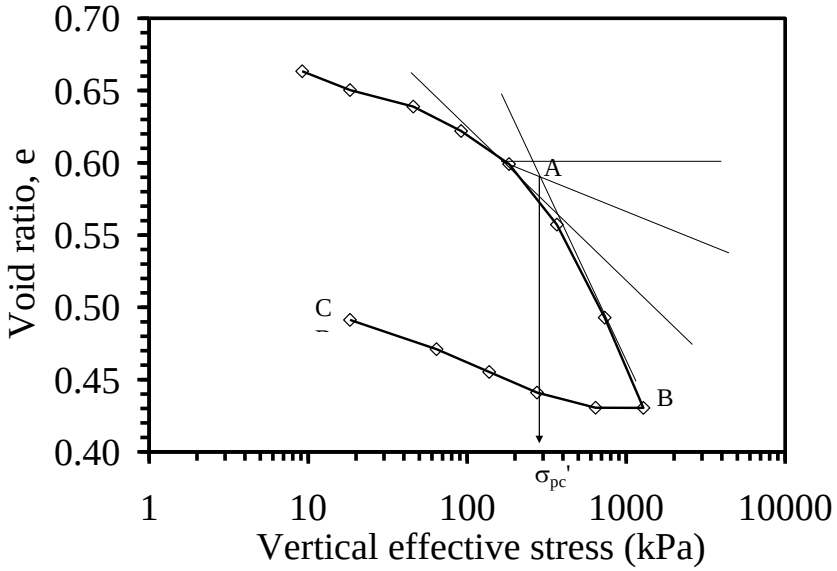

Figure 3.11: Compression curve used to determine the apparent pre-consolidation stress (σ_{pc}') using Casagrande's fitting method.

The compression index, c_c, and recompression index, c_r, were calculated as follows:

$$c_c = \frac{e_0 - e_{pc}}{\log(\sigma_{pc}' / \sigma_{v0}')} \qquad 3.8$$

$$c_r = \frac{e_1 - e_{pc}}{\log(\sigma_{pc}' / \sigma_{v1}')} \qquad 3.9$$

where σ_{v0}' is the effective stress on the log-linear portion of the virgin compression (line AB – Figure 3.11), σ_{v1}' is the final effective stress along the recompression (line BC – Figure 3.11). The values of e_0, e_1, and e_{pc} are the void ratios corresponding to σ_{v0}', σ_{v1}', and σ_{pc}' respectively. The results from the load-deformation analysis are summarized in Table 3.9.

Table 3.9: Load deformation properties of Boulder Clay

Parameter	Value	Units
c_c	0.233	\
c_r	0.041	\
σ_{pc}'	300	kPa

ASTM D2435 Method A specifies that readings of the time rate of deformation be taken during every load increment. As a result, the consolidation curve on a log-scale plot was used to estimate the coefficient of consolidation, c_v, for the 46, 92, 183, 367, 733, and 1283 kPa load increments. An example consolidation curve for the load increment from 73 to 1283 kPa is shown in Figure 3.12. The time corresponding to 50% consolidation for each increment was determined using the log-time method specified in ASTM D2435. The construction for determining the time to 50% consolidation (t_{50}) is also shown in Figure 3.12.

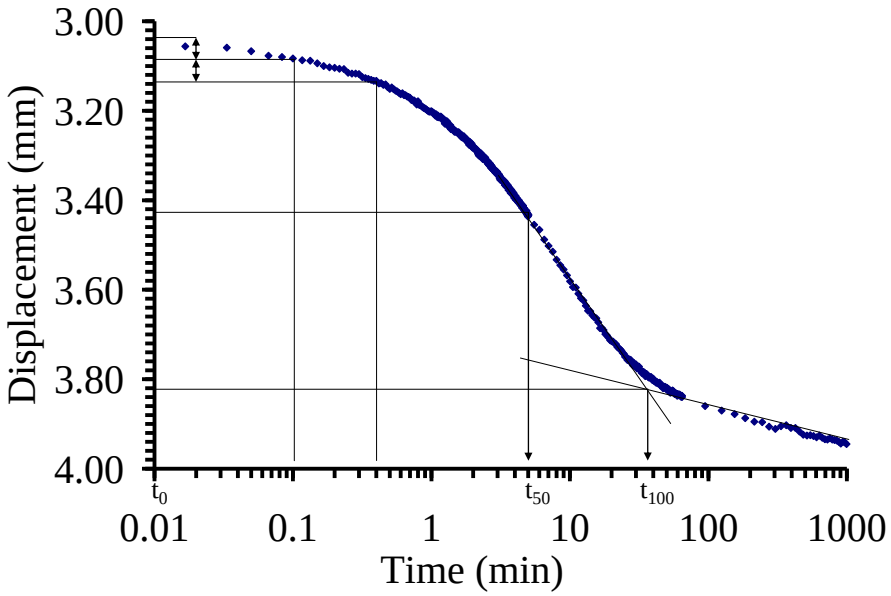

Figure 3.12: Representative time-deformation data during increment in axial stress from 733 to 1283 kPa using the log-time method for determining t_{50}

From the log-time analysis, the coefficient of consolidation, c_v, was calculated as follows:

$$c_v = \frac{0.196\ h^2}{t_{50}} \qquad 3.10$$

where h is half the average thickness of the sample during the load increment since and t_{50} was the time to reach an average degree of consolidation of 50%. Table 3.10 summarizes the time-deformation results for each load increment ranging from 46 to 1283 kPa.

Table 3.10: Time-deformation parameters for Boulder clay for different stress increments

Stress Increment (kPa)	46	92	183	367	733	1283
t_{50} (min)	0.1	0.6	0.9	1.0	2.5	4.0
c_v (mm^2/min)	38.0	5.61	3.65	3.16	1.18	0.68
$e_{initial}$	0.65	0.64	0.62	0.60	0.56	0.49
e_{final}	0.64	0.62	0.60	0.56	0.49	0.43

3.3.7 One-Dimensional Swell Potential

A one-dimensional swell test was performed in accordance with ASTM D4565 method A to measure the Boulder clay swell potential. A clay specimen was prepared using a mechanical press to reach a dry unit weight of 16.8 kN/m^3. The initial and final specimen details are provided in Tables 3.11 and 3.12 respectively. The specimen was placed in an oedometer, inundated with tap water then allowed to swell vertically under a 1 kPa seating load until primary swell had occurred. At the end of primary swell, the specimen was incrementally loaded until the initial void ratio had been reached. Each load increment was applied for 24 hours, which was sufficient for the change in height to reach an equilibrium value. The vertical stresses applied to the specimen during each increment were 2, 9, 18, 37, 73 and 147 kPa.

Table 3.11: Initial specimen details for 1D swell test on Boulder clay

$m_{initial}$ (gr)	$h_{initial}$ (mm)	$d_{initial}$ (mm)	$V_{initial}$ (cm^3)	$w_{initial}$ (%)	$e_{initial}$
169.6	26.7	63.5	84.6	17.2	0.58

Table 3.12: Final specimen details for 1D swell test on Boulder clay

m_{final} (gr)	h_{final} (mm)	d_{final} (mm)	V_{final} (cm^3)	w_{final} (%)	e_{final}
175.9	26.0	63.5	83.6	22.0	0.56

A summary of the percent swell during each stress increment is provided in Table 3.13. To determine the swell pressure, the void ratio at the end of each stress period was plotted versus to logarithm of stress (see Figure 3.13). The vertical stress required to cause the specimen to return to the initial void ratio at the beginning of the test corresponds to the swell pressure, σ_{sp}.

Table 3.13: Stress increment summary of 1D swell test

Stress Increment (kPa)	Height of specimen at end of load phase (mm)	Void ratio at end of load phase	% Heave
2	26.70	0.58	0.00
2	27.74	0.64	3.89
9	27.65	0.63	3.57
18	27.53	0.63	3.12
37	27.31	0.61	2.27
73	26.93	0.59	0.84
147	26.40	0.56	-1.12

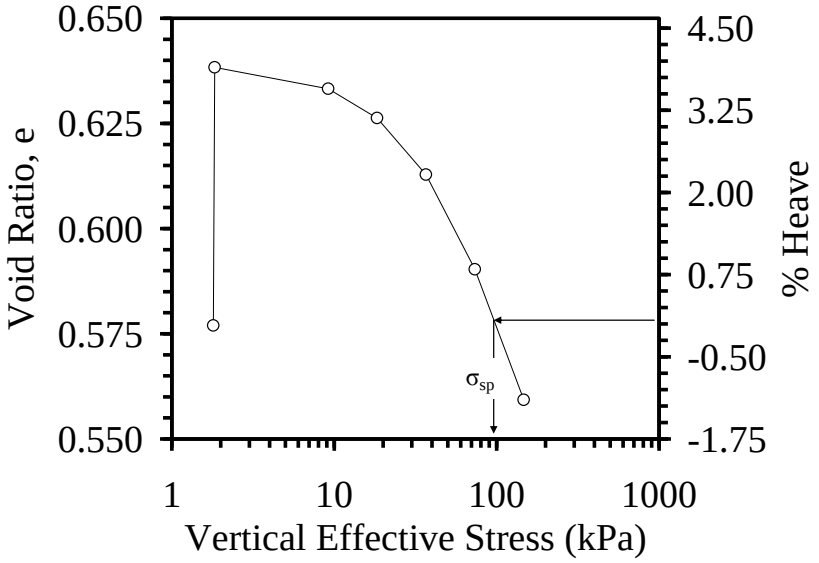

Figure 3.13: Void ratio and percent heave versus log stress curve

Another important parameter determined through the 1D swell test results is the expansion index. The expansion index is calculated as follows:

$$EI = 1000 * h * F \quad (3.11)$$

where EI is the expansion index, h is the expansion of the soil during free swell in inches, and F is the percent of soil passing a #4 sieve. For this test, h was 1 mm and F equals 100%. The calculated expansion index is 41. An EI between 21 and 50 is classified as having low potential for expansion. As a result, Boulder clay can be considered to have a low potential for expansion. A summary of all 1D test results is provided in Table 3.14.

Table 3.14: Summary of 1D test expansion test results for Boulder clay

Parameter	Value	Unit	Comment
e_i	0.58		Initial void ratio
e_f	0.56		Final Void ratio
σ_{se}	1.0	kPa	Seating Pressure
e_{se}	0.64		Void ratio at end of free swell
% heave(max)	3.89	%	Maximum heave at end of free swell
σ_{sp}	100	kPa	Swell Pressure
EI	41		EI between 21-50 is classified as low potential for expansion

3.3.8 Shear Strength

Five consolidated undrained (CU) triaxial tests were conducted in accordance to ASTM D4767-02 to determine the shear strength parameters of the Boulder clay. Each specimen was compacted using a mechanical press into a cylindrical mold that is 71.1 mm high having a 35.6 mm diameter. To ensure uniformity throughout the sample, each specimen was compacted using five lifts of equal mass. This method of compaction is referred to as “static compaction”. A typical specimen after compaction is shown in Figure 3.14. The target dry unit weight and water content for each specimen was 17 kN/m3 and 17.5% respectively, which correspond to 0.6% of the maximum standard Proctor dry density and 10% dry of the standard Proctor optimum water content.

Once the specimen was prepared, it was saturated using the following procedure. First, vacuum was applied to both the top and bottom of the sample for two hours under a seating cell pressure of 35 kPa. Then water was allowed to free flow under atmospheric pressure to the bottom of the sample while vacuum was applied to the top of the specimen. Once water started to flow out from the top of the sample, the confining stress was increased to 70 kPa and a water backpressure of 35 kPa was applied to both the top and bottom of the sample. To complete the saturation process, the backpressure and cell pressure were increased in stages until the measured value of Skempton's B parameter reached a value of at least 0.9 or remained constant until there was no additional increase in the B value with increased stress increments. A summary of the final cell pressures, back pressures and B values is provided in Table 3.15.

Table 3.15: Summary of saturation details

σ_{3c}' (kPa)	σ_{cell} (kPa)	σ_{back} (kPa)	B
34	448	414	0.80
69	483	448	0.86
207	586	552	0.82
414	379	379	0.80
552	207	172	0.78

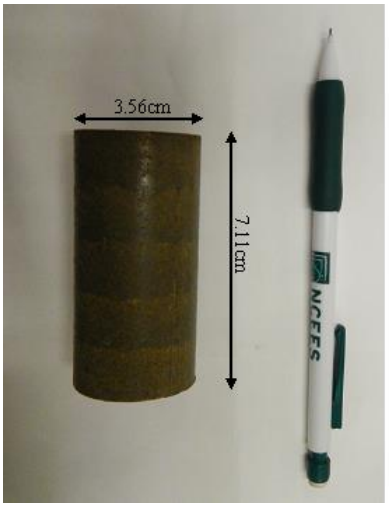

Figure 3.14: Typical 35.6 mm-diameter specimen of compacted Boulder clay.

After saturation, the specimens were consolidated to different effective stress values of 35, 70, 210, 420, or 560 kPa. The consolidation stress was applied for 24 hours or until the volume change inferred from the cell water level and backpressure water levels reached equilibrium. At least 90% of consolidation was obtained during for each consolidation stress. Upon completion of the consolidation phase, each sample was sheared to 15% strain in 150 minutes at a rate of 0.0686 mm/min. This time to 15% axial strain (and corresponding shearing rate) was defined using the value of t_{50} for the soil specimens following ASTM D4767. The initial water contents and void ratios after compaction (w_i and e_i) as well as the void ratios after consolidation (e_{consol}) are provided in Table 3.16.

Table 3.16: Boulder clay initial water contents and void ratios after specimen preparation and void ratios after consolidation

σ_{3c}' (kPa)	w_i (%)	e_i	e_{consol}
34	17.6	0.52	0.52
69	18	0.49	0.48
207	17.3	0.51	0.46
414	17.8	0.54	0.48
552	16.8	0.57	0.51

During shearing, the principal stress difference (σ_1-σ_3), excess pore water pressure Δu, and principal stress ratio σ_1'\σ_3' were measured as a function of axial strain. The curves of principal stress difference are shown in Figure 3.15, the curves of excess pore water pressure are shown in Figure 3.16, and the curves of principal stress ratio are shown in Figure 3.17.

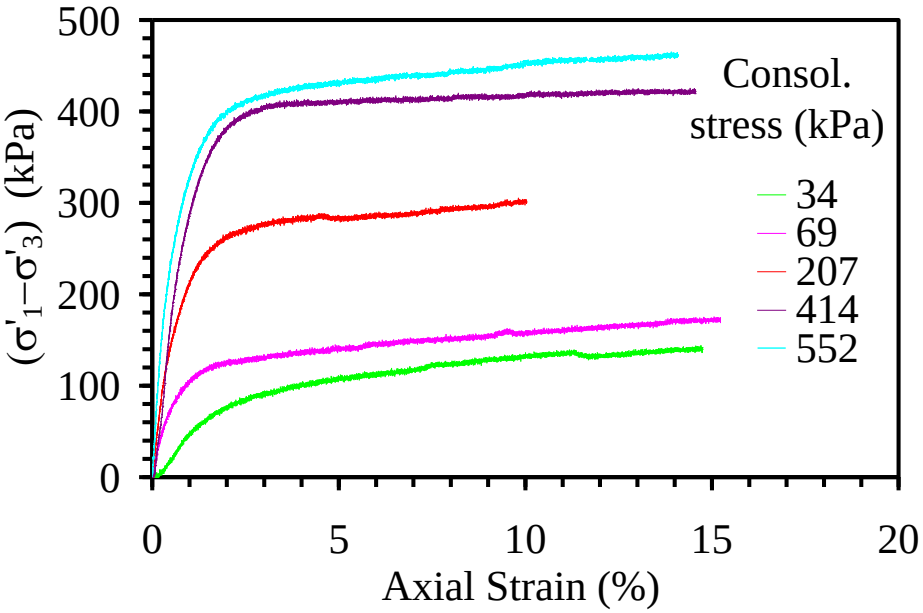

Figure 3.15: Principal stress difference with axial strain for standard triaxial compression tests on saturated Boulder clay

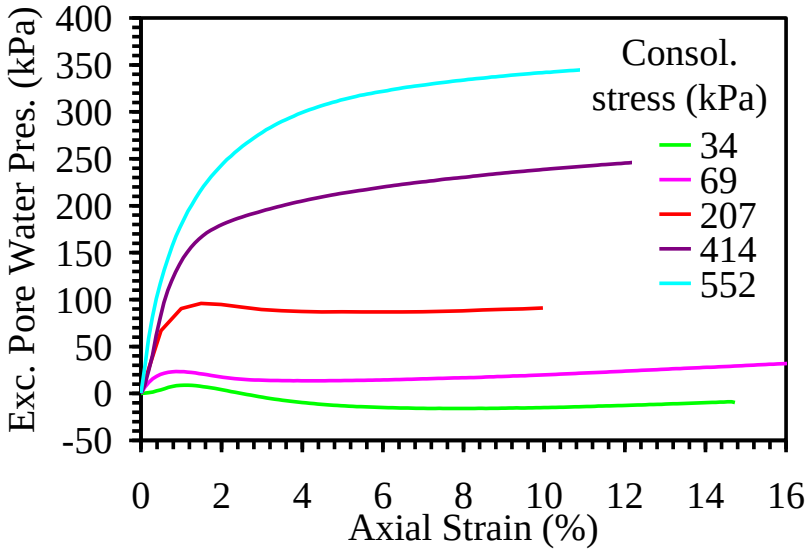

Figure 3.16: Excess pore water pressure with axial strain for standard triaxial compression test on saturated Boulder clay

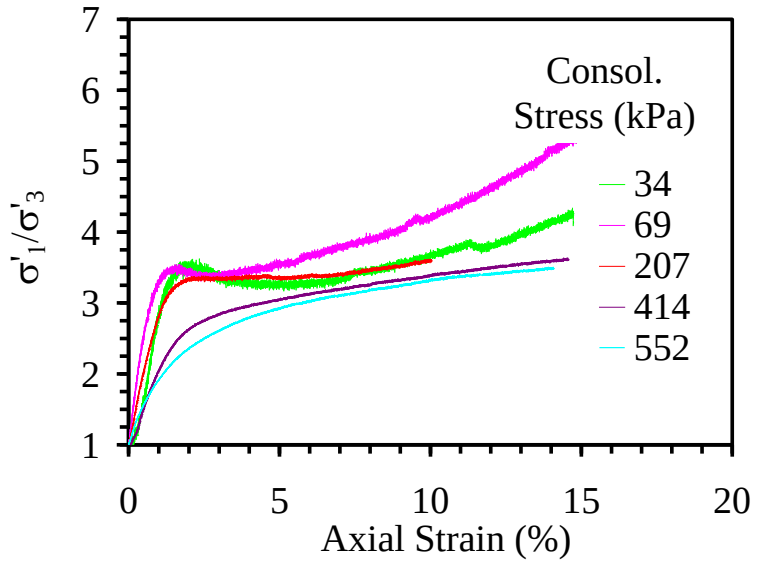

Figure 3.17: Principal stress ratio with axial strain for standard triaxial compression test performed on saturated Boulder clay

Failure was defined using both stress path tangency and maximum principal stress difference failure criterion. Stress path tangency criterion corresponds to the point of maximum mobilized internal friction. The principal stress difference at failure for each test corresponds to the point where the principal stress ratio reaches a maximum. The point of failure using maximum principal stress difference criterion corresponds to the point where the maximum resistance to shearing of the soil has been reached. This point is identified as the point where the maximum principal stress difference has been reached. To determine the parameters for the Mohr-Coulomb failure envelope, the principal stress difference of each test was plotted versus the corresponding minor principal effective stress as shown in Figure 3.18. The failure points, identified with a hollow diamond shape, using stress path tangency criterion are shown in Figure 3.18(a). The failure points, identified with hollow squares, using maximum principal stress difference failure criterion are shown in Figure 3.18(b).

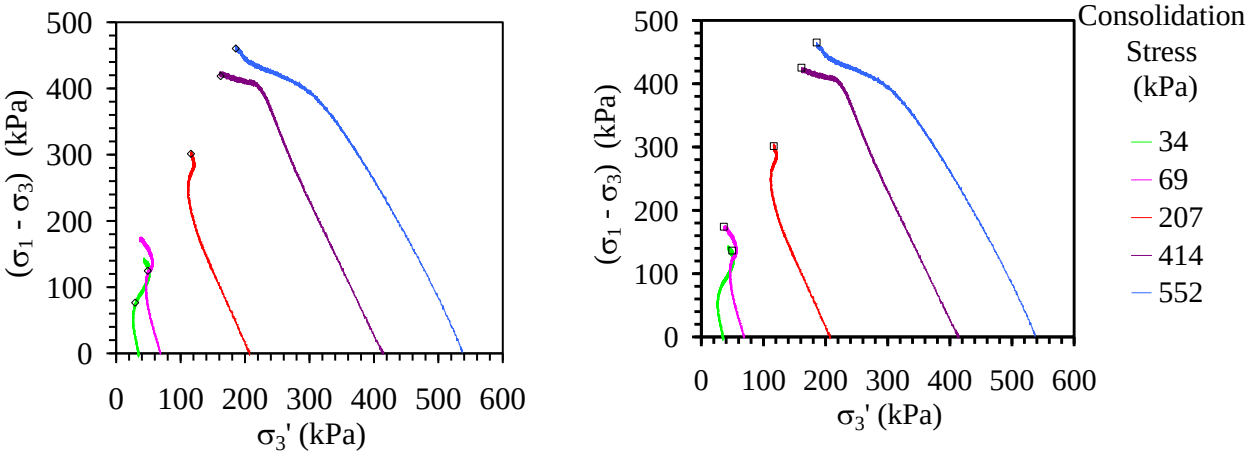

(a) (b)

Figure 3.18: Boulder clay stress paths in triaxial stress space: (a) Points of failure corresponding to stress path tangency are indicated by the hollow diamonds; (b) Points of failure corresponding to maximum principal stress difference are indicated by a hollow square

The principal stress ratio at failure versus minor principal effective stress at failure is shown in modified Mohr-Coulomb stress space in Figure 3.19, along with failure envelopes for stress path tangency [Figure 3.19(a)] and maximum principal stress difference [Figure 3.19(b)]. The angle of inclination of the failure envelope in triaxial stress space, α was calculated to be 68° while the y-intercept, d, was found to be zero. The value of α corresponds to a drained friction angle of 33° using Equation 3.5 and effective cohesion of zero using Equation 3.6. All values at failure for axial strain, minor principal stress, principal stress difference, principal stress ratio, and excess pore water pressure using stress path tangency criterion are provided in Table 3.17 and for maximum principal stress difference criterion in Table 3.18. The shear strength parameters are summarized in Table 3.19.

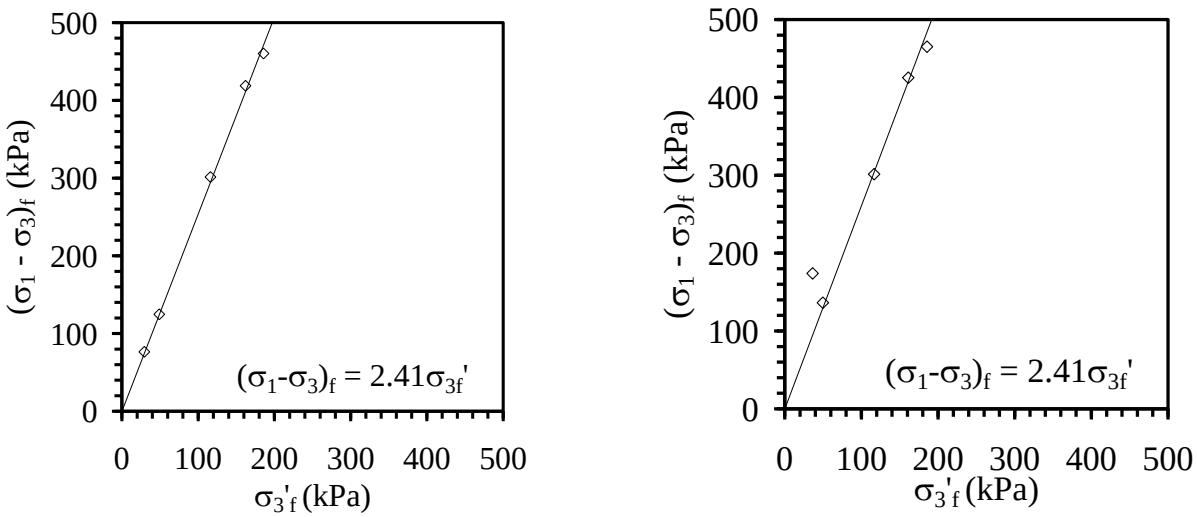

Figure 3.19: Boulder clay failure envelopes in triaxial stress space: (a) Stress path tangency failure criterion; (b) Maximum principal stress failure criterion

Table 3.17: Consolidation stress, axial strain, minor principal stress, principal stress difference, principal stress ratio and excess pore water pressure at failure using stress path tangency failure criterion.

σ_{3c}' (kPa)	e_f	σ_{3f}' (kPa)	$(\sigma_1-\sigma_3)_f$ (kPa)	$(\sigma_1'/\sigma_3')_f$	Δu_f (kPa)
34	1.90	30	77	3.48	5
69	1.60	49	125	3.49	20
207	10.03	116	301	3.60	91
414	14.60	162	419	3.63	253
552	14.10	186	460	3.49	548

Table 3.18: Consolidation stress, axial strain, minor principal stress, principal stress difference, principal stress ratio and excess pore water pressure at failure using maximum principal stress difference failure criterion.

σ_{3c}' (kPa)	e_f	σ_{3f}' (kPa)	$(\sigma_1-\sigma_3)_f$ (kPa)	$(\sigma_1'/\sigma_3')_f$	Δu_f (kPa)
34	15	50	136	4.09	-10
69	15	36	174	5.79	33
207	10	117	301	3.60	91
414	15	161	425	3.63	253
552	15	186	465	3.51	351

Table 3.19: Summary of Boulder clay shear strength parameters using stress path tangency failure criterion

Failure criterion	Modified Mohr-Coulomb			Mohr-Coulomb		
	Parameter	Value	Units	Parameter	Value	Unites
Stress path tangency	α	68.5	degrees	ϕ'	69.0	degrees
	d	0	kPa	c'	0	kPa
Maximum principal stress	α	34.0	degrees	ϕ'	34.5	degrees
	d	0	kPa	c'	0	kPa

Given the scatter in the data points representing failure at maximum principal stress difference than the point representing failure at stress path tangency the stress path tangency failure criterion is a better representation of the shear strength of Boulder clay.

3.3.9 Soil Water Retention Curve (SWRC) and Hydraulic Conductivity Function (HCF)

The soil water retention curve (SWRC) of the Boulder clay was measured using two different methods: the axis translation technique incorporated into a flexible-wall permeameter that represent the equilibrium conditions for the triaxial compression tests on unsaturated specimens (discussed in Section 6.2) and the vapor equilibrium technique. Further, the hydraulic conductivity of a saturated specimen of Boulder clay was measured using a flexible-wall permeameter that incorporates a flow pump for controlling the flow rate (McCartney and Znidarcic (2010). The Boulder clay specimen for the hydraulic conductivity test was prepared by first mixing loose air dried material with water to obtain a gravimetric water content of 17.5%. Static compaction was used to form a cylindrical specimen with a void ratio of 0.49 (target 0.51). Compaction was performed in a single 25.9 mm-thick lift in a 63.8 mm-diameter split mold. The properties of the clay specimen are summarized in Table 3.20.

Table 3.20: Summary of specimen characteristics used for hydraulic conductivity measurement

Property	Value	Units
Height	25.9	mm
Diameter	63.8	mm
w	17.4	%
ρ_d	1737	kg/m^3
n	0.33	-
e	0.49	-

To measure the hydraulic conductivity, a flow pump was used to draw water out of the bottom of the specimen. After compaction of the specimen to the target dry density, backpressure saturation was used to saturate the specimen within the flexible wall permeameter. After saturation of the specimen under a backpressure of 330 kPa, the specimen was consolidated to an initial effective confining stress of 50 kPa (i.e., a cell pressure of 350 kPa and a backpressure of 300 kPa). At this point, the saturated hydraulic conductivity was determined by applying three different velocities of 0.0001, 0.0005 and 0.001 mm/sec across the specimen using the flow pump. The difference in head between the top and bottom of the specimen for each rate was measured using a differential pressure transducer (DPT). The hydraulic gradient, i, could then be calculated by dividing the difference in head by the height of the specimen. The flow rate through the specimen was calculated as follows:

$$Q = vA \tag{3.12}$$

where Q is the flow rate, v is the velocity, A is the cross sectional area of the specimen. Darcy's law indicates that the seepage velocity is equal to the negative of the hydraulic conductivity (k) times the gradient (i). Accordingly, the saturated hydraulic conductivity can be calculated by rearranging Darcy's law, as follows:

$$k_{sat} = -\frac{Q}{i} \times \frac{1}{A} \tag{3.13}$$

where Q/i is the slope of the best fit line through the points of flow rate versus hydraulic gradient as shown in Figure 3.20 divided by the cross sectional area of the soil specimen. The saturated hydraulic conductivity of Boulder clay was calculated to be 6.92×10^{-10} m/sec.

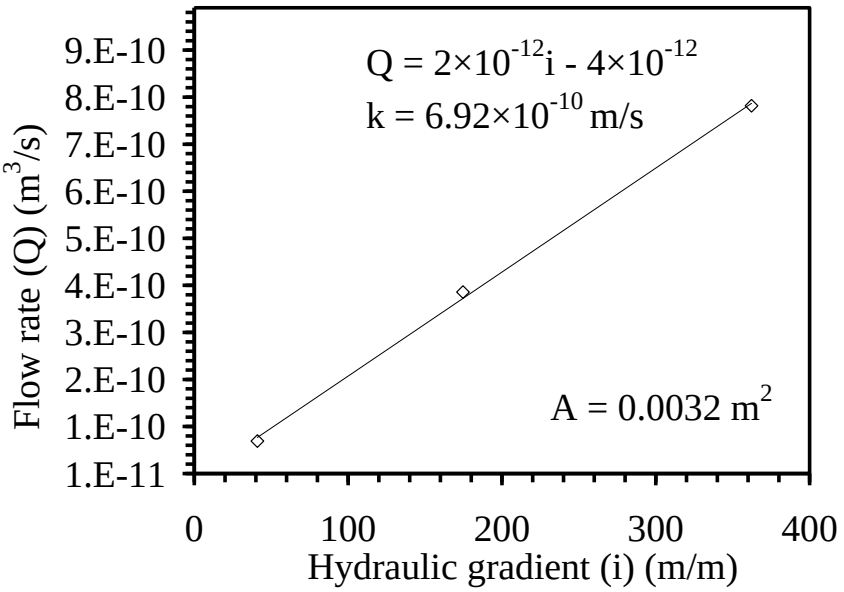

Figure 3.20: Flow rate versus gradient in the flow pump test to determine the hydraulic conductivity

The suction in the triaxial compression tests was controlled using the axis translation technique. In the axis translation technique, the suction in the specimen is equal to the difference between the pore air and pore water pressures. Specifically, the air pressure applied to the specimen is greater than the water pressure applied to the specimen. This is achieved through the use of a high air ceramic disk at the bottom of the specimen. The high air entry ceramic disk only permits passage of water, not air, until the difference between air and water pressure is equal to air entry value of the ceramic disk.

The equilibrium points determined through triaxial testing were found by measuring the outflow of water from a saturated triaxial specimen after applying a know suction of either 34

kPa or 140 kPa. This outflow could them be correlated using the following equation to determine the corresponding degree of saturation.

$$S = 1 - \frac{V_{out} G_s \rho_w}{e \rho_d V_f} \qquad 3.14$$

where S is the degree of saturation after application of a specific suction, V_{out} is the outflow from the triaxial specimen, G_s is the specific gravity and ρ_w is the density of water. V_f, e, and ρ_d are the specimen volume, void ratio and dry density after consolidation.

To determine SWRC points at total suctions greater than 10 MPa, the vapor equilibrium technique (Delage et al. 2008) was used. The total suction in this technique is controlled by applying a constant relative humidity to the air around a specimen in a tightly sealed desiccator. The relative humidity is controlled by placing a saturated salt solution into the desiccator along with the soil specimen. The equilibrium points from the axis translation technique applied in the triaxial tests and the vapor equilibrium techniques are given in Table 3.21.

Table 3.21: Experimental equilibrium points of degree of saturation and volumetric water content from the different SWRC tests and van Genuchten (1980) theoretical degree of saturation and volumetric water content

Technique	Suction (kPa)	Experimental results Degree of saturation	Experiemental results Volumetric water conent	van Genuchten Degree of saturation	van Genuchten Volumetric water content	Differences squared
Triaxial	34	0.94	0.31	0.97	0.32	0.001
	34	0.96	0.32	0.97	0.32	0.000
	140	0.91	0.30	0.89	0.29	0.000
	140	0.89	0.29	0.89	0.29	0.000
Vapor Equilibrium	22000	0.46	0.15	0.43	0.14	0.001
	65000	0.38	0.12	0.36	0.12	0.000
	74000	0.43	0.14	0.35	0.12	0.006
	84000	0.42	0.14	0.35	0.11	0.005
	164000	0.28	0.09	0.31	0.10	0.001

The van Genuchten (1980) SWRC model was fitted to the primary drainage path. The van Genuchten (1980) SWRC is given as follows:

$$\theta = \theta_r - (\theta_s - \theta_r)[1 + (\alpha_{vG}\psi)^{n_{vG}}]^{-\left(1-\frac{1}{n_{vG}}\right)} \quad 3.15$$

The value of θ_s corresponds to the porosity measured from compaction, while the residual water content θ_r was assumed to be zero. The values of α_{vG} and n_{vG} were determined using least squares regression to match the equilibrium SWRC data points. The SWRC points from the axis translation technique applied in the triaxial cell and vapor equilibrium tests along with the fitted van Genuchten SWRC are shown in Figure 3.22. The SWRC shown in Figure 3.22 is consistent with that of a clay with a relatively high air entry value of about 50 kPa. The best-fit van Genuchten (1980) SWRC parameters are summarized in Table 3.22.

Table 3.22: Summary of van Genuchten (1980) SWRC fitting parameters

Parameter	Drying
θ_s	0.329
θ_r	0.000
α_{vG} (kPa^{-1})	0.009
n_{vG}	1.160

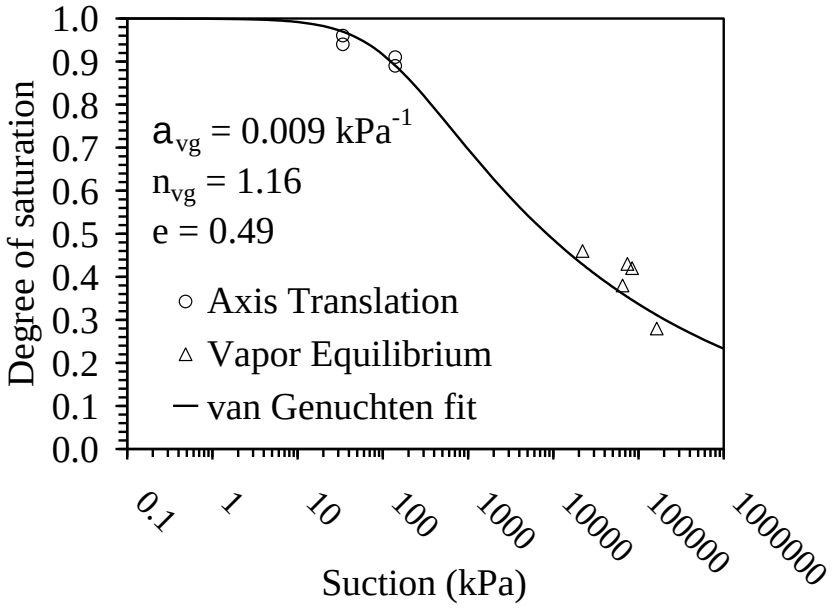

Figure 3.21: Experimental SWRC for Boulder clay with the fitted van Genuchten (1980) SWRC

Using the van Genuchten (1980) SWRC parameters α_{vG} and n_{vG} that were fitted to the experimental SWRC data, the hydraulic conductivity function (HCF) was estimated from the following equation:

$$k(\psi) = k_{sat}\left(\frac{(1-(\alpha_{vG}\psi)^{(n_{vG}-1)}(1+(\alpha_{vG}\psi)^{n_{vG}})^{-(1-\frac{1}{n_{vG}})})^2}{(1+(\alpha_{vG}\psi)^{n_{vG}})^{0.5(1-\frac{1}{n_{vG}})}}\right) \qquad 3.16$$

The HCF predicted using Equation 3.16, and using the saturated hydraulic conductivity from the flow pump tests is shown in Figure 3.23.

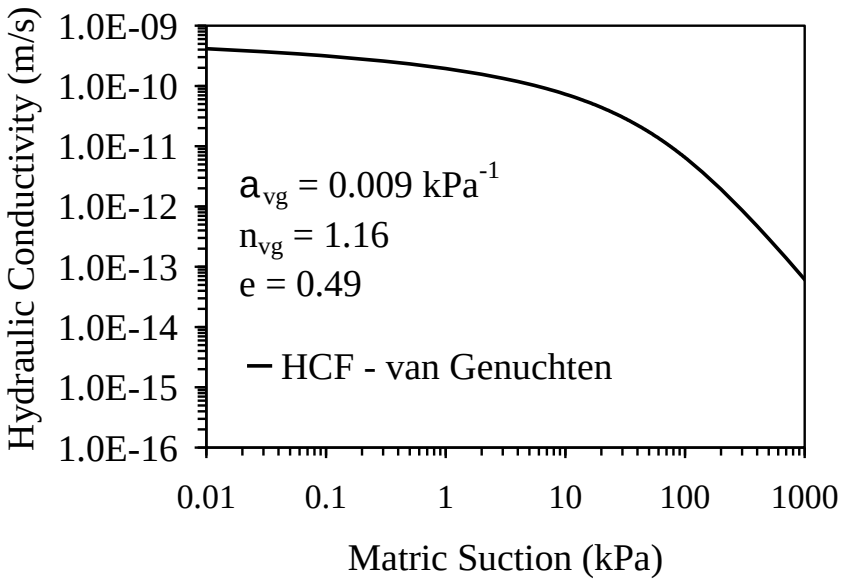

Figure 3.22: HCF predicted from the van Genuchten (1980) SWRC fitting parameters

4.0 Equipment and Procedures

This section details the equipment used during triaxial testing of Boulder clay and Mason sand. Two separate load frames were used to control the displacement rate applied to the triaxial specimens. For displacement rates up to 10 mm/min (strain rates ranging from 0.1 %/min to 14.5 %/min) a motor driven triaxial load frame manufactured was used to shear the specimens. This was the primary machine used to test all Boulder clay specimens and all dry Mason sand specimens. Vacuum and air pressure and water pressure was applied to the cell and specimens using a pressure panel purchased from Trautwein Soil Testing Equipment Co. The displacement during shear was monitored at the top of the triaxial cell using a linear variable differential transformer (LVDT). The axial load was measured using an 8.9 kN capacity load cell manufactured by GEOTAC mounted on the cross head of the load frame. The pore water pressure was measured from the bottom of the specimen with a 690 kPa capacity pressure transducer produced by GEOTAC.

During tests were the outflow of water from the specimen or changes in the cell volume needed to be monitored, a differential pressure transducer (DPT) attached to the back of the pressure panel was used. The data acquisition system used was a National Instruments SCXI-1000 chaise, SCXI-1520 module and SCXI-1314 terminal block for acquisition of load cell, pore pressure transducer and DPT signals and a SCXI-1540 module and SCXI-1315 terminal block for LVDT signals. A schematic of this experimental setup is shown in Figure 4.1.

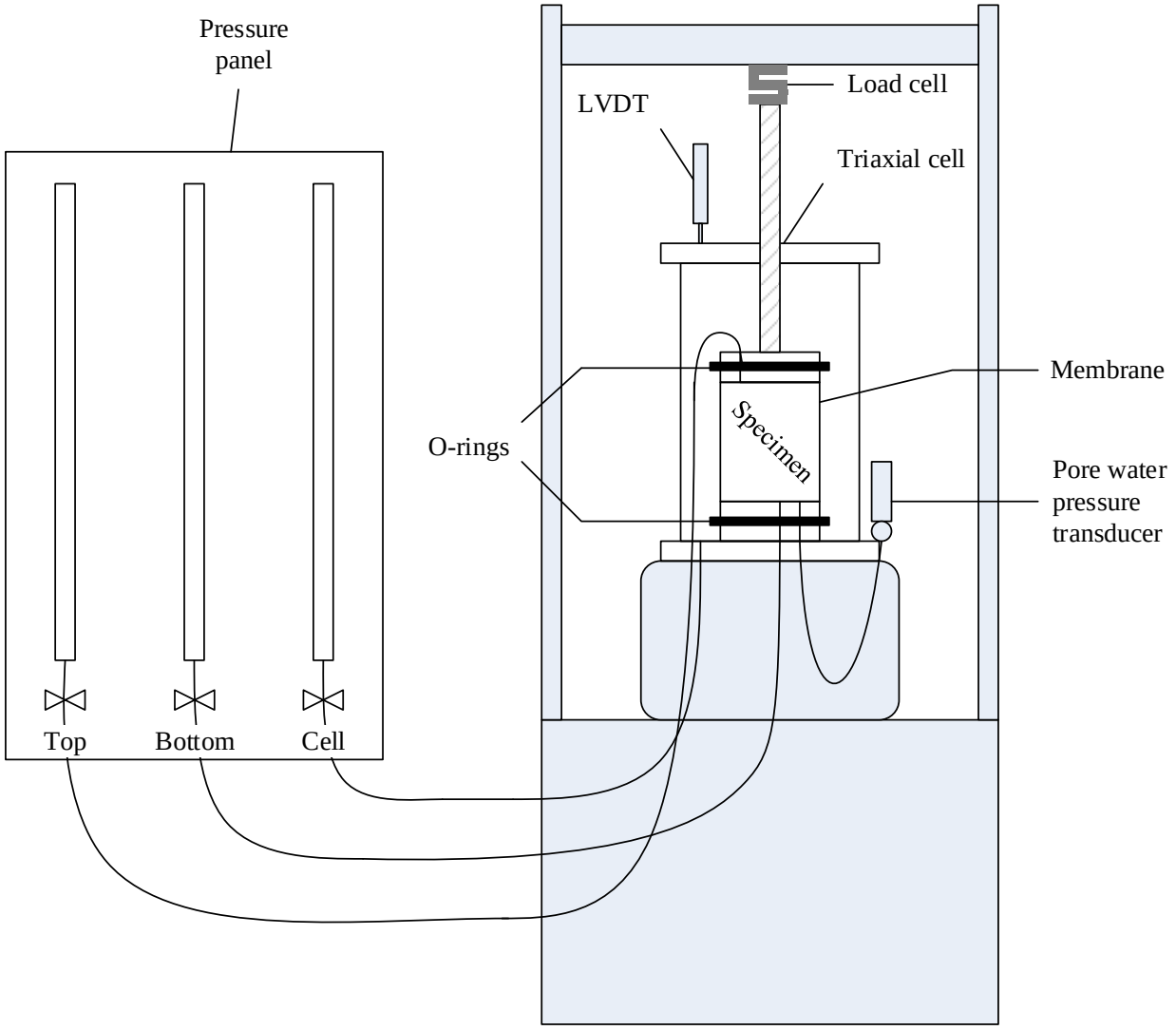

Figure 4.1: Schematic of pressure panel, load frame, and measuring devices used for triaxial testing at slower strain rates

For shearing displacement rates greater than 10 mm/min, a hydraulic press manufactured by MTS was used. The vacuum, air pressure and water pressure were applied with a Trautwein pressure panel. The displacement was measured with an internal LVDT integrated into the MTS machine. The axial load was measured with a 490 kN capacity load cell also manufactured by MTS. Pore water pressure was measured at the bottom of the specimen with a 2070 kPa pressure transducer manufactured by GEOTAC. National Instrument chaise, module and terminal block

were used for data acquisition and control of the MTS load frame. A picture of this experimental setup is shown in Figure 4.2.

Figure 4.2: Hydraulic MTS experimental setup

5.0 Strain Rate Effects on Mason Sand

This chapter presents the preparation of the triaxial specimens and results for tests performed on Mason sand. The first section discusses the preparation and results of test on saturated Mason sand specimens. The second section discusses the preparation and results of tests on dry Mason sand. The third section compares the results of saturated and dry Mason sand tests performed at axial strain rates of 0.75 %/min and1.56 %/min.

5.1 Saturated Mason Sand

5.1.1. Preparation and Shearing Procedures for Saturated Mason Sand Specimens

Four consolidated undrained triaxial tests were conducted at three different strain rates to investigate the effects of loading rate on the undrained shear strength of saturated Mason sand,. Each specimen was prepared by taking loose, oven-dry sand cooled to room temperature, and pouring it into a membrane stretched over a split mold having a diameter of 71 mm and height of 148 mm in three lifts of equal mass. Each lift was densified to a target void ratio of 0.54 using a mechanical eccentric weight vibrator. The target void ratio of 0.54 corresponds to a relative density of 0.89. The top cap was then placed on the specimen, the membrane was attached, and the specimen was placed under vacuum. After assembly of the cell, the sand was saturated by applying a vacuum to the top of the specimen and allowing water under atmospheric pressure to flow upward from the bottom.

Once water started to flow from the top of the specimen, the specimen was back-pressure saturated until the measured value of Skempton's B parameter reached 0.9 or remained constant with additional incremental increases to the backpressure. The final B-values and saturation details for each test are summarized in Table 5.1. The specimens were consolidated to 207 kPa and sheared to an axial strain of 15% in times of 20, 10, 1, and 0.1 minutes. The corresponding

strain rates to the before mentioned times to failure are 0.9, 1.5, 16, and 215 %/min respectively. The initial void ratio corresponding to the applied time to 15% axial strain, shearing rate and strain rate for each is given in Table 5.2.

Table 5.1: Summary of saturation details for test performed on Mason sand at different shearing rates

Time to 15% axial strain (min)	Shearing Rate (mm/min)	Strain Rate (%/min)	σ_{cell} (kPa)	σ_{back} (kPa)	B
20.0	1.2	0.9	483	276	0.80
10.0	2.5	1.5	483	276	0.93
1.0	28.0	16.0	483	276	0.90
0.1	367	215	483	276	0.89

Table 5.2: Initial void ratios after specimen preparation and void ratios after consolidation for tests on Mason sand

Time to 15% axial strain (min)	Shearing Rate (mm/min)	Strain Rate (%/min)	e_i	$\sigma_{confining}$ (kPa)	σ_3' (kPa)
20.0	1.2	0.9	0.54	483	207
10.0	2.5	1.5	0.55	483	207
1.0	28.0	16.0	0.53	483	207
0.1	360.0	211.0	0.54	483	207

During shearing, the axial displacement, axial load, and excess pore water pressure at the base of the specimen were recorded. This data was used to calculate the undrained shear strength (principal stress difference), principal stress ratio, and excess pore water pressure. The graphs of displacement versus time for the three tests are shown in Figure 5.1 and Figure 5.2.

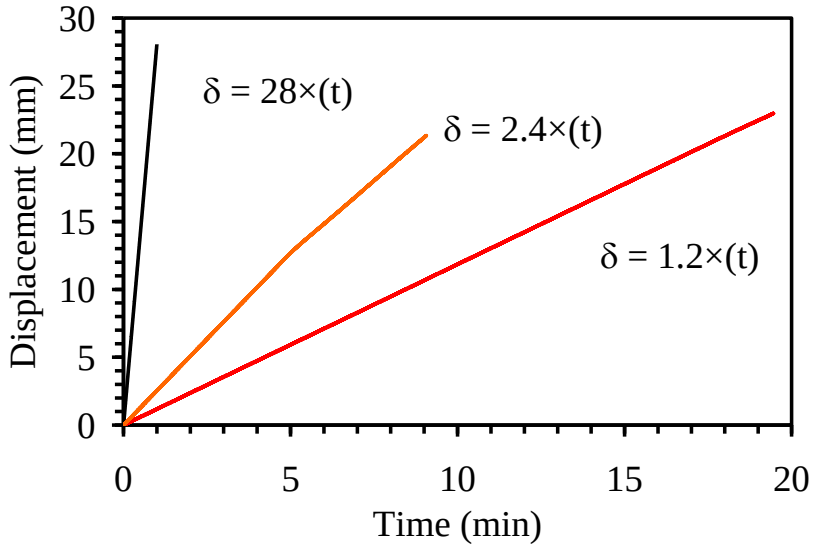

Figure 5.1: Recorded displacement versus time for specimens sheared to an axial strain of 15% in 1, 10, and 20 minutes

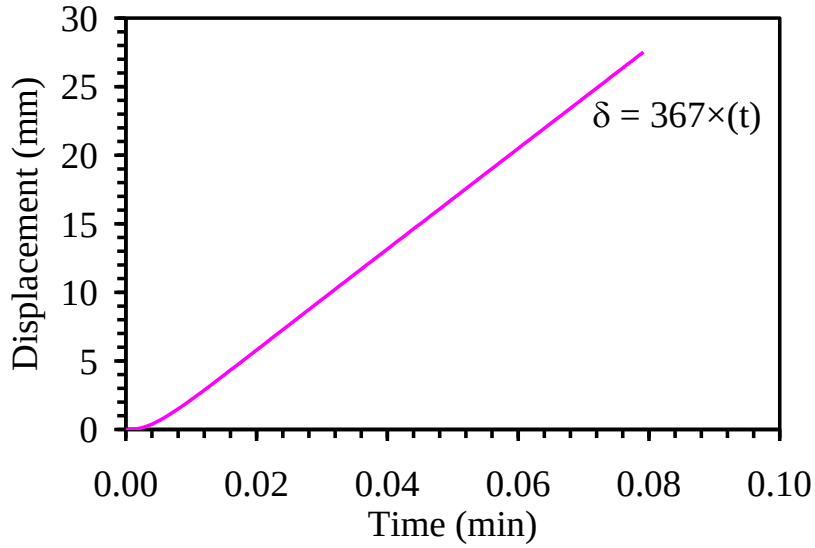

Figure 5.2: Recorded displacement versus time for specimens sheared to an axial strain of 15% in 0.1 minute

5.1.2 Results for Saturated Mason Sand

The shear strength, principal stress ratio and excess pore water pressure versus axial strain are shown in Figures 5.3 through 5.5. Principal stress difference versus axial strain shown in Figure 5.3 indicate a correlation between increasing time to 15% axial strain or strain rate and

increasing shear strength. The principal stress ratio shown in Figure 5.4 appears to be independent of the strain rate applied. The excess pore water pressure generated during shear is presented in Figure 5.5. For each test, the pore water pressure increases to approximately 100 kPa at 1% axial strain and then decreases at varying rates to about -300 kPa. In Figures 5.3 through 5.5 the SPT point of failure is identified with a hollow circle.

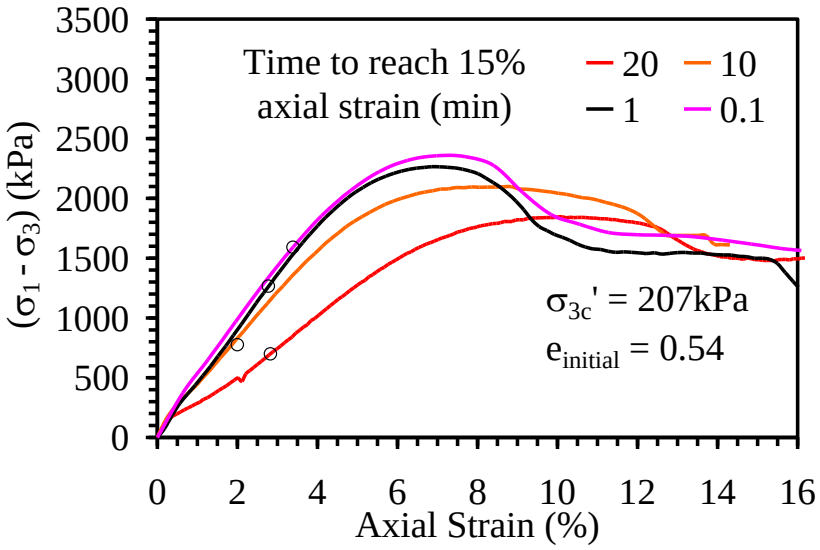

Figure 5.3: Principal stress difference with axial strain for triaxial compression tests on saturated Mason sand performed at different axial strain rates.

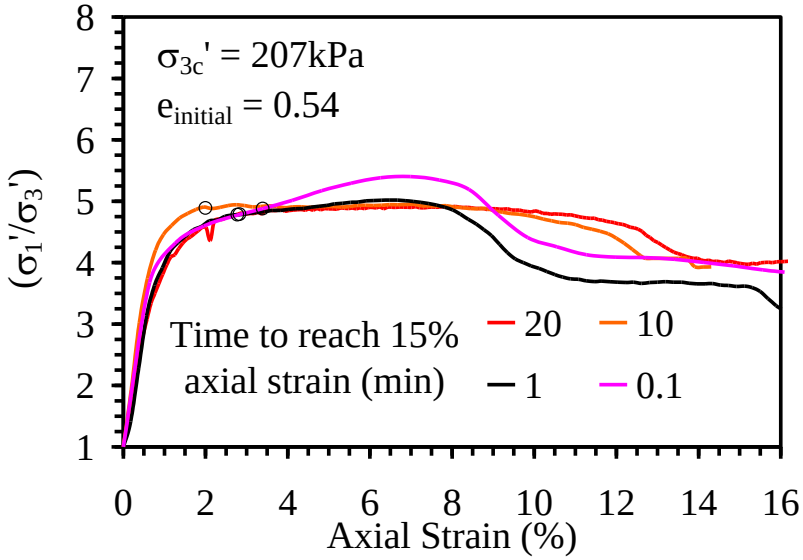

Figure 5.4: Principal stress ratio with axial strain for triaxial compression tests on saturated Mason sand performed at different axial strain rates.

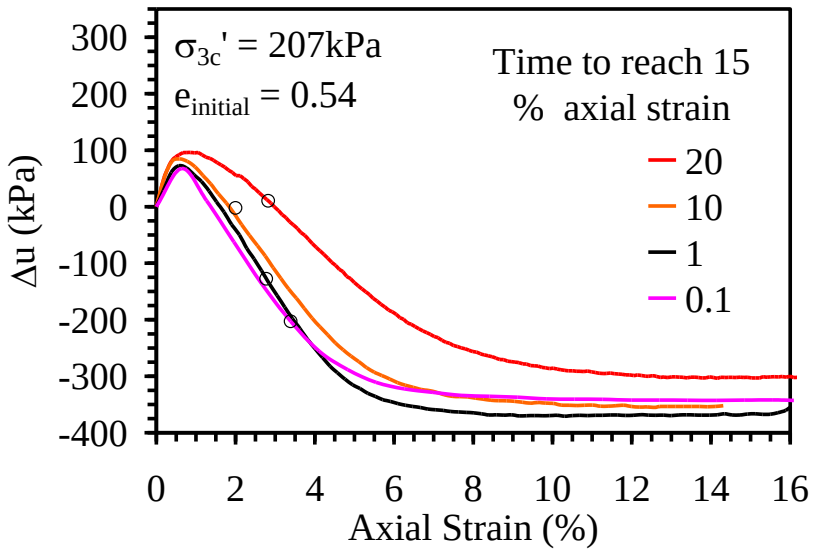

Figure 5.5: Excess pore water pressure with axial strain for triaxial compression tests on saturated Mason sand performed at different axial strain rates.

The stress paths for the four tests are plotted in modified Mohr-Coulomb stress space and are shown in 5.6. The failure envelope and failure points defined for stress path tangency criterion are shown in Figure 5.6(a) using hollow circles. The failure points defined using the maximum principal stress difference criterion are shown as hollow circles in Figure 5.6(b).

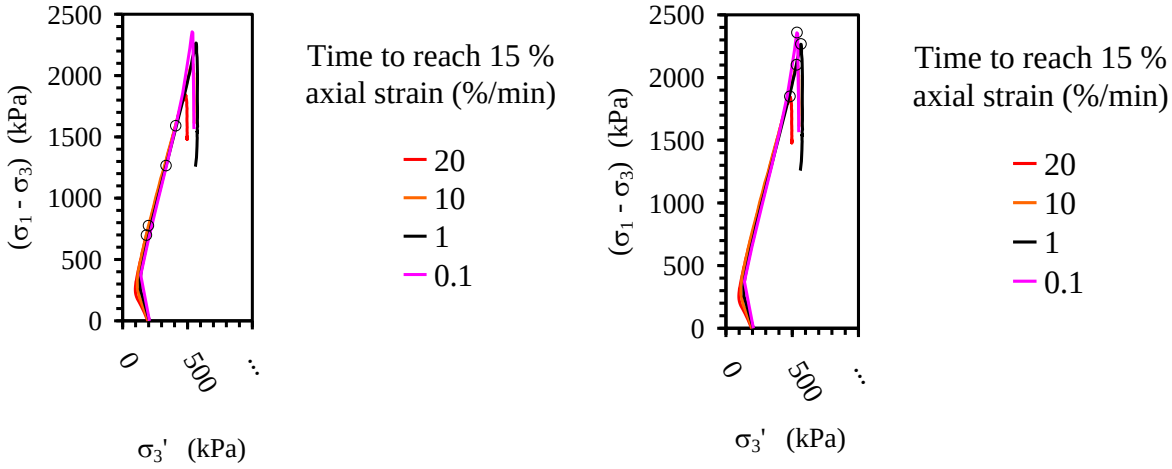

Figure 5.6: Stress paths in modified Mohr-Coulomb stress space for triaxial compression tests on Mason sand performed at different axial strain rates. Failure points using stress path tangency criterion are shown in Figure 5.6(a). Failure points using maximum principal stress difference criterion are shown in Figure 5.6(b).

5.2 Dry Mason Sand

5.2.1 Preparation and Shearing Procedures of Dry Mason Sand Specimens

To ensure that the rate effect on shear strength of Mason sand was due to the magnitude of excess pore water pressure during shearing, additional tests on Mason sand under dry conditions in consolidated drained triaxial compression were performed. These tests were conducted to verify that the mineralogy of the Mason sand (which may contain some silicate minerals), did not affect the shear strength or have some contribution to the rate effects. The procedures for preparation of dry sand specimens were identical to the saturated sand. Each specimen was densified using a mechanical vibrator to a target void ratio of 0.54 corresponding to a relative density of 0.89. Each specimen was placed under a vacuum of -80 kPa and the triaxial cell was assembled and filled with de-aired water. At this point, a cell pressure of 70 kPa was applied, the sample was released from the vacuum, and a pressure of 35 kPa was applied to the top and bottom of the sample. The cell pressure and pressure to the top and bottom was incrementally increased to 310 kPa cell pressure and 276 kPa top and bottom pressure. The specimen was then consolidated to 207 kPa and sheared under fully drained conditions by keeping the air lines to top and bottom specimen open. Strain rates of 0.75, 1.10, 1.56, and 3.1 %/min were used for the dry sand tests. These rates corresponding to times required to reach an axial strain of 15% axial strain of 20, 15, 10, and 5 minutes, respectively. The specimen volume change during shear was measured by tracking the change in outflow from the cell using a differential pressure transducer (DPT) connected to the back of the pressure panel. The displacement versus time results for the tests having different strain rates are shown in Figure 5.7. This plot clearly shows that the displacement rates were constant throughout the triaxial tests. The initial void ratio, confining pressure, and consolidation stress for each test are shown in Table 5.3.

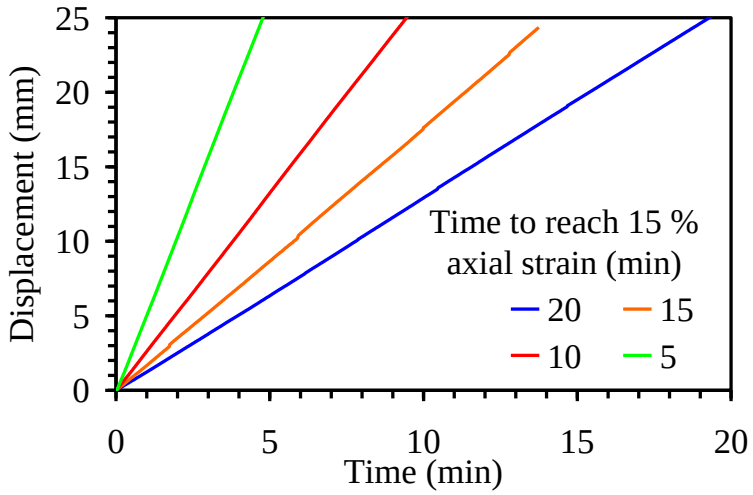

Figure 5.7: Recorded displacement versus time for specimens sheared to an axial strain of 15% in 5, 10, 15 and 20 minutes.

Table 5.3: Summary of testing details for triaxial compression tests on dry Mason sand.

Time to 15 % axial strain (min)	Strain Rate (%/min)	e_i	$\sigma_{confining}$ (kPa)	σ_3' (kPa)
20.0	0.8	0.54	483	207
1.0	1.1	0.53	483	207
0.1	1.6	0.54	483	207
0.01	3	0.53	483	207

5.2.2. Results for Dry Mason Sand

The principal stress difference versus axial strain curves for the four tests is shown in Figure 5.8. The principal stress ratio versus axial strain is shown in Figure 5.9. The stress-strain curves are relatively similar for the four tests regardless of the strain rate. Because the sand is dry (no excess pore water pressures), the stress-strain curves plotted in terms of principal stress difference and principal stress ratio have the same shape. Using stress path tangency (SPT) failure criterion, the maximum principal stress corresponds to the point of maximum friction mobilization in the dry sand (maximum principal stress ratio). The volumetric strain versus axial strain and volumetric strain with time results obtained from the outflow measurements for the

four tests are shown in Figure 5.10(a) and 5.10(b). All four specimens showed a small initial contraction, followed by dilation. To demonstrate accuracy and repeatability, at least two tests for each strain rate was performed.

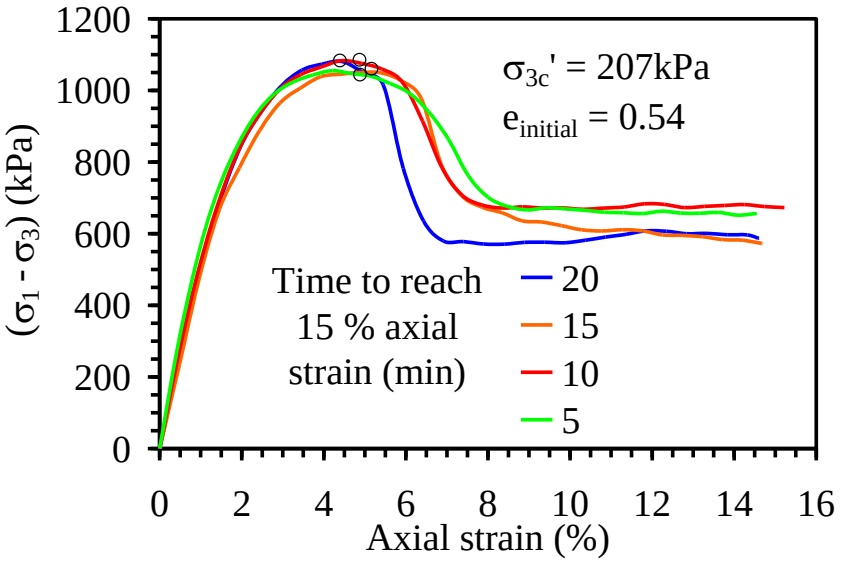

Figure 5.8: Principal stress difference with axial strain for triaxial compression tests on dry Mason sand performed at different axial strain rates.

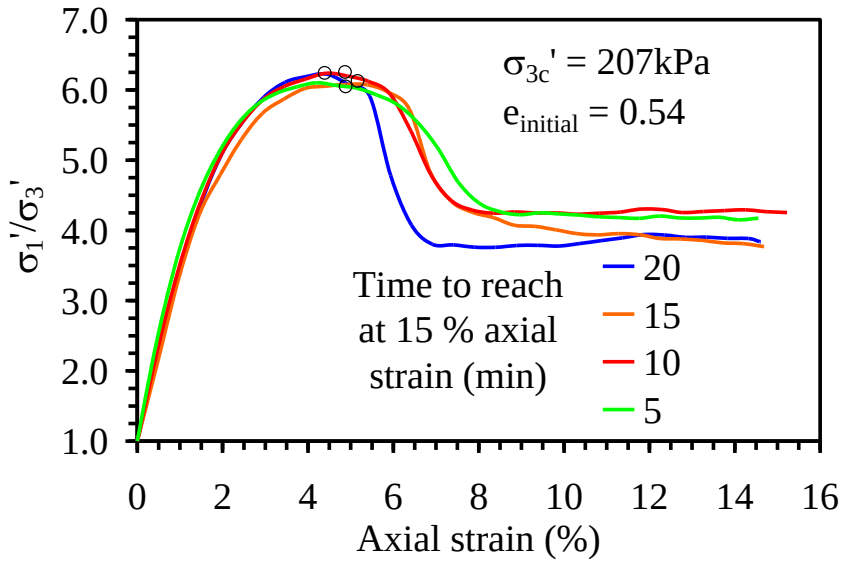

Figure 5.9: Principal stress ratio with axial strain for triaxial compression tests on dry Mason sand performed at different axial strain rates.

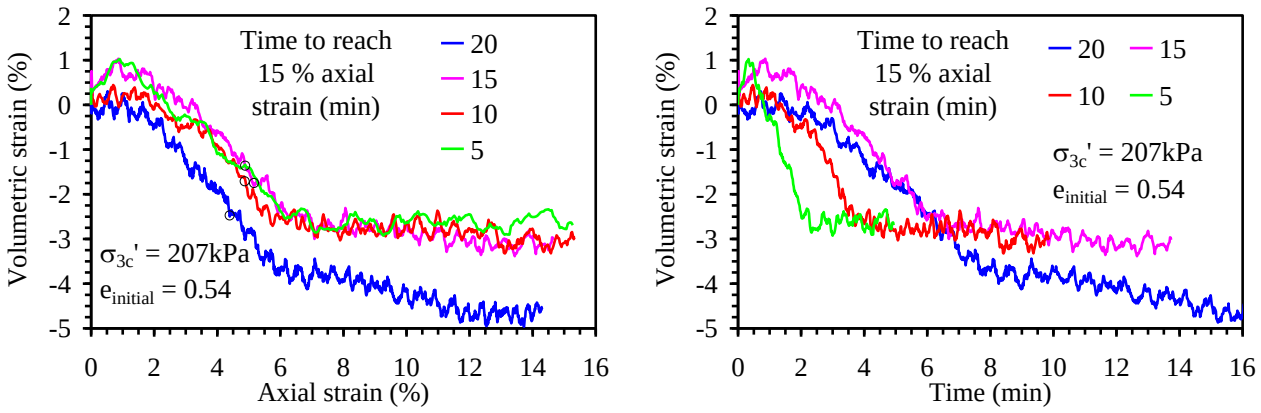

(a) (b)

Figure 5.10: Volumetric strain with axial strain (a) and volumetric strain with time (b) for triaxial compression tests on dry Mason sand performed at different axial strain rates

5.3 Comparison of Dry to Saturated Mason Sand Results

In this section, the results from the tests on the saturated Mason sand specimens are compared with those performed on the dry mason sand at the same strain rates. The comparisons were made for tests performed at the same axial strain rates of 0.75 and 1.56 %/minute corresponding times to 15% axial strain of 20 and 10 minutes. Comparison of the results from these tests can help assess whether the rate effects are due the impact of excess pore water pressure (and dilation during shearing) or mineralogy.

5.3.1. Comparison between Dry and Saturated Mason Sand Tests Performed at 0.75 %/min Axial Strain Rate

The results for triaxial compression tests performed at an axial strain rate of 0.75 %/min corresponding to a time to 15% axial strain of 20 minutes conducted under drained, dry conditions and saturated, undrained conditions are shown Figures 5.11 through 5.13. The displacement versus time for the two tests is shown in Figure 5.11. The principal stress difference versus axial strain for the four tests is shown in Figure 5.12. The principal stress ratio

versus axial strain is shown in Figure 5.13. In Figures 5.12 and 5.13 the SPT failure points are identified with a hollow square.

From the results shown in Figure 5.12, it is clear that the saturated sand tests reach a much higher maximum principal stress difference than the dry sand tests due to effects of the negative excess pore water pressures. However, the SPT failure point corresponding to the shear strength at failure is greater for the dry sand than for the saturated sand. Evaluation of the results in Figure 5.13 indicates that the dry sand has a larger maximum principal stress ratio than the saturated sand.

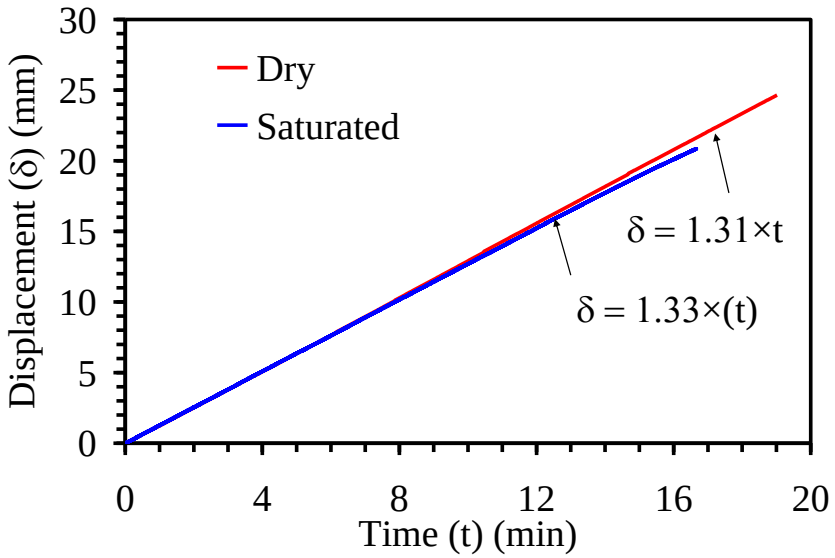

Figure 5.11: Recorded displacement versus time for dry and saturated Mason sand specimens performed at an axial strain rate of 0.75 %/min.

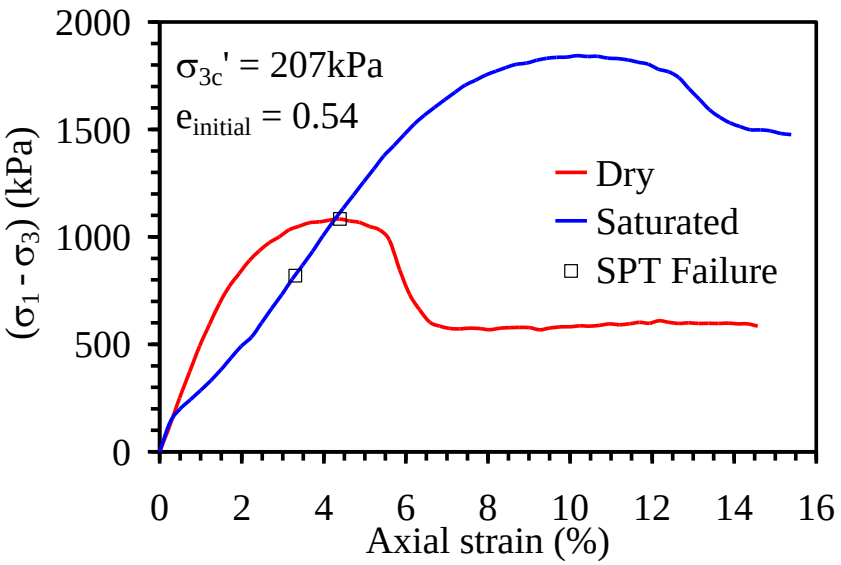

Figure 5.12: Principal stress difference with axial strain for triaxial compression tests on dry and saturated Mason sand performed at an axial strain rate of 0.75 %/min.

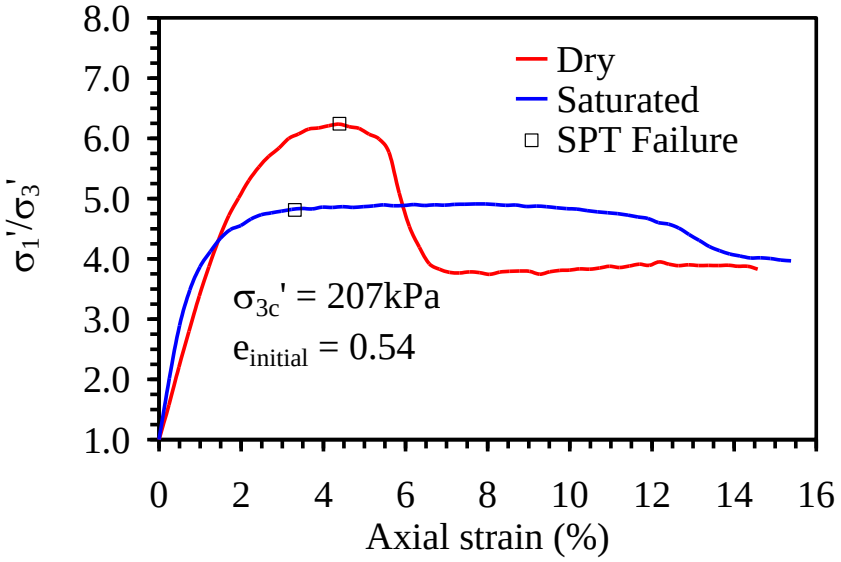

Figure 5.13: Principal stress ratio with axial strain for triaxial compression tests on dry and saturated Mason sand performed at an axial strain rate of 0.75 %/min.

5.3.2. Comparison between Dry and Saturated Mason Sand Triaxial Compression Tests Performed at an Axial strain rate of 1.56 %/min

The results for triaxial compression tests conducted under drained, dry conditions and saturated, undrained conditions at an axial strain rate of 1.56 %/min corresponding to a time to

15% axial strain of 10 minutes are shown Figures 5.14 through 5.16. The displacement versus time curves for the two tests are shown in Figure 5.14. The principal stress difference versus axial strain for the four tests is shown in Figure 5.15. The principal stress ratio versus axial strain is shown in Figure 5.16.

From Figure 5.15, the saturated sand test clearly reaches a much higher maximum principal stress difference than the dry sand test. From Figure 5.16, the dry sand test has a larger maximum principal stress ratio than the saturated test. These observations are identical to those made for the tests performed at an axial strain rate of 0.75 %/min. However, unlike the 0.75 %/min tests, the shear strength using SPT criterion of the saturated sand indicated by hollow squares in Figure 5.15 is nearly equal to the shear strength of the dry sand.

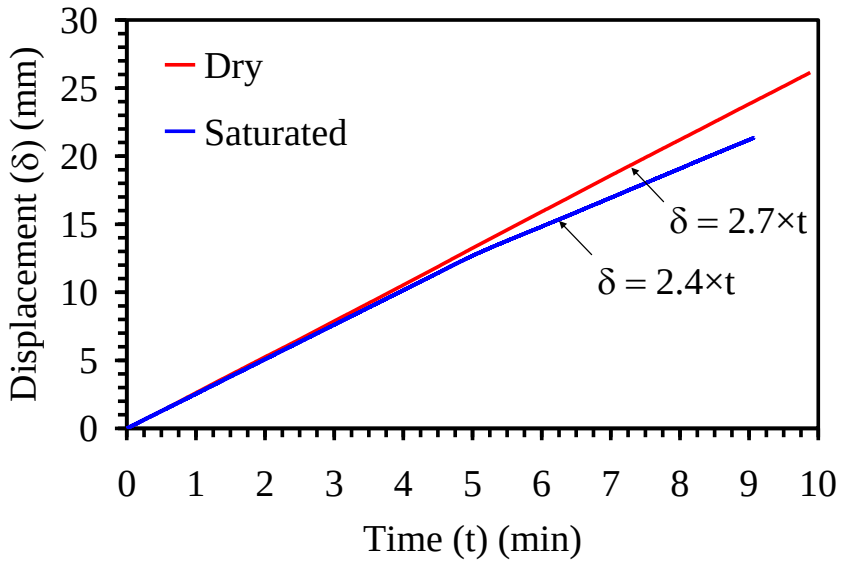

Figure 5.14: Recorded displacement versus time for dry and saturated Mason sand specimens performed at an axial strain rate of 1.56 %/min.

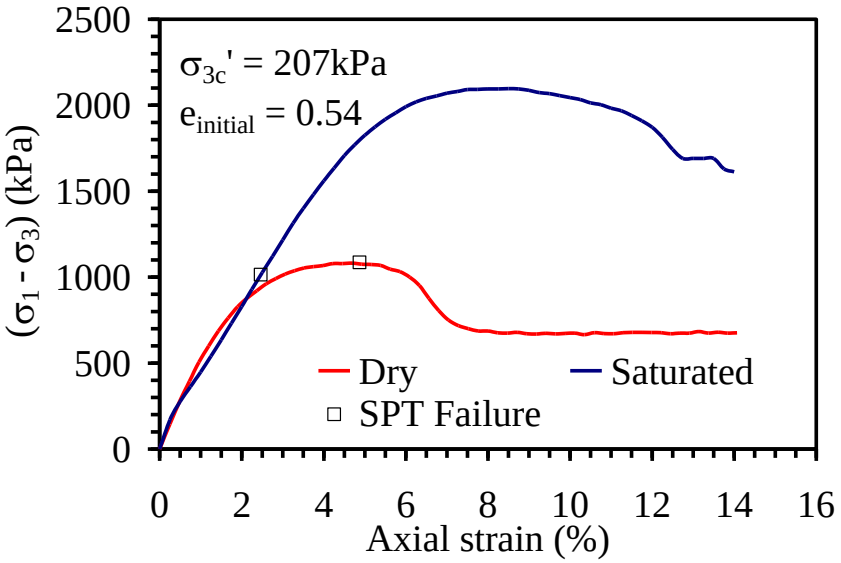

Figure 5.15: Principal stress difference with axial strain for triaxial compression tests on dry and saturated Mason sand performed at an axial strain rate of 1.56 %/min.

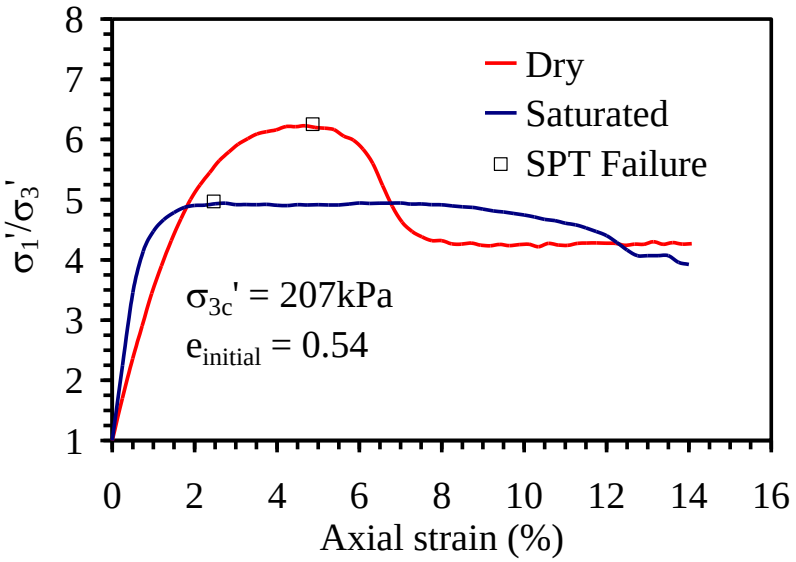

Figure 5.16: Principal stress ratio with axial strain for triaxial compression tests on dry and saturated Mason sand performed at an axial strain rate of 1.56 %/min.

5.4 Repeatability of Mason Sand Tests

To prove repeatability of triaxial compression tests on Mason sand, all tests with the exception of the saturated test run at a time to 15% axial strain in 10 minutes were performed a minimum of two times. The first section provides the principal stress difference, principal stress

ratio and excess pore water pressure with axial strain for all saturated tests performed. The second section shows the principal stress difference, principal stress ratio and volumetric strain with axial strain for all dry Mason sand tests performed.

5.4.1 Repeatability of Saturated Mason Sand Tests

Figures 5.17 through 5.23 shows the axial displacement with time of testing, principal stress difference, average principal stress difference and error bars, principal stress ratio, average principal stress ratio and error bars, excess pore water pressure, and average excess pore water pressure and error bars with axial strain for all Mason sand tests performed at a time to 15% axial strain of 20 minutes. Figures 5.24 through 5.30 shows axial displacement with time of testing, principal stress difference, average principal stress difference and error bars, principal stress ratio, average principal stress ratio and error bars, excess pore water pressure, and average excess pore water pressure and error bars with axial strain for all Mason sand tests performed at a time to 15% axial strain of 1 minute. Figures 5.31 through 5.37 shows axial displacement with time of testing, principal stress difference, average principal stress difference and error bars, principal stress ratio, average principal stress ratio and error bars, excess pore water pressure, and average excess pore water pressure and error bars with axial strain for all Mason sand tests performed at a time to 15% axial strain of 0.1 minute.

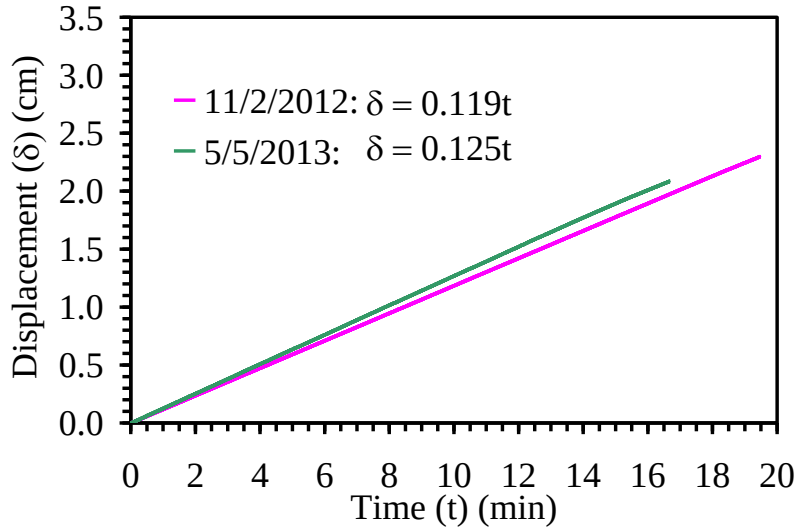

Figure 5.17: Axial displacement with time of testing of triaxial compression tests on saturated Mason sand performed at a time to 15% axial stain of 20 minutes

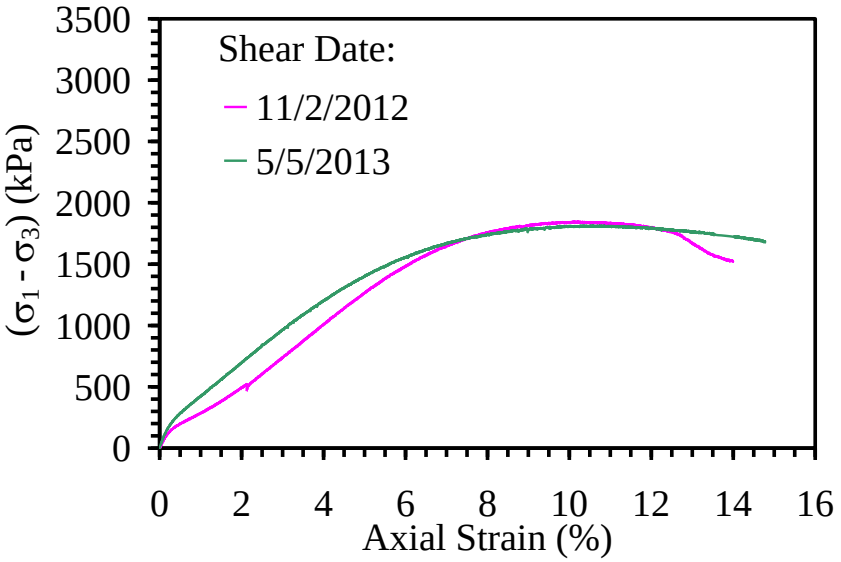

Figure 5.18: Principal stress difference with axial strain of triaxial compression test on saturated Mason sand performed at a time to 15% axial strain of 20 minutes

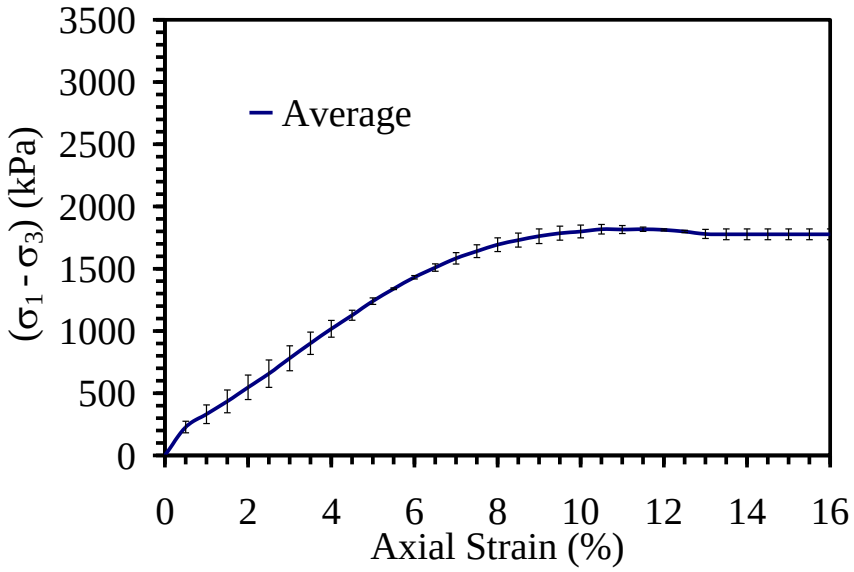

Figure 5.19: Average principal stress difference and error bars with axial strain of triaxial compression test on all saturated Mason sand performed at a time to 15% axial strain of 20 minutes

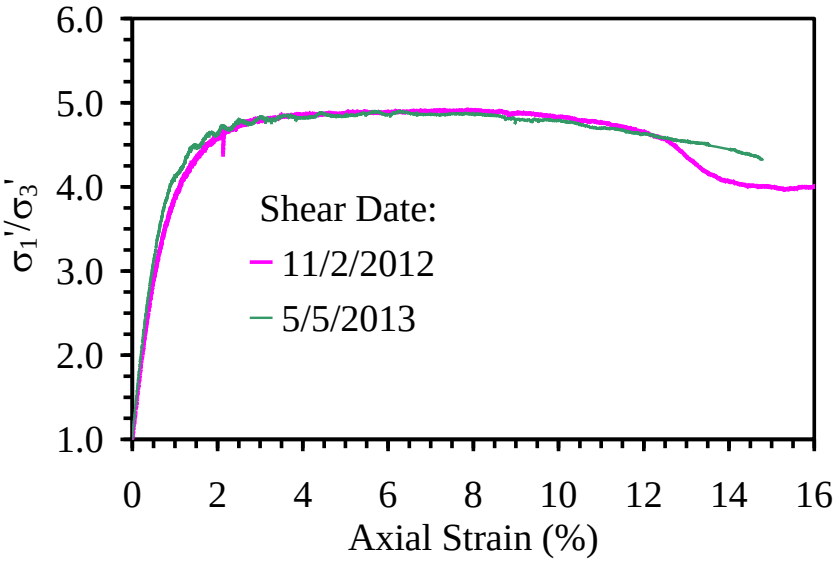

Figure 5.20: Principal stress ratio with axial strain of triaxial compression test on saturated Mason sand performed at a time to 15% axial strain of 20 minutes

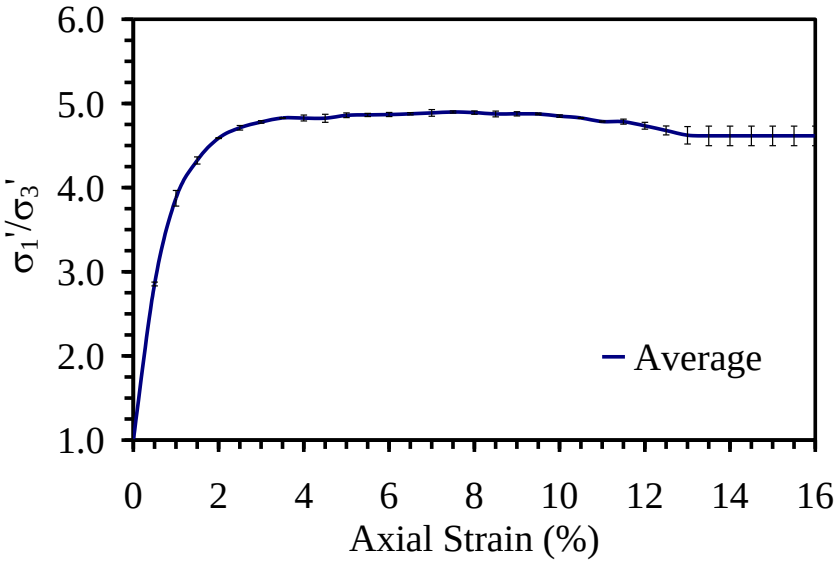

Figure 5.21: Average principal stress ratio and error bars with axial strain of triaxial compression test on all saturated Mason sand performed at a time to 15% axial strain of 20 minutes

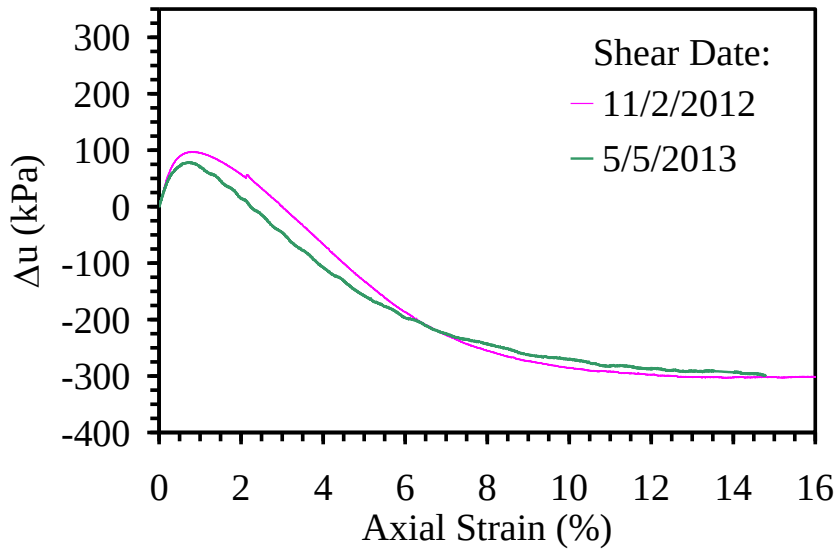

Figure 5.22: Excess pore water pressure with axial strain of triaxial compression test on saturated Mason sand performed at a time to 15% axial strain of 20 minutes

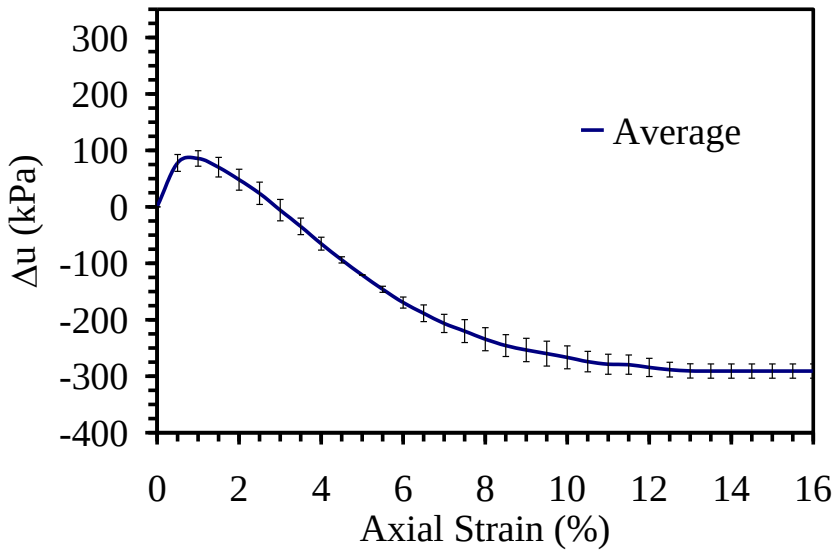

Figure 5.23: Average excess pore water pressure and error bars with axial strain of triaxial compression test on all saturated Mason sand performed at a time to 15% axial strain of 20 minutes

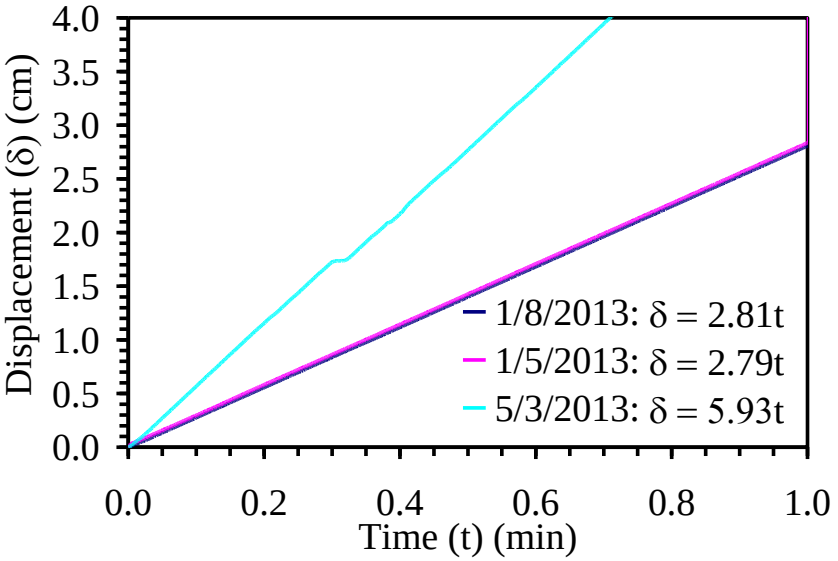

Figure 5.24: Axial displacement with time of testing of triaxial compression tests on saturated Mason sand performed at a time to 15% axial strain of 1 minute

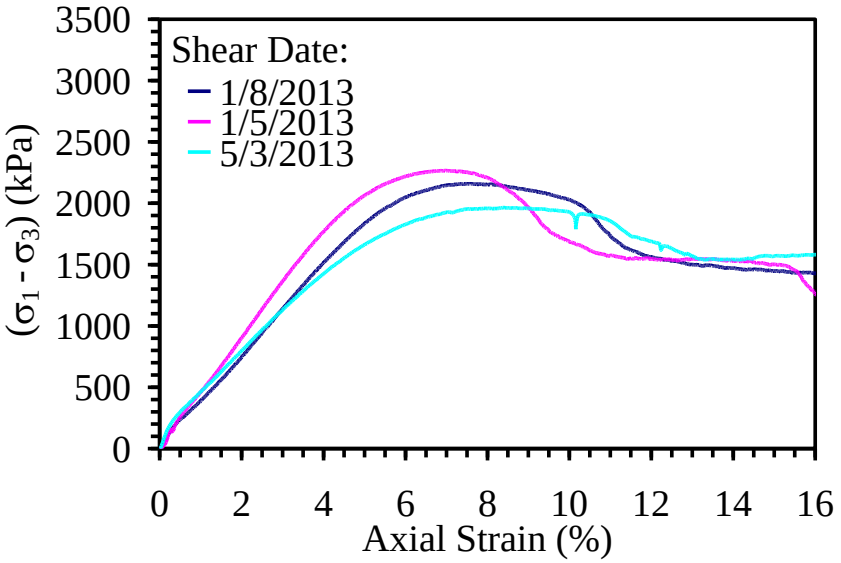

Figure 5.25: Principal stress difference with axial strain of triaxial compression test on saturated Mason sand performed at a time to 15% axial strain of 1 minute

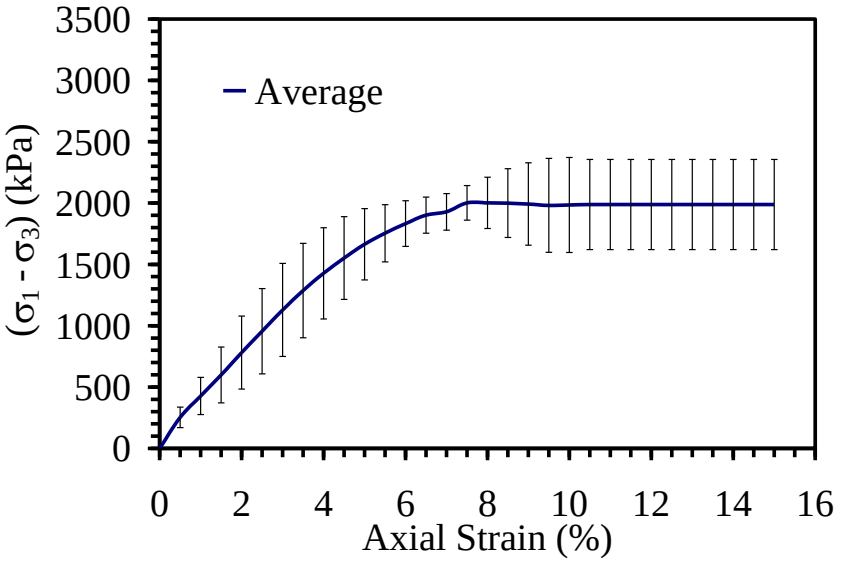

Figure 5.26: Average principal stress difference and and error bars with axial strain of triaxial compression test on all saturated Mason sand performed at a time to 15% axial strain of 1 minute

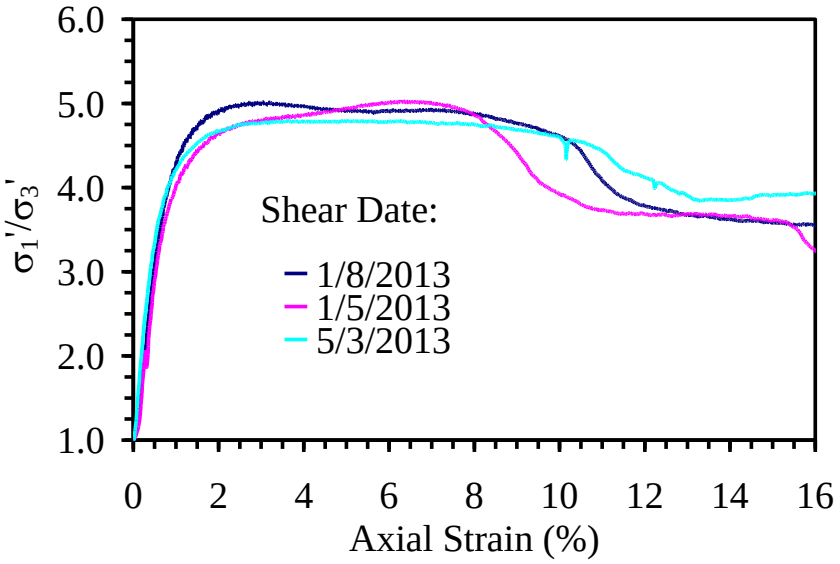

Figure 5.27: Principal stress ratio with axial strain of triaxial compression test on saturated Mason sand performed at a time to 15% axial strain of 1 minute

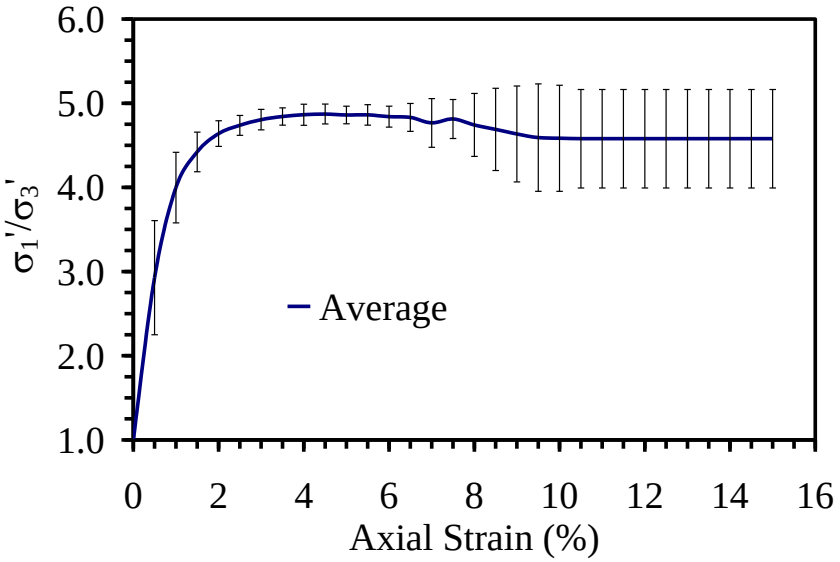

Figure 5.28: Average principal stress ratio and error bars with axial strain of triaxial compression test on all saturated Mason sand performed at a time to 15% axial strain of 1 minute

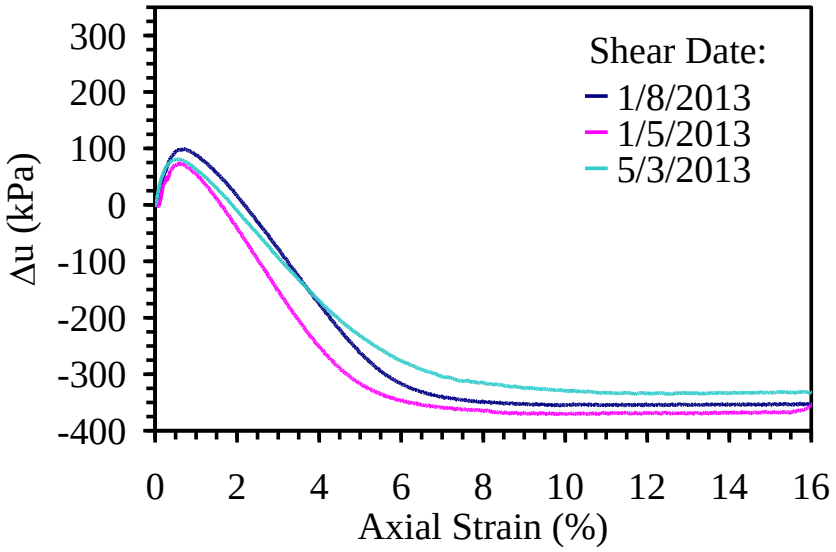

Figure 5.29: Excess pore water pressure with axial strain of triaxial compression test on saturated Mason sand performed at a time to 15% axial strain of 1 minute

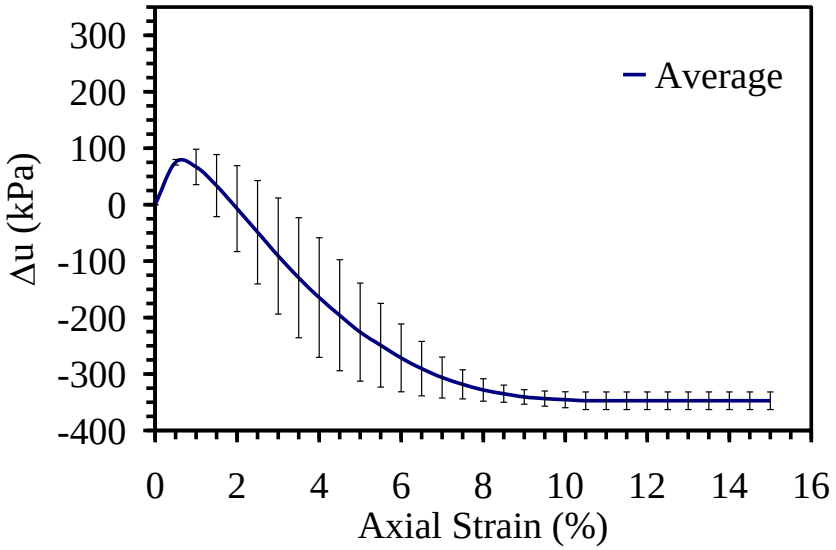

Figure 5.30: Average excess pore water pressure and error bars with axial strain of triaxial compression test on all saturated Mason sand performed at a time to 15% axial strain of 1 minute

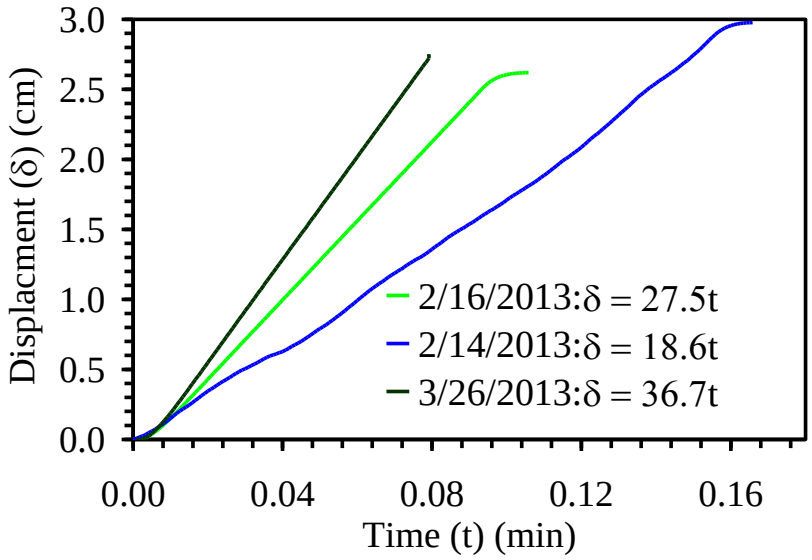

Figure 5.31: Axial displacement with time of testing of triaxial compression tests on all saturated Mason sand performed at a time to 15% axial strain of 0.1 minute

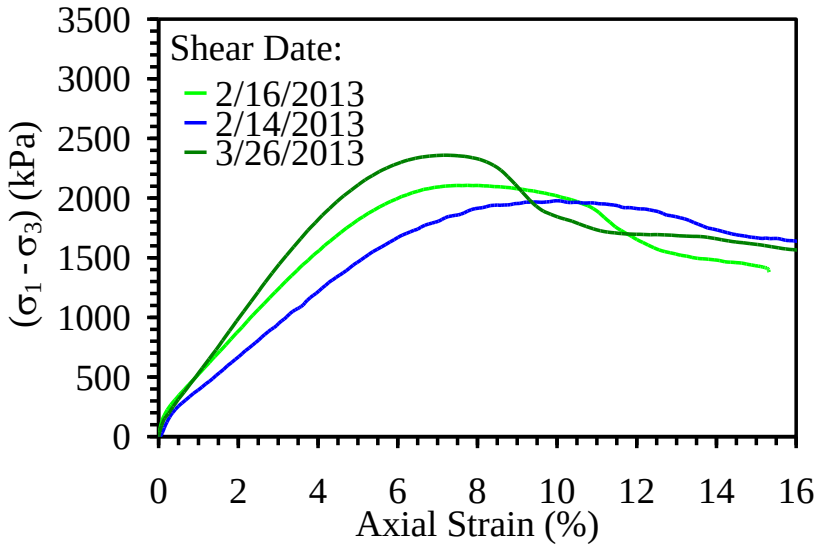

Figure 5.32: Principal stress difference with axial strain of triaxial compression test on saturated Mason sand performed at a time to 15% axial strain of 0.1 minute

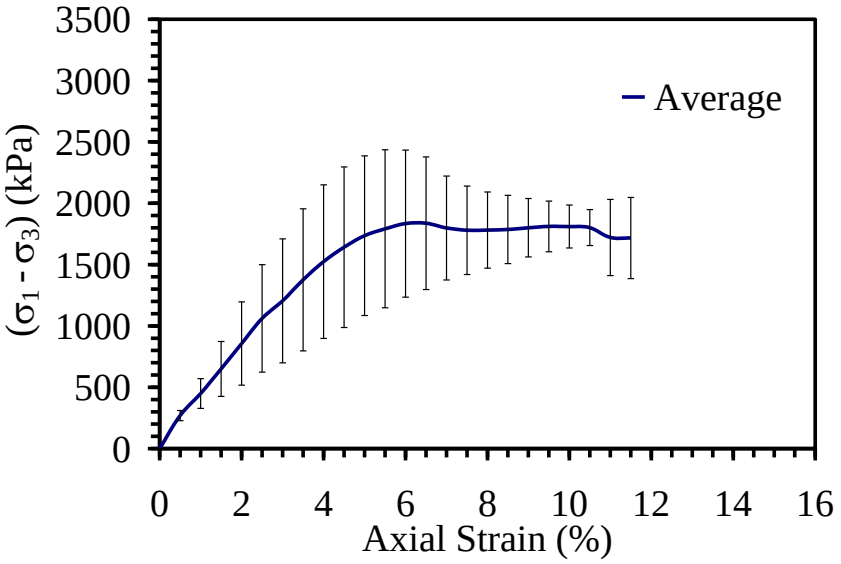

Figure 5.33: Average principal stress difference and error bars with axial strain of triaxial compression test on all saturated Mason sand performed at a time to 15% axial strain of 0.1 minute

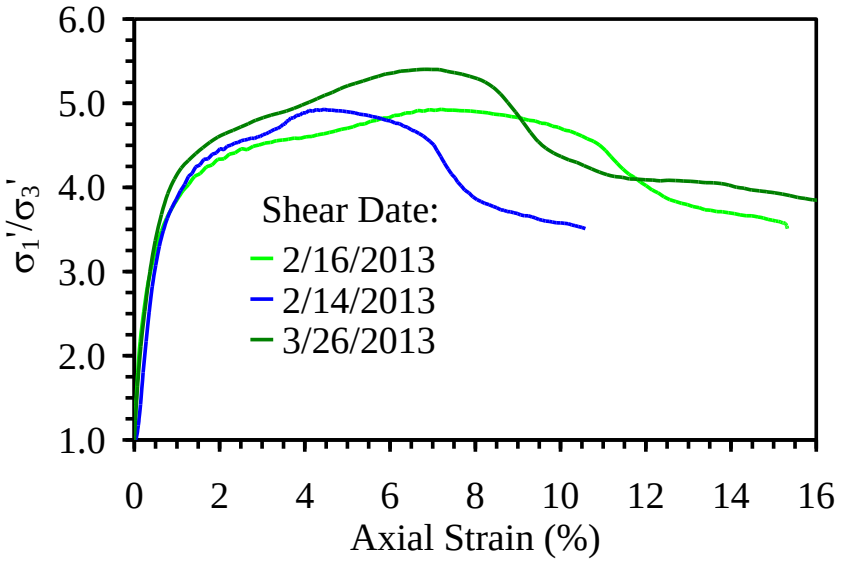

Figure 5.34: Principal stress ratio with axial strain of triaxial compression test on saturated Mason sand performed at a time to 15% axial strain of 0.1 minute

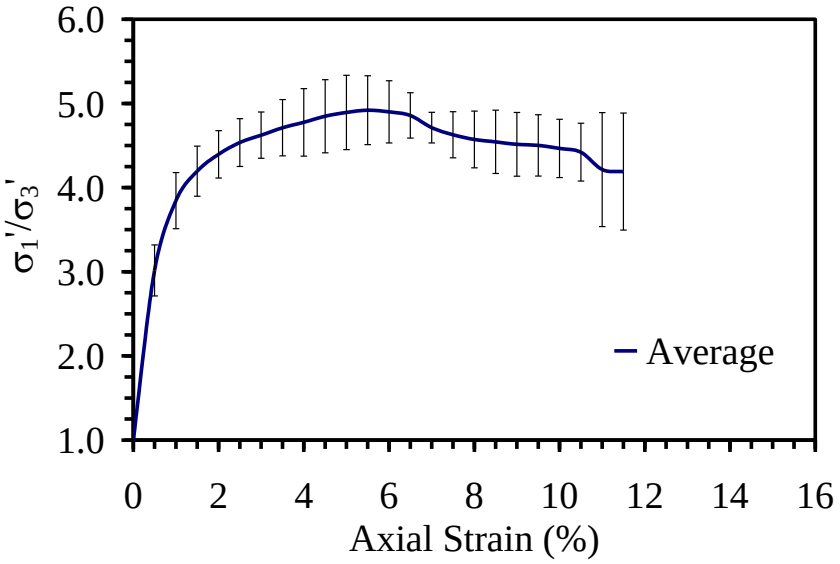

Figure 5.35: Average principal stress ratio and error bars with axial strain of triaxial compression test on all saturated Mason sand performed at a time to 15% axial strain of 0.1 minute

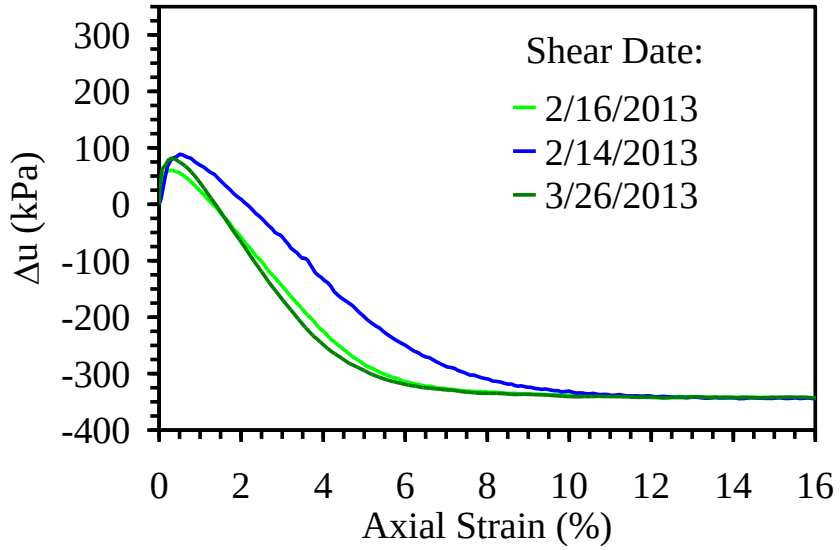

Figure 5.36: Excess pore water pressure with axial strain of triaxial compression test on saturated Mason sand performed at a time to 15% axial strain of 0.1 minute

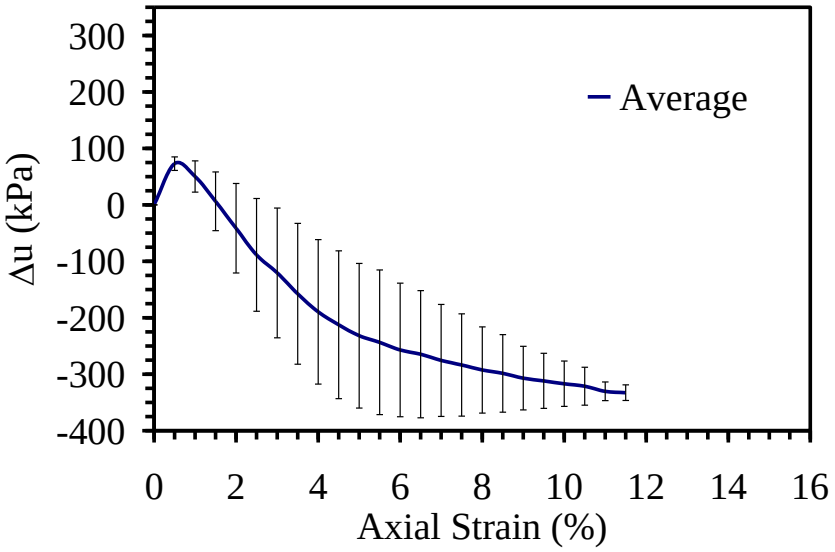

Figure 5.37: Average excess pore water pressure and error bars with axial strain of triaxial compression test on all saturated Mason sand performed at a time to 15% axial strain of 0.1 minute

5.4.2 Repeatability of Dry Mason Sand Tests

Figures 5.38 through 5.44 show the axial displacement with time of testing, principal stress difference, average principal stress difference and error bars, principal stress ratio, average principal stress ratio and error bars, volumetric strain, and average volumetric strain and error bars with axial strain for all dry Mason sand tests performed at a time to 15% axial strain of 20 minutes. Figures 5.45 through 5.51 show the axial displacement with time of testing, principal stress difference, average principal stress difference and error bars, principal stress ratio, average principal stress ratio and error bars, volumetric strain, and average volumetric strain and error bars with axial strain for all dry Mason sand tests performed at a time to 15% axial strain of 15 minutes. Figures 5.52 through 5.58 show the axial displacement with time of testing, principal stress difference, average principal stress difference and error bars, principal stress ratio, average principal stress ratio and error bars, volumetric strain, and average volumetric strain and error bars with axial strain for all dry Mason sand tests performed at a time to 15% axial strain of 10

minutes. Figures 5.59 through 5.65 show the axial displacement with time of testing, principal stress difference, average principal stress difference and error bars, principal stress ratio, average principal stress ratio and error bars, volumetric strain, and average volumetric strain and error bars with axial strain for all dry Mason sand tests performed at a time to 15% axial strain of 5 minutes.

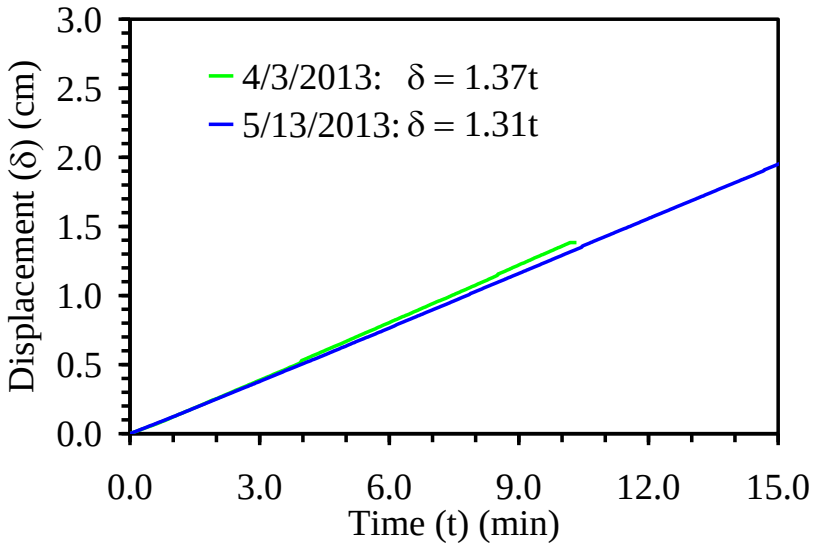

Figure 5.38: Axial displacement with time of testing of triaxial compression tests on dry Mason sand performed at a time to 15% axial strain of 20 minutes

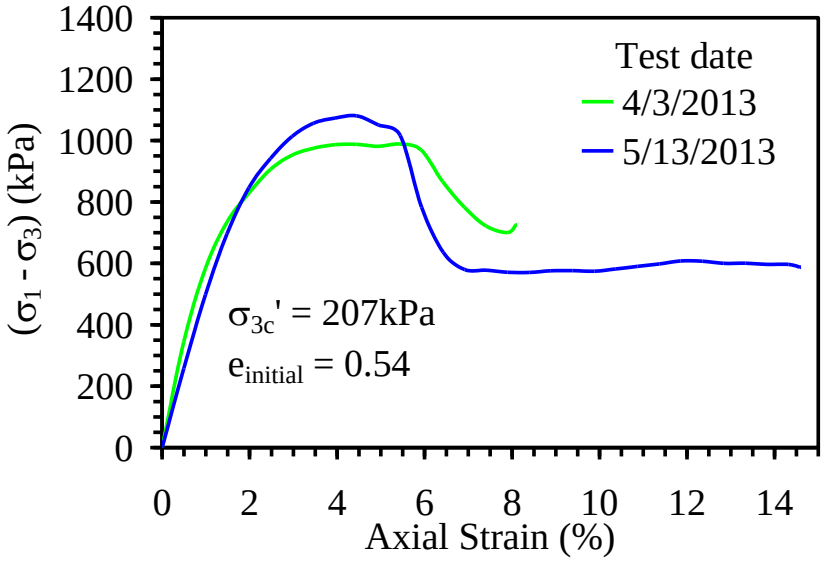

Figure 5.39: Principal stress difference with axial strain of triaxial compression test on dry Mason sand performed at a time to 15% axial strain of 20 minutes

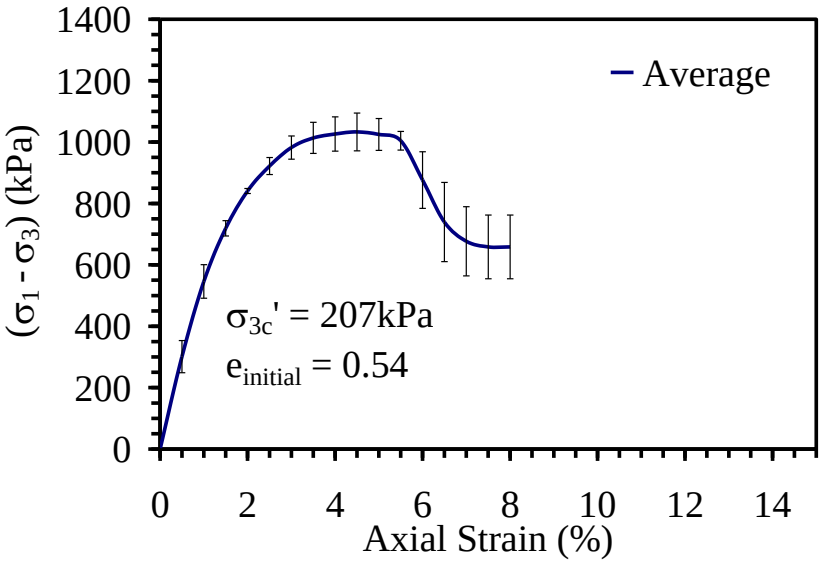

Figure 5.40: Average principal stress difference and error bars with axial strain of triaxial compression test on all dry Mason sand performed at a time to 15% axial strain of 20 minutes

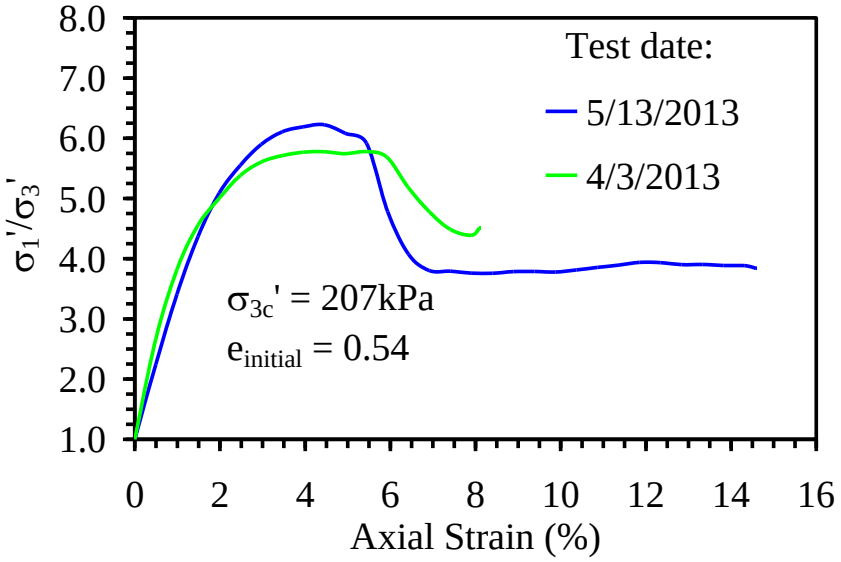

Figure 5.41: Principal stress ratio with axial strain of triaxial compression test on dry Mason sand performed at a time to 15% axial strain of 20 minutes

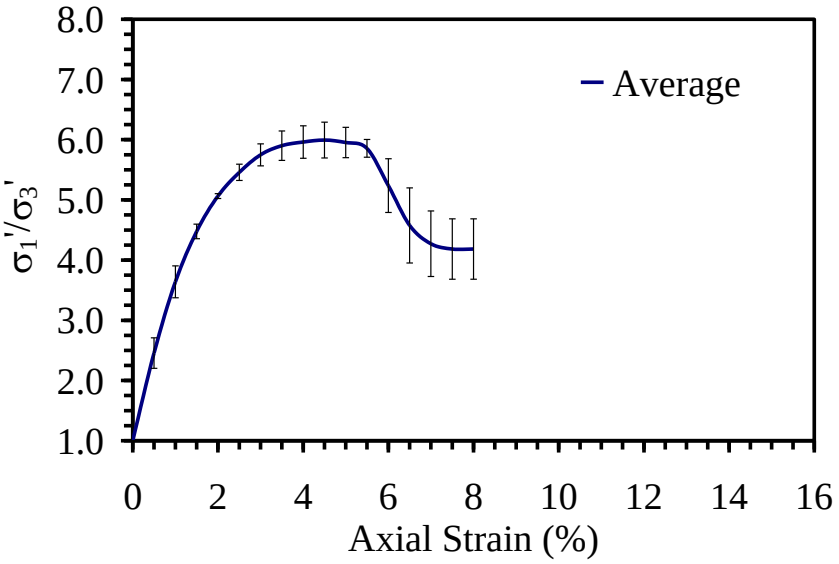

Figure 5.42: Average principal stress ratio and error bars with axial strain of triaxial compression test on all dry Mason sand performed at a time to 15% axial strain of 20 minutes

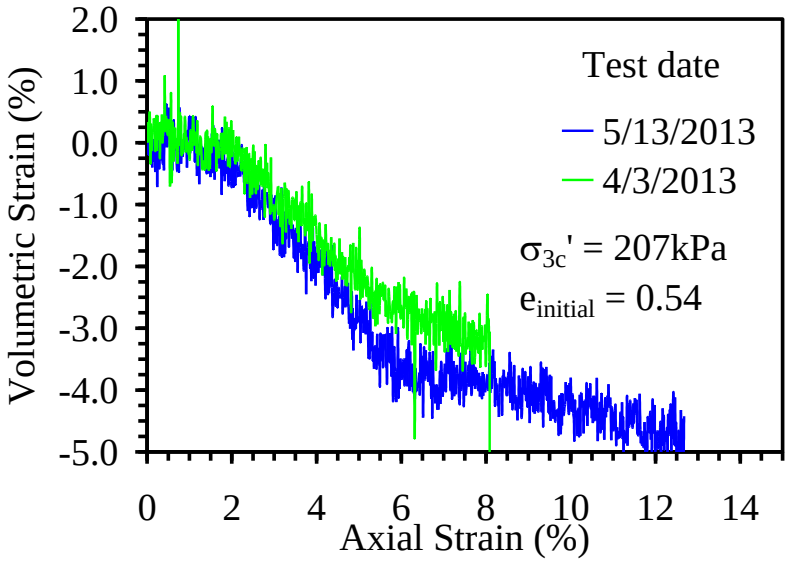

Figure 5.43: Volumetric strain with axial strain of triaxial compression test on dry Mason sand performed at a time to 15% axial strain of 20 minutes

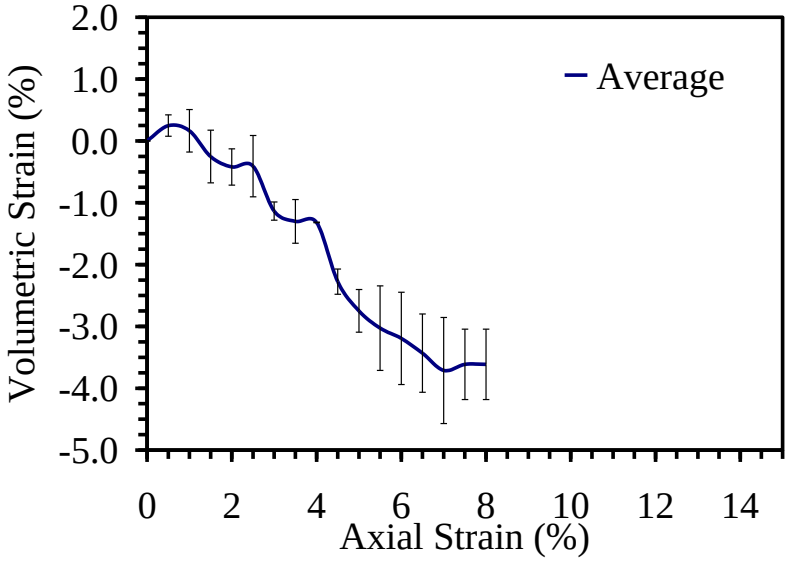

Figure 5.44: Average volumetric strain and error bars with axial strain of triaxial compression test on all dry Mason sand performed at a time to 15% axial strain of 20 minutes

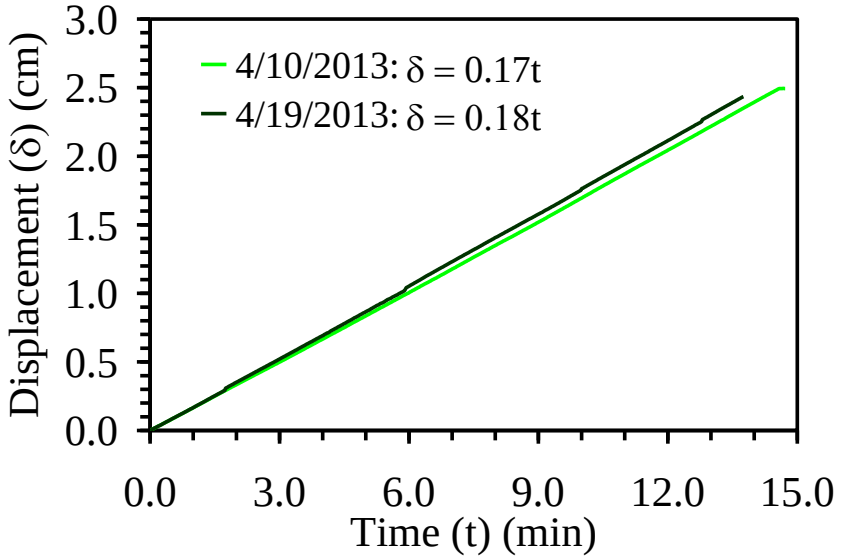

Figure 5.45: Axial displacement with time of testing of triaxial compression tests on dry Mason sand performed at a time to 15% axial strain of 15 minutes

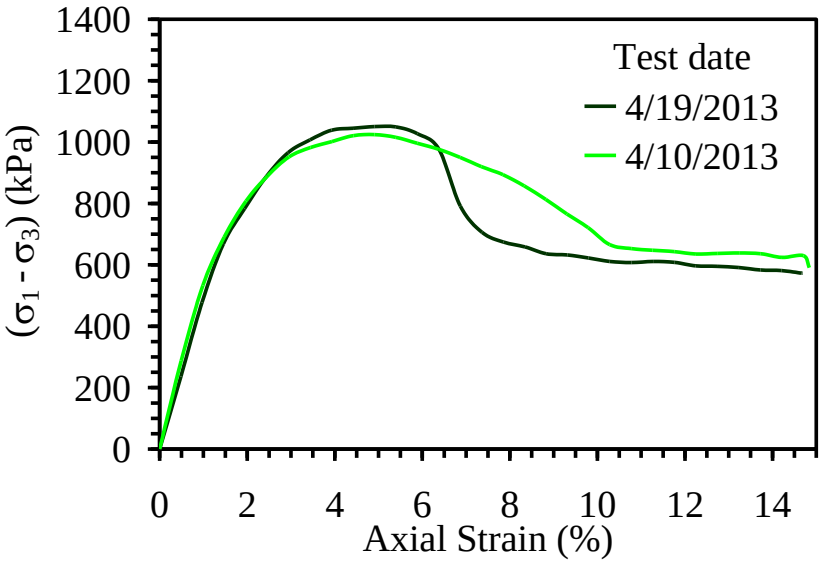

Figure 5.46: Principal stress difference with axial strain of triaxial compression test on dry Mason sand performed at a time to 15% axial strain of 15 minutes

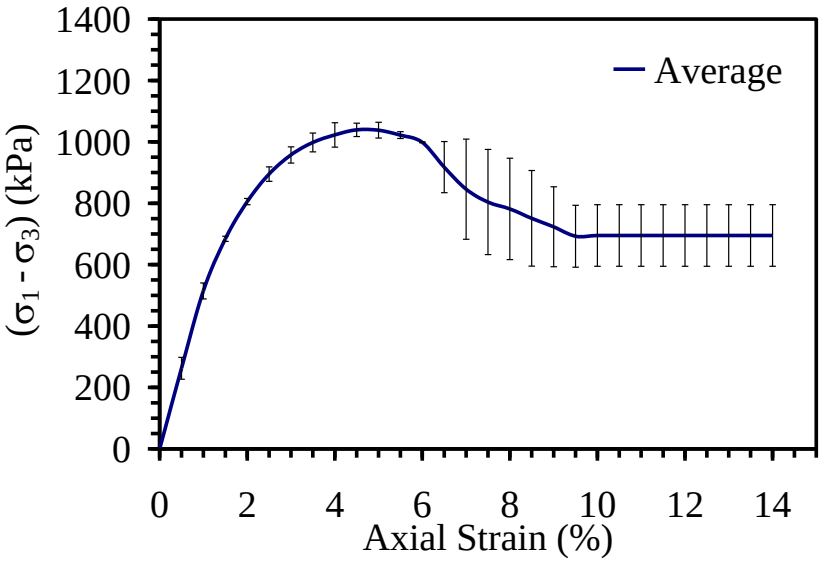

Figure 5.47: Average principal stress difference and error bars with axial strain of triaxial compression test on all dry Mason sand performed at a time to 15% axial strain of 15 minutes

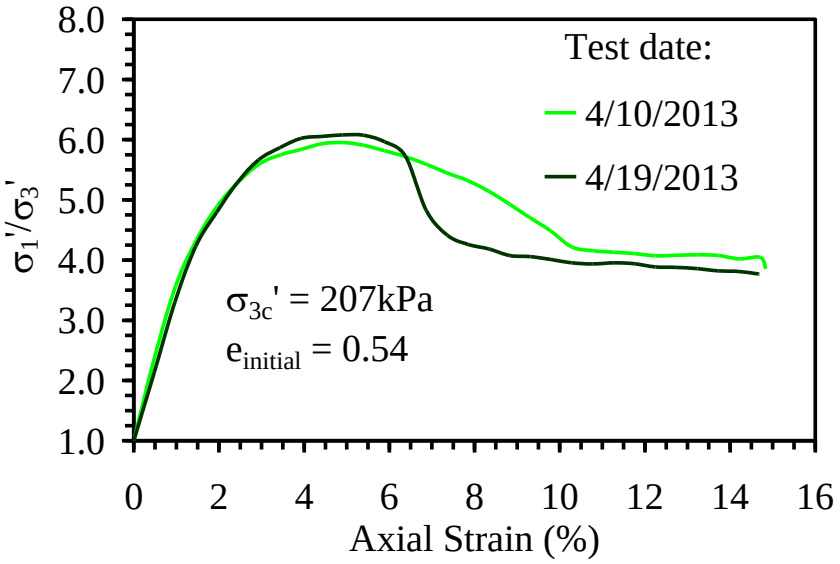

Figure 5.48: Principal stress ratio with axial strain of triaxial compression test on dry Mason sand performed at a time to 15% axial strain of 15 minutes

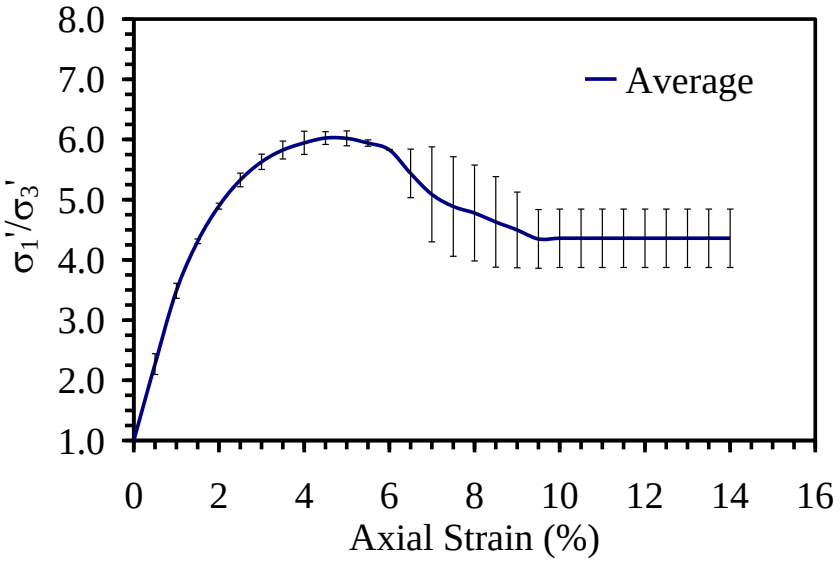

Figure 5.49: Average principal ratio difference and error bars with axial strain of triaxial compression test on all dry Mason sand performed at a time to 15 % axial strain of 15 minutes

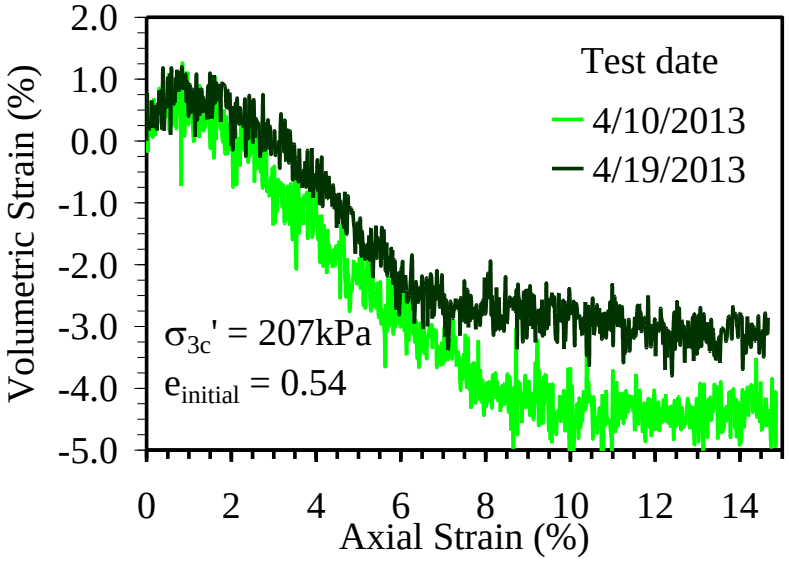

Figure 5.50: Volumetric strain with axial strain of triaxial compression test on dry Mason sand performed at a time to 15% axial strain of 15 minutes

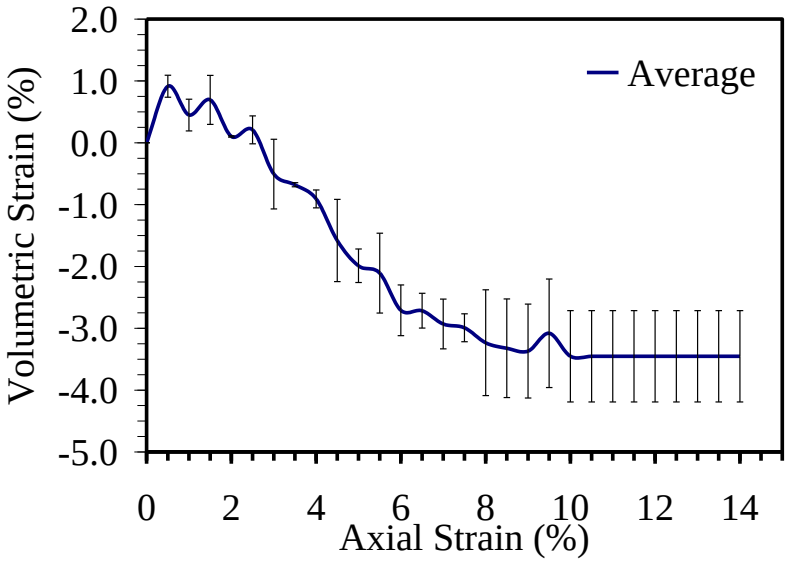

Figure 5.51: Average volumetric strain and error bars with axial strain of triaxial compression test on all dry Mason sand performed at a time to 15 % axial strain of 15 minutes

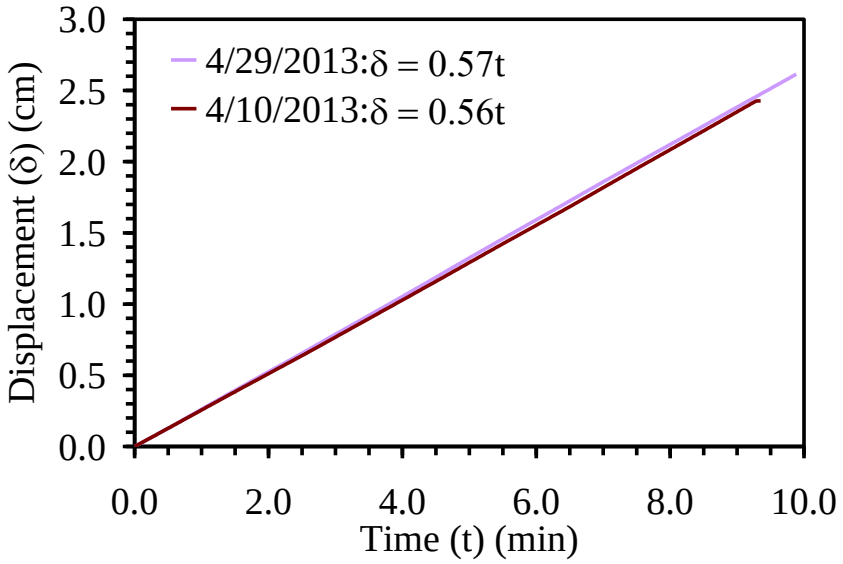

Figure 5.52: Axial displacement with time of testing of triaxial compression tests on dry Mason sand performed at a time to 15 % axial strain of 10 minutes

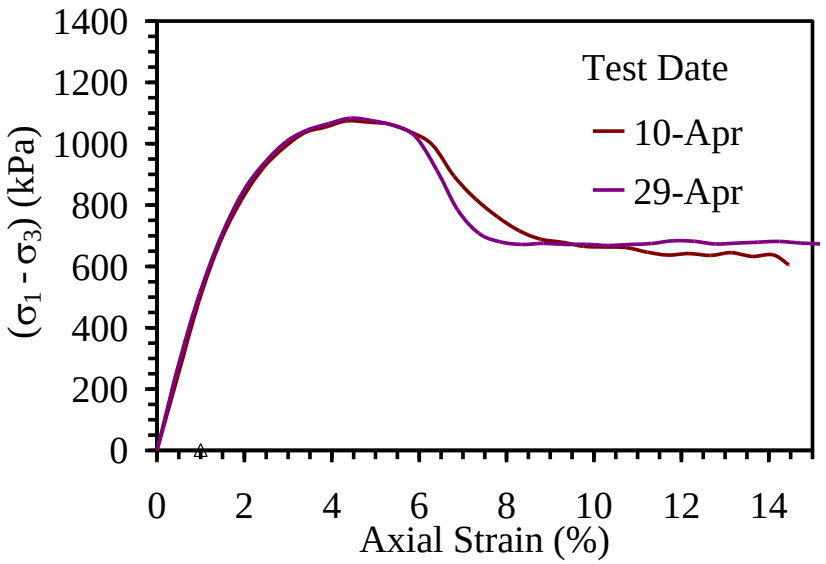

Figure 5.53: Principal stress difference with axial strain of triaxial compression test on dry Mason sand performed at a time to 15% axial strain of 10 minutes

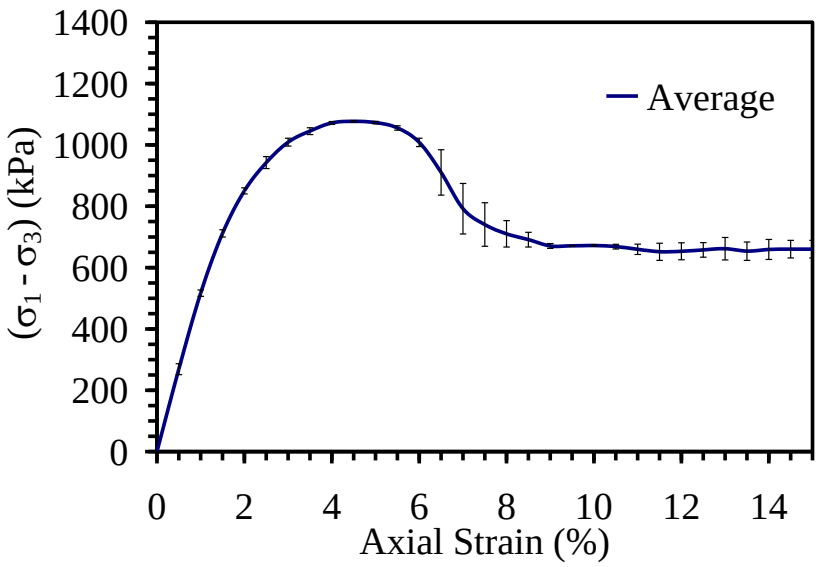

Figure 5.54: Average principal stress difference and error bars with axial strain of all triaxial compression tests on dry Mason sand performed at a time to 15% axial strain of 10 minutes

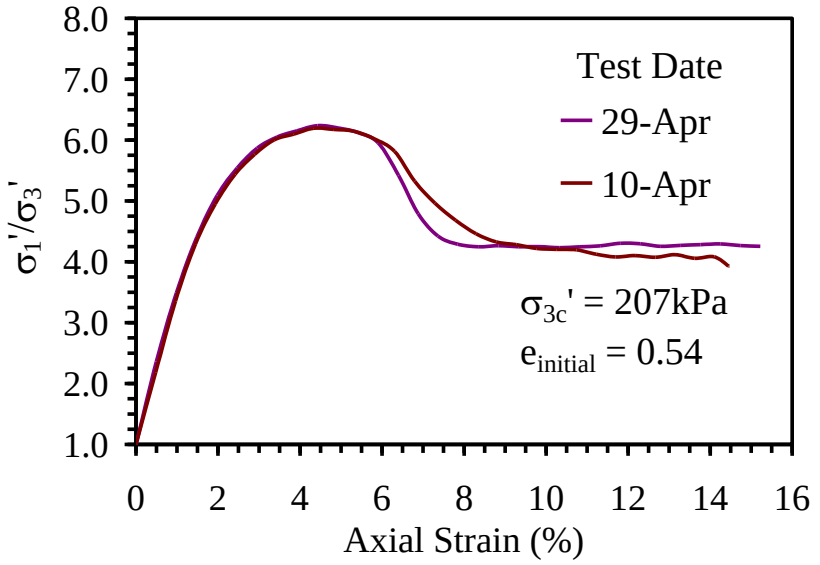

Figure 5.55: Principal stress ratio with axial strain of triaxial compression test on dry Mason sand performed at a time to 15% axial strain of 10 minutes

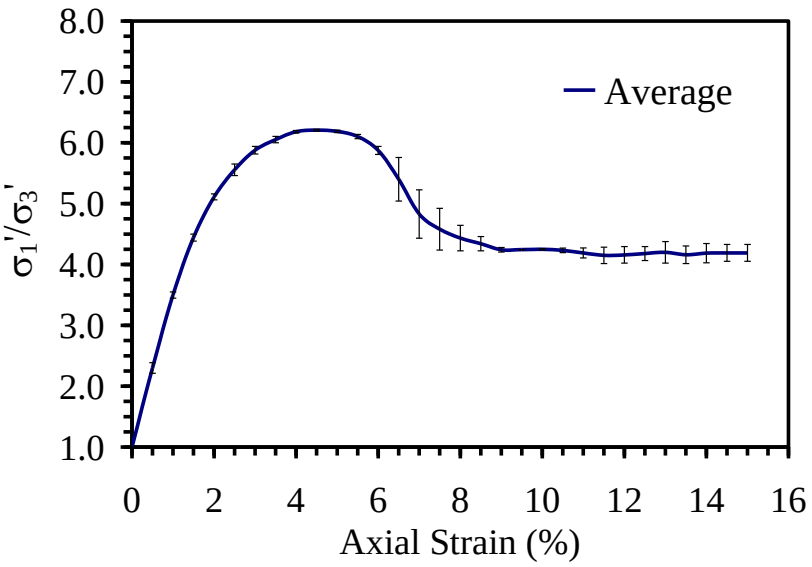

Figure 5.56: Average principal stress difference and error bars with axial strain of all triaxial compression tests on dry Mason sand performed at a time to 15% axial strain of 10 minutes

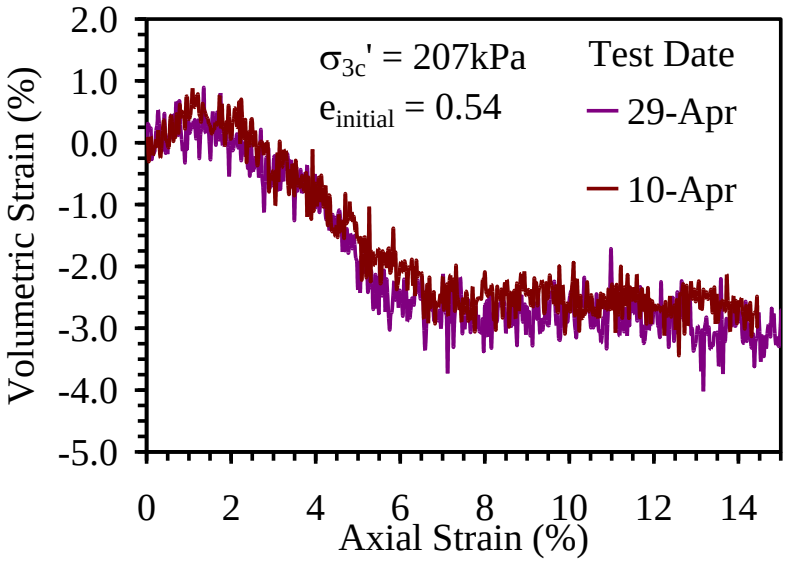

Figure 5.57: Volumetric stain with axial strain of triaxial compression test on dry Mason sand performed at a time to 15% axial strain of 10 minutes

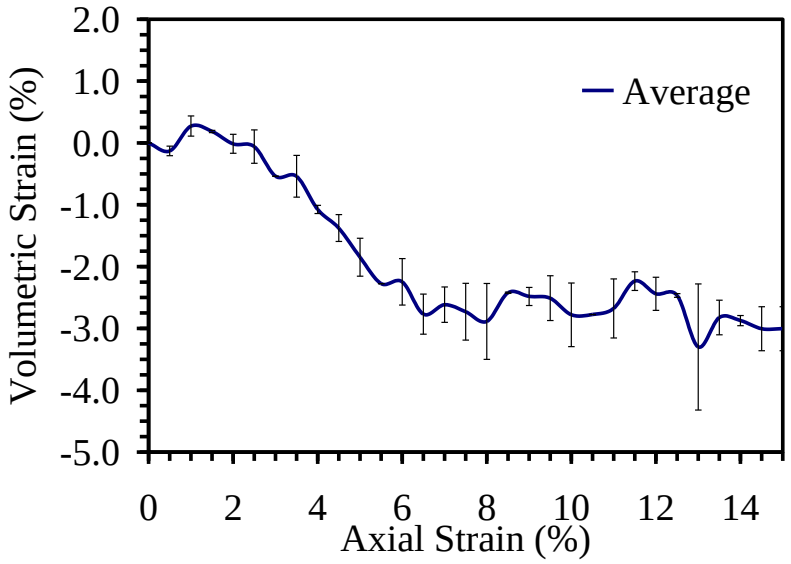

Figure 5.58: Average volumetric stain and error bars with axial strain of all triaxial compression tests on dry Mason sand performed at a time to 15% axial strain of 10 minutes

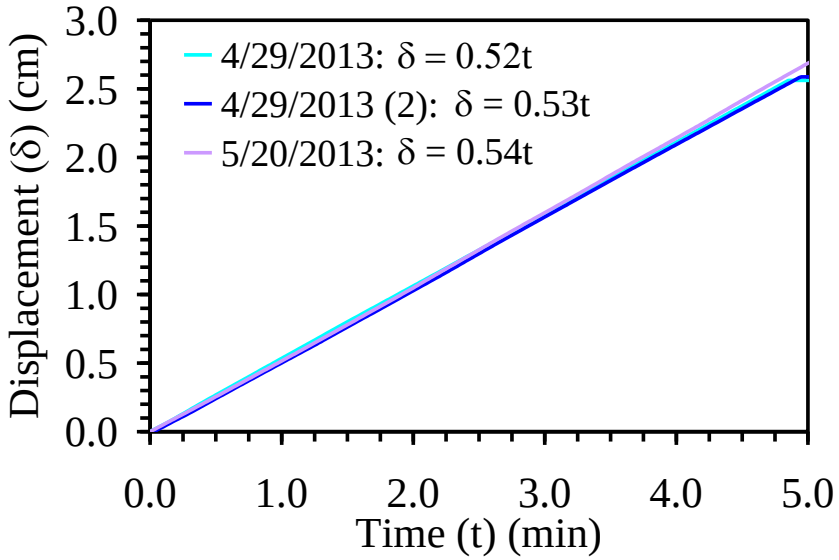

Figure 5.59: Axial displacement with time of triaxial compression tests on dry Mason sand performed at a time to 15 % axial strain of 5 minutes

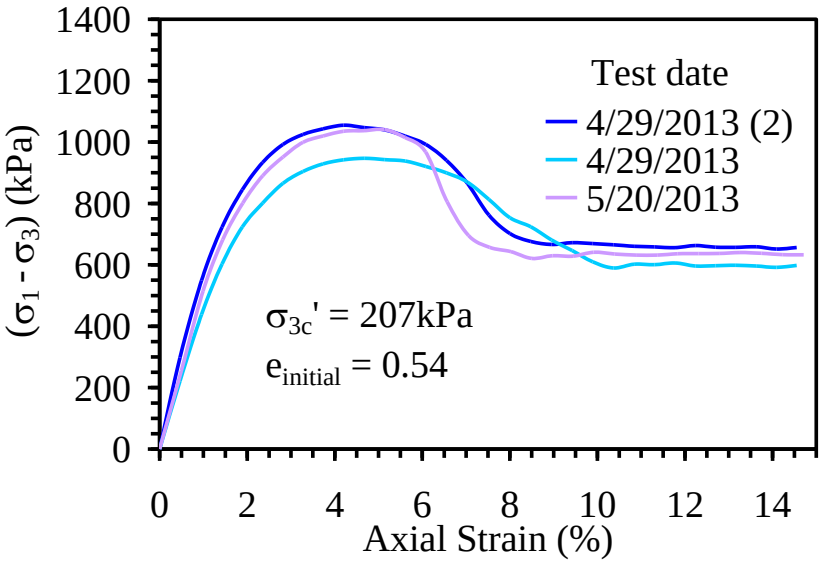

Figure 5.60: Principal stress difference with axial strain of triaxial compression test on dry Mason sand performed at a time to 15% axial strain of 5 minutes

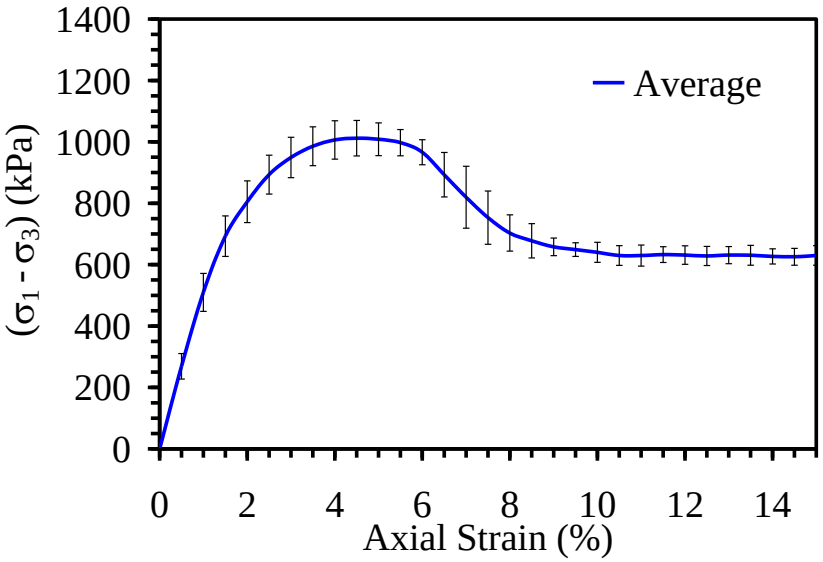

Figure 5.61: Average principal stress difference and error bars with axial strain of all triaxial compression tests on dry Mason sand performed at a time to 15% axial strain of 5 minutes

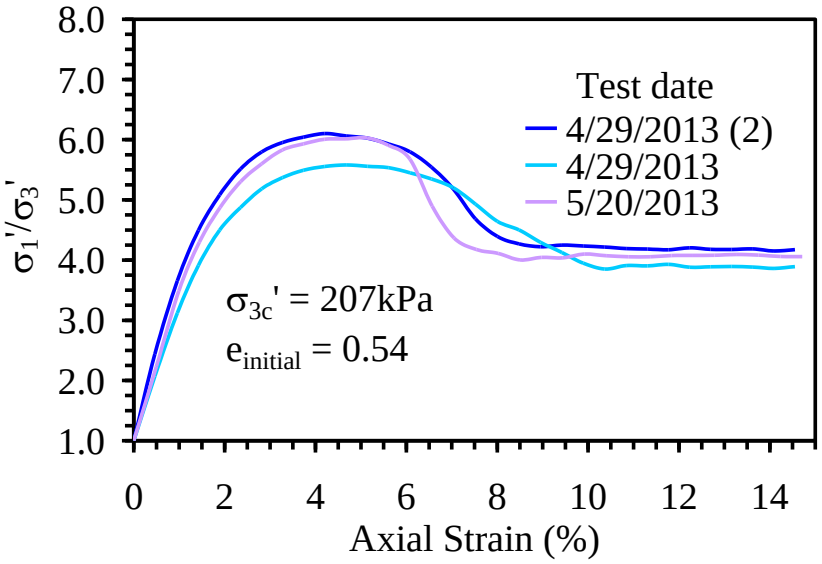

Figure 5.62: Principal stress ratio with axial strain of triaxial compression test on dry Mason sand performed at a time to 15% axial strain of 5 minutes

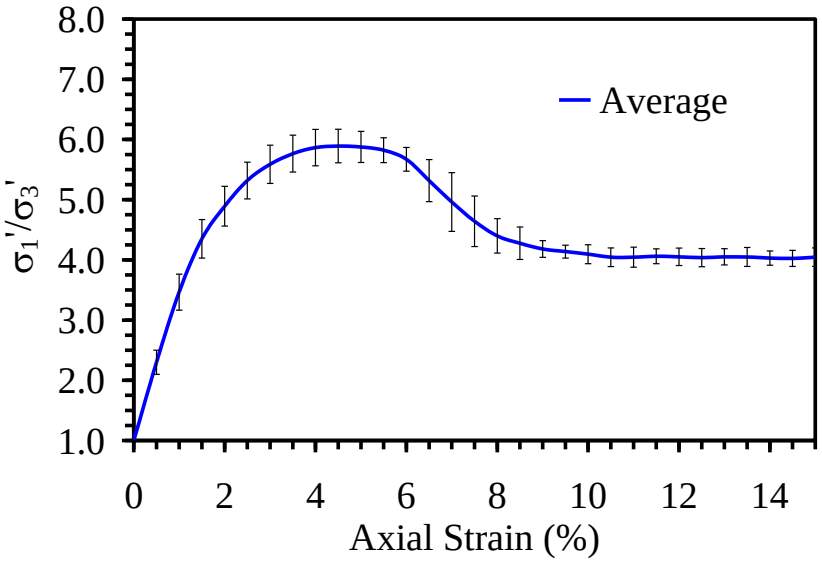

Figure 5.63: Average principal stress ratio and error bars with axial strain of all triaxial compression tests on dry Mason sand performed at a time to 15% axial strain of 5 minutes

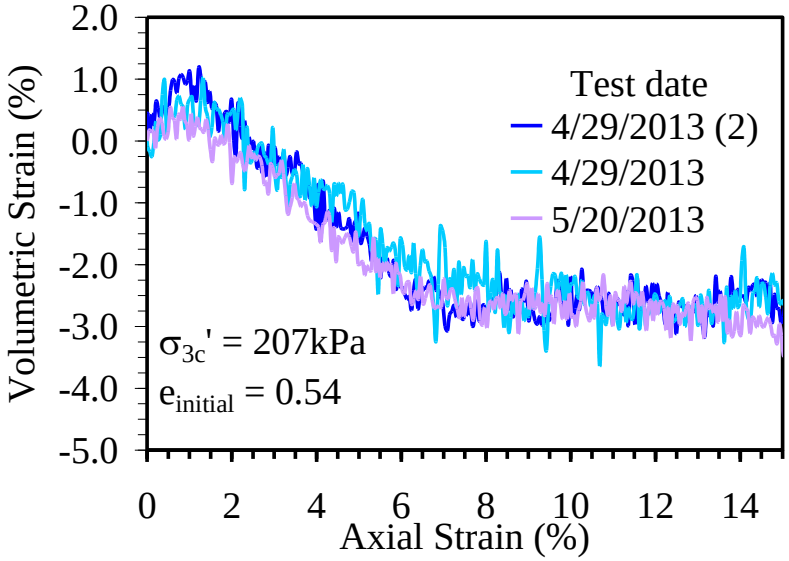

Figure 5.64: Volumetric strain with axial strain of triaxial compression test on dry Mason sand performed at a time to 15% axial strain of 5 minutes

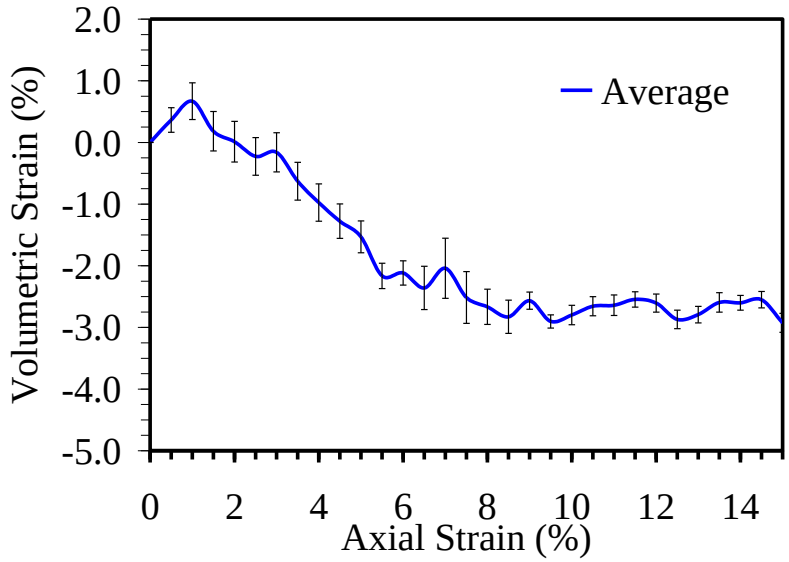

Figure 5.65: Average volumetric strain and error bars with axial strain of all triaxial compression tests on dry Mason sand performed at a time to 15% axial strain of 5 minutes

6.0 Rate Effects on Boulder Clay

This chapter presents the preparation of the specimens and results for triaxial compression tests performed on Boulder clay. The first section discusses the preparation and results of CU test on saturated Boulder clay specimens at various strain rates. The second section discusses the preparation and results of CU tests on unsaturated Boulder clay specimens at various strain rates. The third section presents the results of UU Boulder clay tests at various strain rates.

6.1 Saturated Boulder Clay Rate Effects

6.1.1 Preparation and Shearing Procedures of Saturated Boulder Clay

To investigate the effects of strain rate on the shear strength of Boulder clay, three consolidated undrained (CU) triaxial tests were performed at three separate strain rates: 0.1, 1.5, and 14.5%/minute corresponding to times to 15% axial strain of 150, 10 and 1 minute. Each specimen was prepared and saturated using identical procedures discussed in the Chapter 3 Section 3.3.8 to prepare and saturate the standard CU tests. The Skempton's B parameters, cell pressures and backpressures at the end of saturation are provided in Table 6.1.

Table 6.1: Saturation details for shearing rate tests on Boulder clay

Time to 15% axial strain (min)	Shearing Rate (mm/min)	Strain Rate (%/min)	σ_{cell} (kPa)	σ_{back} (kPa)	B
150	0.0686	0.1	588	552	0.82
10	1.10	1.5	276	241	0.80
1.0	10.0	14	310	276	0.87

After saturation, each specimen was consolidated to 207 kPa before shearing. The specimens were sheared until reaching an axial strain of 15%, which corresponded to times to failure of 150, 10 and 1 minute for the strain rates mentioned above. The initial water content and void ratio after specimen preparation and the void ratios after consolidation for the three tests are presented in Table 6.2.

Table 6.2: Boulder clay initial conditions after specimen preparation

Time to 15% axial strain (min)	Rate (mm/min)	Strain Rate (%/min)	ω_i %	e_i	e_{consol}
150	0.0686	0.1	17.3	0.51	0.46
10	1.10	1.5	17.8	0.53	0.50
1	10.0	14	17.9	0.53	0.47

6.1.2 Results from Triaxial Compression Tests on Saturated Boulder Clay

The stress strain curves for the three tests are shown in Figure 6.1. The principal stress ratio versus axial strain is shown in Figure 6.2. The excess pore water pressure versus axial strain is shown in Figure 6.3. The point of SPT failure is identified in Figures 6.1, 6.2 and 6.3 with a hollow square. From Figure 6.1 and 6.3, it is clear that the principal stress difference increases with increased strain rate and the pore water pressure decreases with increased strain rate. The initial tangent modulus (slope of $(\sigma_1-\sigma_3)$ versus axial strain curve approximately between an axial strain of 0 - 1%) also appears to increases with increased strain rate.

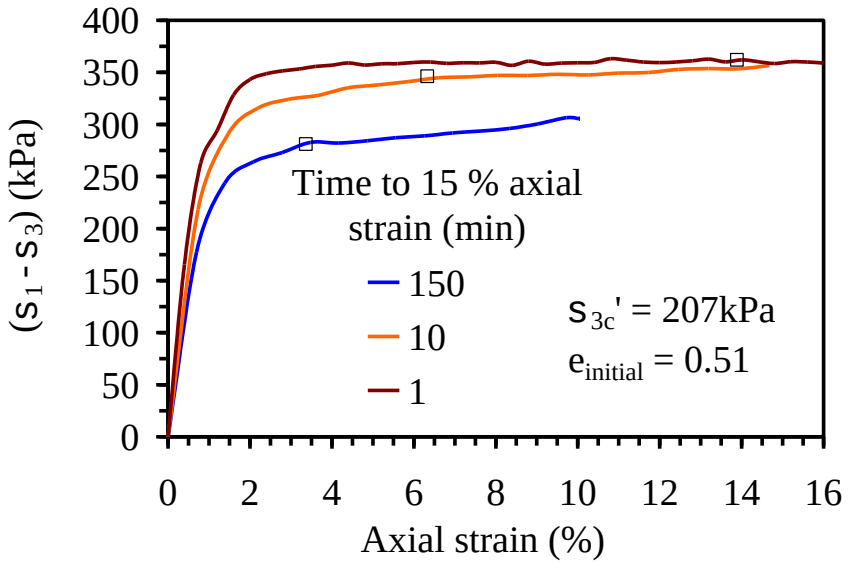

Figure 6.1: Principal stress difference with axial strain for triaxial compression tests on saturated Boulder clay performed at different axial strain rates.

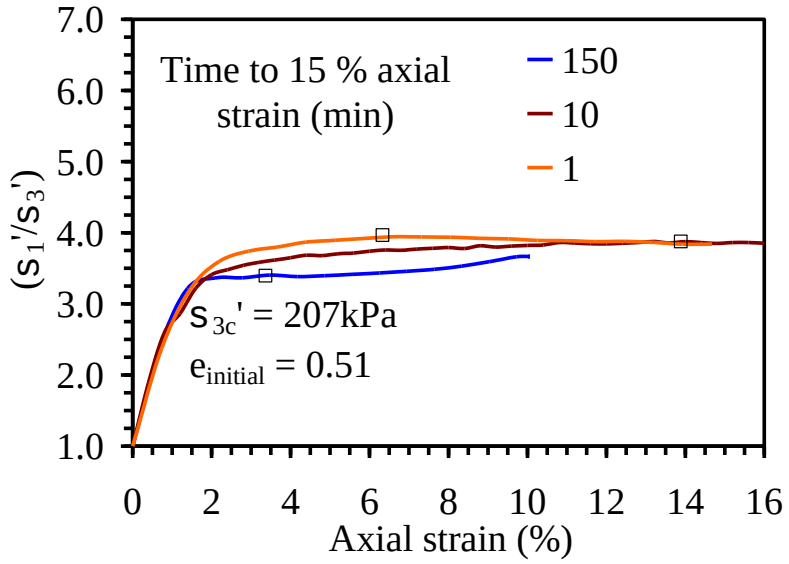

Figure 6.2: Principal stress ratio with axial strain for triaxial compression tests on saturated Boulder clay performed at different axial strain rates.

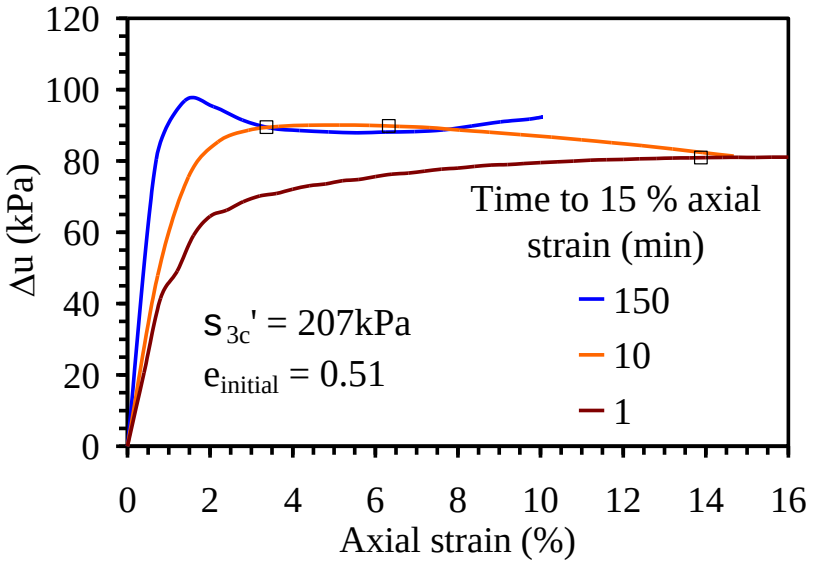

Figure 6.3: Excess pore water pressure with axial strain for triaxial compression tests on saturated Boulder clay performed at different axial strain rates.

6.2 Unsaturated Boulder Clay Rate Effects

6.2.1 Preparation and Shearing Procedures for Unsaturated Boulder clay Specimens

To understand the effects of shearing rate on Boulder clay in unsaturated conditions, CU triaxial tests were performed on specimens subjected to values of matric suction equal to 34 and 140 kPa. Each specimen was sheared until reaching an axial strain of 15% in either 150 minutes or 1 minute (axial strain rates of 0.1 and 14.5%/min, respectively) under constant net stress conditions. Each specimen was compacted, saturated, and consolidated using identical procedures to the saturated tests.

The axis translation technique was used to independently control the pore air and pore water pressures in the specimen. A known air pressure was applied to the top of the specimen and a known water pressure to the bottom of the specimen. The difference between the applied air and water pressure is equal to the desired matric suction ($\psi = u_a - u_w$). To apply this technique, the top air pressure was applied through a coarse porous stone while the bottom water pressure was applied through a high air entry (HAE) ceramic disk with a diameter of 76 mm (greater than that of the specimen). The air entry value of the disks used was 100 kPa for the tests at suction values of 34 kPa and was 300 kPa for the test at a suction of 140 kPa. The specimen was assumed to have uniform matric suction throughout when outflow from the specimen into a graduated burette remained constant for 24 hours. Outflow curves for three of the four unsaturated tests are shown in Figure 6.4. A summary of the initial water contents, void ratios, consolidation void ratios and B-values for the specimens is provided in Table 6.3. A summary of the consolidation details for unsaturated Boulder clay tests is provided in Table 6.4.

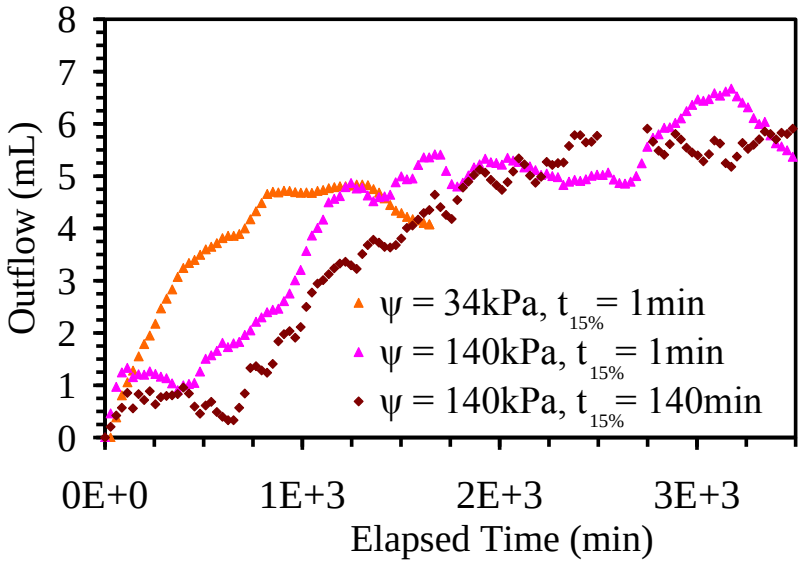

Figure 6.4: Outflow with time for triaxial compression tests on unsaturated Boulder clay

Table 6.3: Initial conditions and saturation details of unsaturated Boulder clay tests

Time to 15% axial strain (min)	Rate (mm/min)	Strain Rate (%/min)	Suction (kPa)	ω_i (%)	e_i	e_{consol}	B
150	0.069	0.1	0	17.3	0.51	0.46	0.82
150	0.069	0.1	34	18.0	0.54	0.50	0.86
150	0.069	0.1	140	16.7	0.52	0.51	0.84
1	10.0	14.6	0	17.9	0.50	0.47	0.87
1	10.0	14.6	34	19.5	0.52	0.47	0.91
1	10.0	14.6	70	17.0	0.53	0.52	0.75
1	10.0	14.3	140	17.8	0.53	0.51	0.91

Table 6.4: Consolidation details of unsaturated Boulder clay tests

Time to 15% axial strain (min)	Rate (mm/min)	Strain Rate (%/min)	Suction (kPa)	σ_3' (kPa)	$\sigma_{confining}$ (kPa)	σ_{back} (kPa)
150	0.069	0.1	0	207	768	559
150	0.069	0.1	34	207	483	276
150	0.069	0.1	140	207	517	310
1	10.0	14.6	0	207	483	276
1	10.0	14.6	34	207	483	276
1	10.0	14.6	70	207	483	276
1	10.0	14.3	140	207	483	276

6.2.2 Unsaturated Boulder Clay Results

The principal stress difference versus axial strain for the saturated and unsaturated tests run at times to an axial strain of 15% in 150 minutes and 1 minute are shown in Figures 6.5(a) and 6.5(b). From these figures, it is apparent that there is an increase in the principal stress difference with increased matric suction as well as well as increased strain rate. Similarly, the principal stress ratio versus axial strain for saturated and unsaturated tests is plotted in Figure 6.6(a) for tests run at a time to an axial strain of 15% in 150 minutes and 6.6(b) for tests run at a time to an axial strain of 15% in 1 minute. The excess pore water pressure versus axial strain for the saturated and unsaturated tests is shown in Figure 6.7(a) for tests run at a time to an axial strain of 15% in 150 minutes and Figure 6.7(b) for tests run at a time to an axial strain of 15% in 1 minute. The excess pore water pressures for the different specimens shown in Figure 6.7 decrease with increasing strain rate for matric suction values of 0 and 140 kPa but increase with increasing strain rate for a matric suction value of 34 kPa. The difference in behavior for the specimen with a matric suction of 34 kPa could be that the degree of saturation is relatively high at greater than 90% so compression of the voids will lead to generation of positive excess pore water pressure. Further, the hydraulic conductivity of the unsaturated specimen at 34 kPa suction is less than that of the saturated specimen. Given the potential of the 34 kPa specimen to still generate relatively high excess pore pressures along with a decreased hydraulic conductivity, during faster shearing tests the excess pore pressure may not be able to dissipate away from the shear plane as quickly as the saturated specimen and higher excess pore pressure could be measured. During slower shearing tests, the excess pore water pressure generated was similar in all three tests [Figure 6.7(a)].

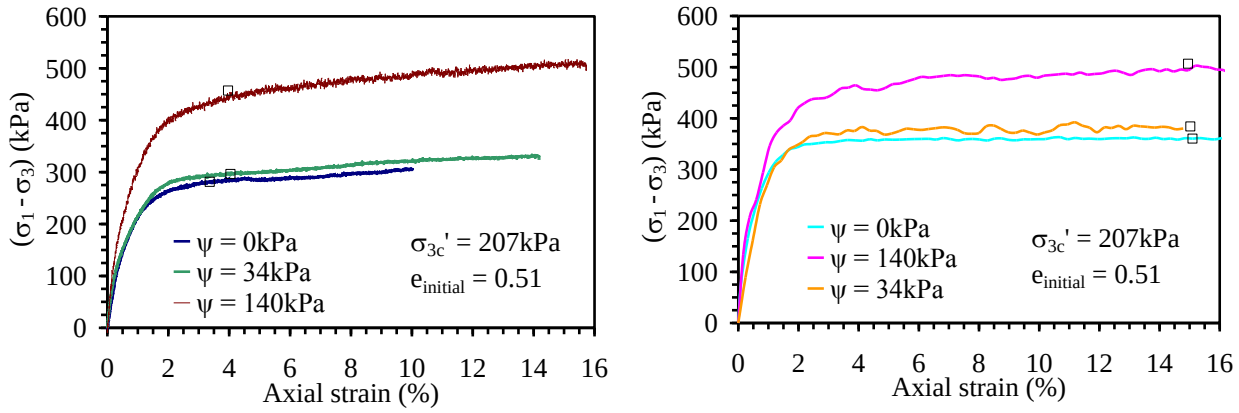

Figure 6.5: Principal stress difference with axial strain for triaxial compression tests on unsaturated and saturated Boulder clay run at times to 15% axial strain of: (a) 150 minutes and (b) 1 minute

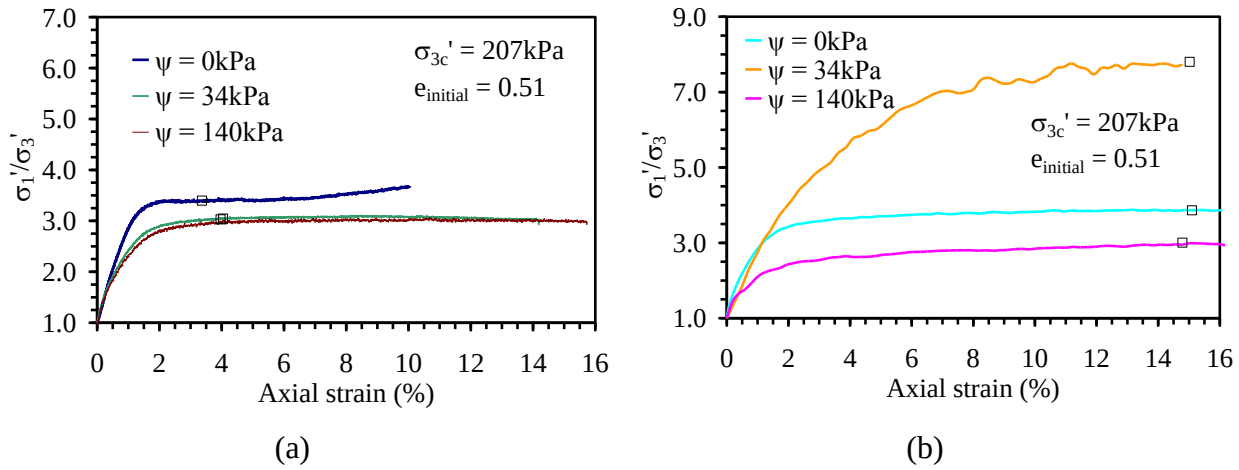

Figure 6.6: Principal stress ratio with axial strain for triaxial compression tests on unsaturated and saturated Boulder clay run at times to failure at 15% axial strain of: (a) 150 minutes and (b) 1 minute

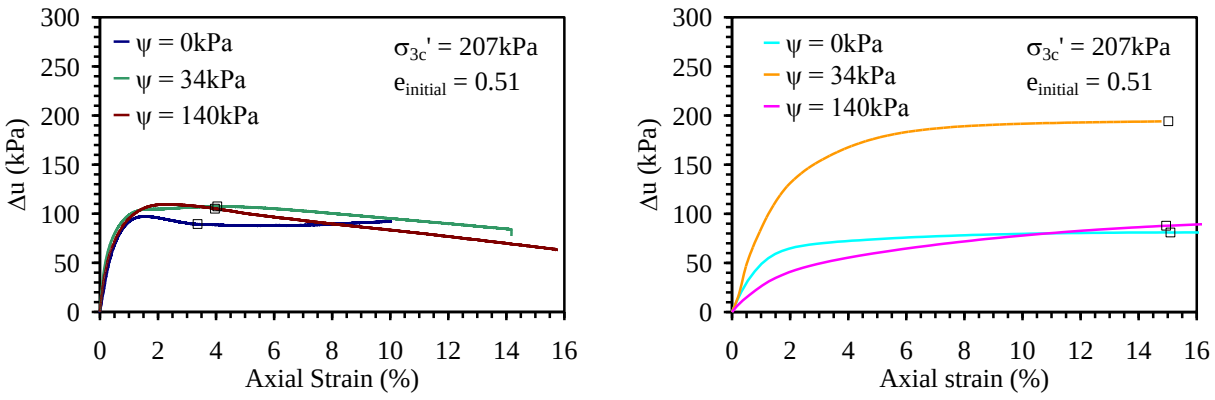

(a) (b)

Figure 6.7: Excess pore water pressure with axial strain for triaxial compression tests on unsaturated and saturated Boulder clay tests run at times to failure at 15% axial strain of: (a) 150 minutes and (b) 1 minute

6.3 Unconsolidated Undrained Boulder Clay Rate Effects

6.3.1 Preparation and Shearing Procedures for Unconsolidated Undrained Boulder Clay

To further characterize the effects of strain rate on the shear strength of Boulder clay in an unsaturated state, a series of unconsolidated undrained (UU) triaxial compression tests in accordance with ASTM D2850 were performed. Each specimen used was compacted using identical procedures used in previous tests to an initial target void ratio of 0.51 with target compaction water contents of 13, 16.5, 17.5, or 19.5%. Once a specimen was prepared and a latex membrane placed around it, the triaxial cell was assembled and filled with de-aired water. A confining pressure of 207 kPa was immediately applied to the cell and the specimen allowed to rest without drainage for a minimum of 10 minutes then sheared. For each water content, three different specimens were sheared at three different axial strain rates: 0.1, 1.5, and 14.5 %/minute corresponding to times to 15% axial strain of 150, 10 and 1 minute. During shear, the axial load and vertical displacement was recorded. Summaries of the compaction water content, degree of saturation and initial void ratio for UU tests is provided in Table 6.5 for a target water content of

19.5%, Table 6.6 for a target water content of 17.5%, Table 6.7 for a target water content of 16.5 and Table 6.8 for a target water content of 13%.

Table 6.5: Specimen details of UU tests with a target compaction water content of 19.5%

Time to 15% axial strain (min)	Strain rate (%/min)	$w_{compaction}$ (%)	$S_{compaction}$ (%)	$e_{compaction}$
150	0.1	19.9	100.0	0.53
10	1.5	19.9	100.0	0.53
1	14.5	19.9	99.9	0.54

Table 6.6: Specimen details of UU tests with a target compaction water content of 17.5%

Time to 15% axial strain (min)	Strain rate (%/min)	$w_{compaction}$ (%)	$S_{compaction}$ (%)	$e_{compaction}$
150	0.1	17.4	90.1	0.52
10	1.5	17.4	91.3	0.51
1	14.5	17.4	94.7	0.53

Table 6.7: Specimen details of UU tests with a target compaction water content of 16.5%

Time to 15% axial strain (min)	Strain rate (%/min)	$w_{compaction}$ (%)	$S_{compaction}$ (%)	$e_{compaction}$
150	0.1	15.6	86.0	0.53
10	1.5	16.3	81.0	0.54
1	14.3	16.5	81.0	0.52

Table 6.8: Specimen details for UU tests with a target compaction water content of 13%

Time to 15% axial strain (min)	Strain rate (%/min)	$w_{compaction}$ (%)	$S_{compaction}$ (%)	$e_{compaction}$
150	0.1	13.5	69.6	0.52
10	1.5	13.5	70.0	0.52
1	14.3	13.5	68.3	0.53

6.3.2: Unconsolidated Undrained Boulder Clay Results

The principal stress difference versus axial strain for the tests with a compaction water content of 19.5% run at times to an axial strain of 15% in 150, 10 and 1 minute are shown in Figure 6.8. Similar plots for compaction water contents of 17.5, 16.5 and 13% are shown in

Figures 6.9, 6.10, and 6.11 respectively. From these figures, it is evident that regardless of the compaction water content, there is an increase in the principal stress difference with increasing strain rate. The principal stress difference versus axial strain plotted for tests performed at a times to reach an axial strain of 15% of 150, 10 and 1 minute for the four different compaction water contents is shown in Figures 6.12, 6.13 and 6.14 respectively. From the results shown in these figures, it is clear that the principal stress difference increases with decreasing water content regardless of the applied strain rate. Although the specimens compacted at different water contents have different initial suction values, the compacted specimens likely have different soil structures than the constant net stress CU triaxial tests where a known suction value is applied to the specimens. Thus, it is difficult to confidently assess the exact role of suction on the shear strength.

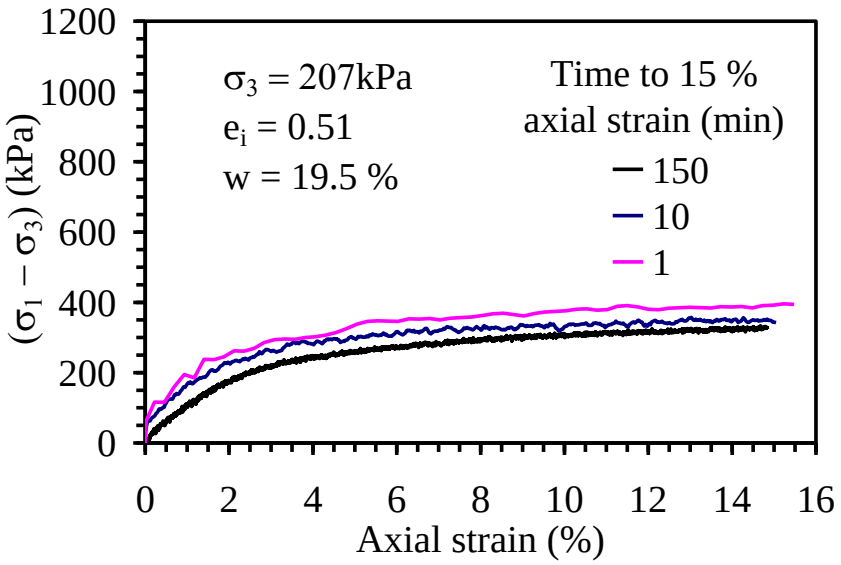

Figure 6.8: Principal stress difference with axial strain for UU triaxial compression tests compacted with a target water content of 19.5% performed at different axial strain rates

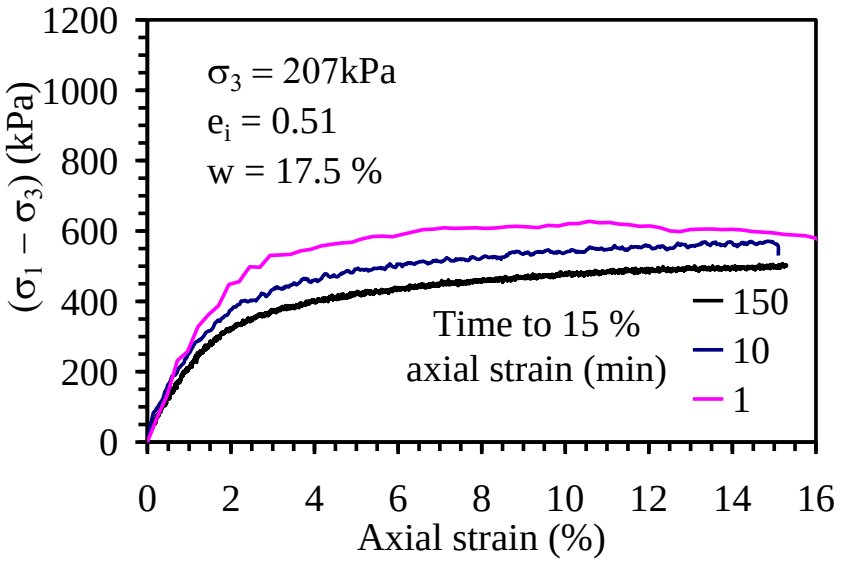

Figure 6.9: Principal stress difference with axial strain for UU triaxial compression tests compacted with a target water content of 17.5% performed at different axial strain rates.

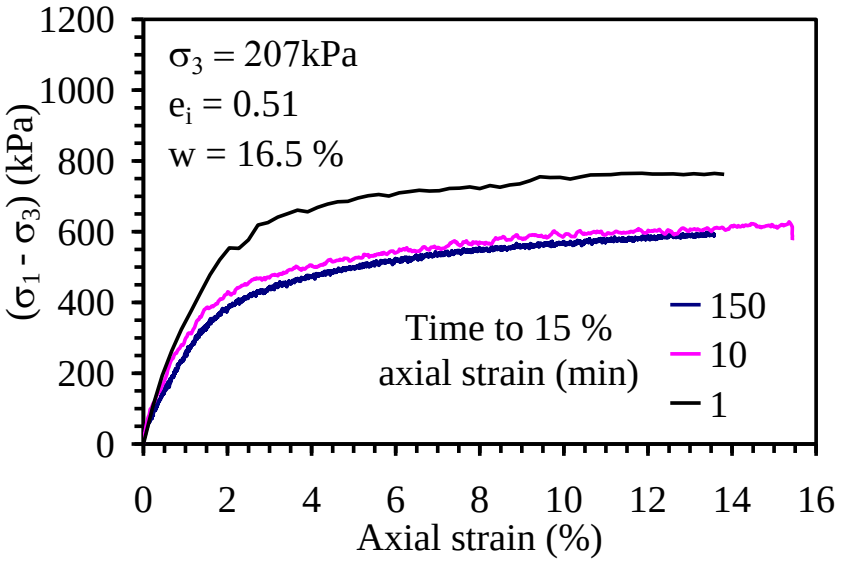

Figure 6.10: Principal stress difference versus axial strain for UU tests compacted with a target compaction water content of 16.5% performed at times to reach an axial strain of 15% in 150, 10 and 1 minutes

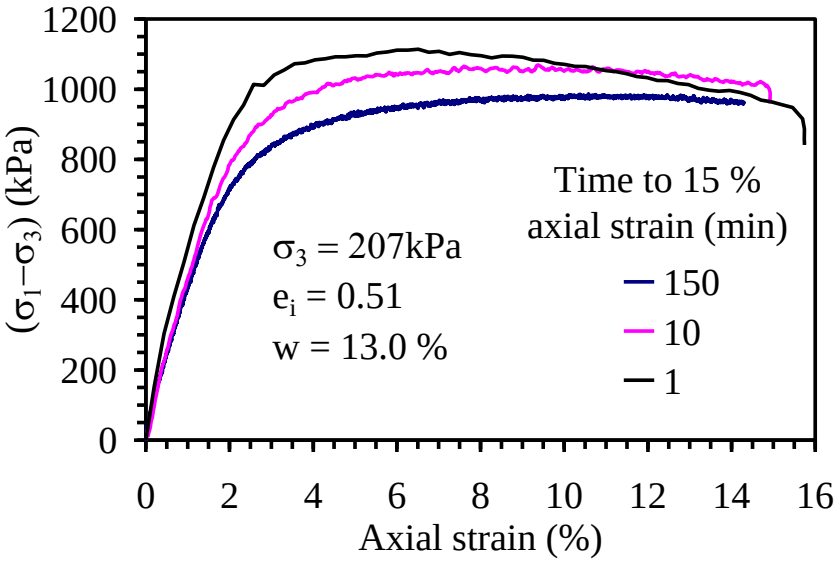

Figure 6.11: Principal stress difference with axial strain for UU triaxial compression tests compacted with a target water content of 13% performed at different axial strain rates

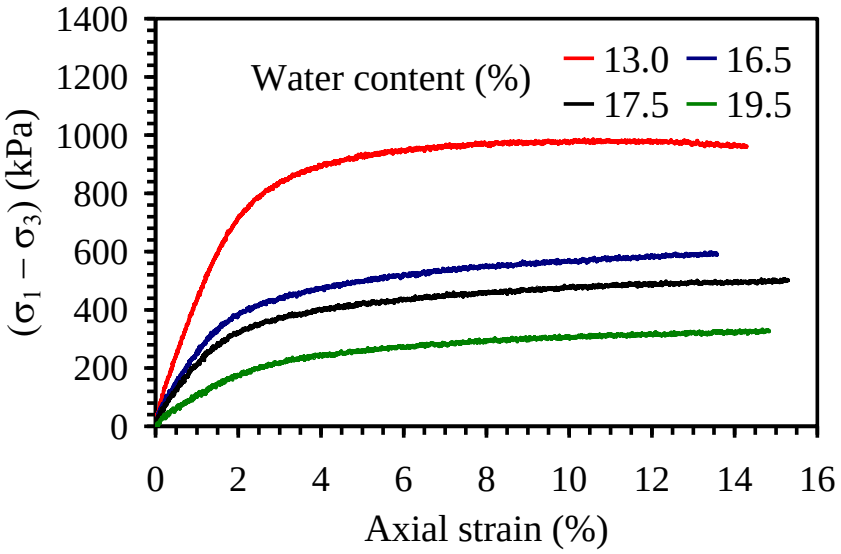

Figure 6.12: Principal stress difference with axial strain for UU triaxial compression tests compacted at different water contents performed at a time to 15% axial strain of 150 minutes

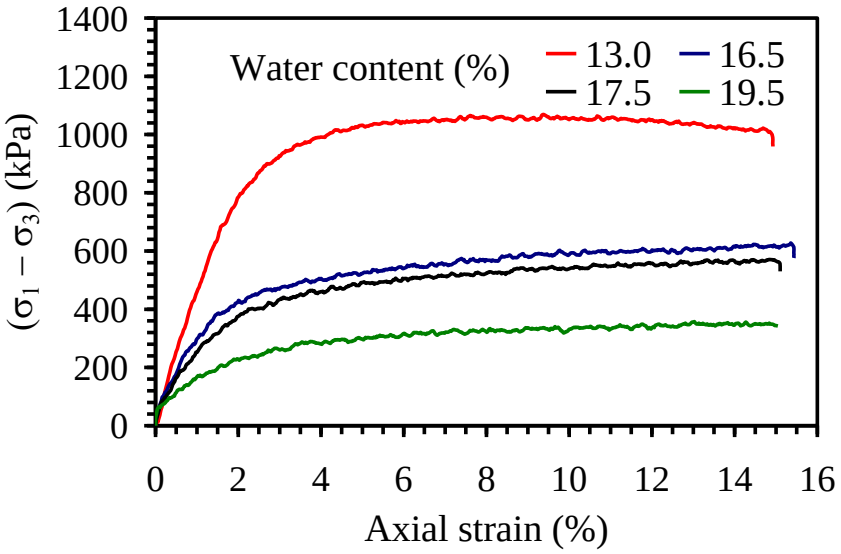

Figure 6.13: Principal stress difference with axial strain for UU triaxial compression tests compacted at different water contents performed at a time to 15% axial strain of 10 minutes

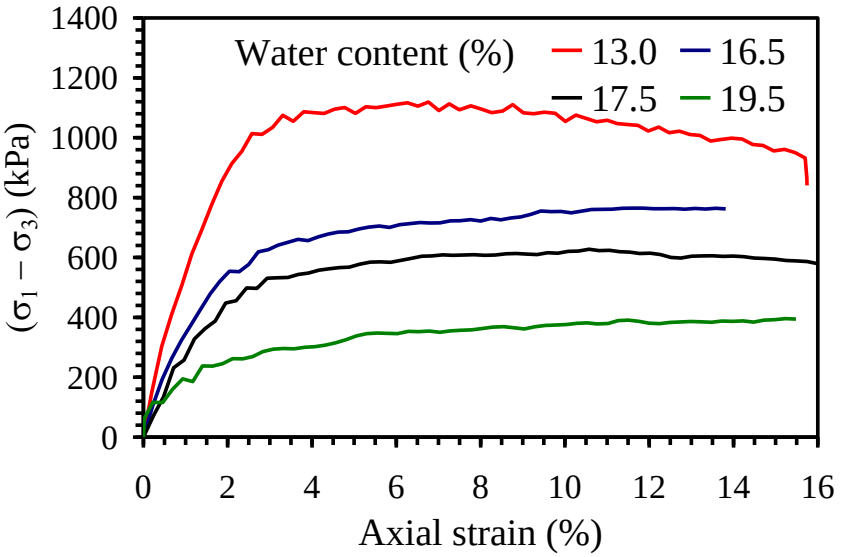

Figure 6.14: Principal stress difference with axial strain for UU triaxial compression tests compacted at different water contents performed at a time to 15% axial strain of 1 minutes

6.4 Repeatability of CU Tests on Boulder Clay

To prove repeatability of the consolidated undrained triaxial compression tests on Boulder clay, all tests with the exception of the test run at a time to 15% axial strain of 150 minutes minimum were performed a minimum of two times. The first section provides the principal

stress difference, principal stress ratio and excess pore water pressure with axial strain for all multiple saturated tests performed. The second section shows the principal stress difference, principal stress ratio and excess pore water pressure with axial strain for multiple unsaturated tests performed.

6.4.1 Repeatability of Saturated Boulder Clay Tests

Figures 6.15 through 6.21 shows the axial displacement with time of testing, principal stress difference, average principal stress difference and error bars, principal stress ratio, average principal stress ratio and error bars, excess pore water pressure, and average excess pore water pressure and error bars with axial strain for all saturated Boulder clay tests performed at a time to 15% axial strain of 10 minutes. Figures 6.22 through 6.28 shows the axial displacement with time of testing, principal stress difference, average principal stress difference and error bars, principal stress ratio, average principal stress ratio and error bars, excess pore water pressure, and average excess pore water pressure and error bars with axial strain for all saturated Boulder clay tests performed at a time to 15% axial strain of 1 minute.

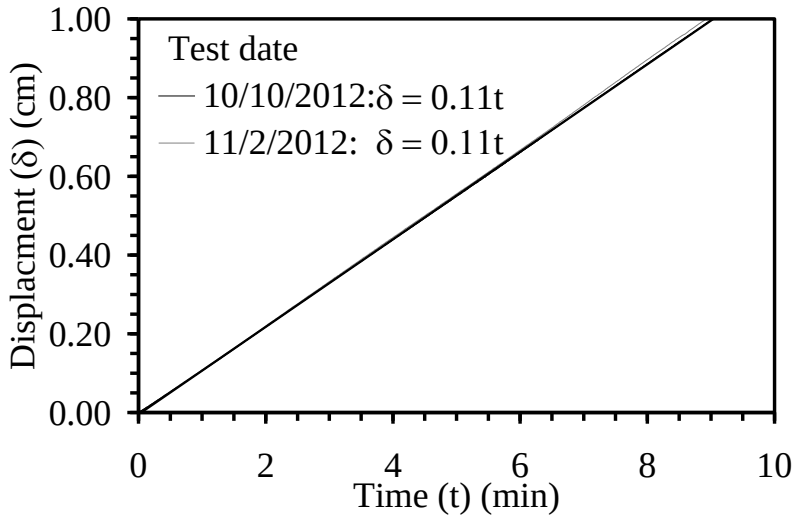

Figure 6.15: Axial displacement with time of testing for triaxial compression tests on saturated Boulder clay performed at a time to 15 % axial strain of 10 minutes

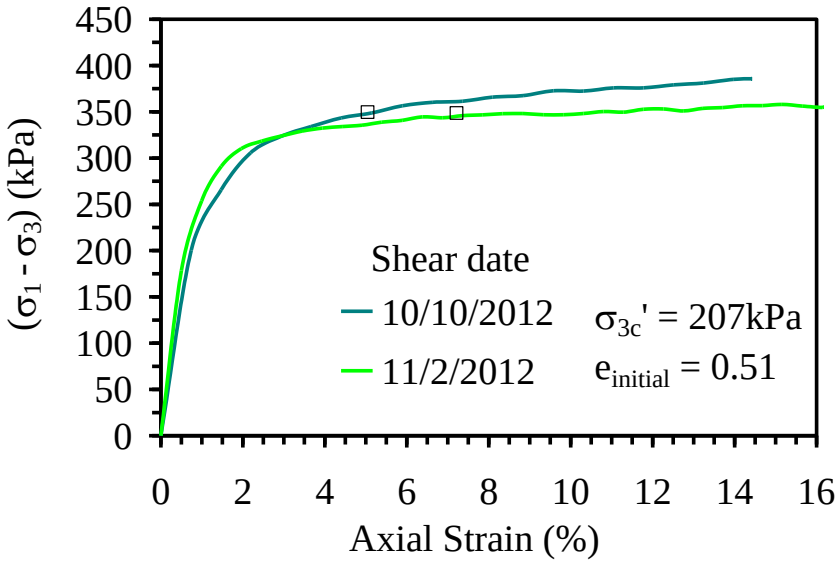

Figure 6.16: Principal stress difference with axial strain for triaxial compression tests on saturated Boulder clay tests performed at a time to 15% axial strain of 10 minutes

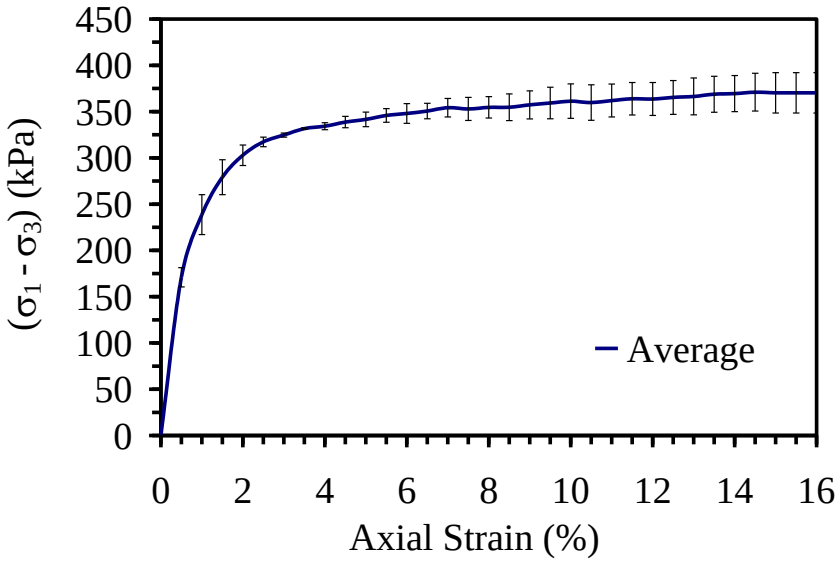

Figure 6.17: Average principal stress difference and error bars with axial strain for all triaxial compression tests performed on saturated Boulder clay at a time to 15% axial strain of 10 minute

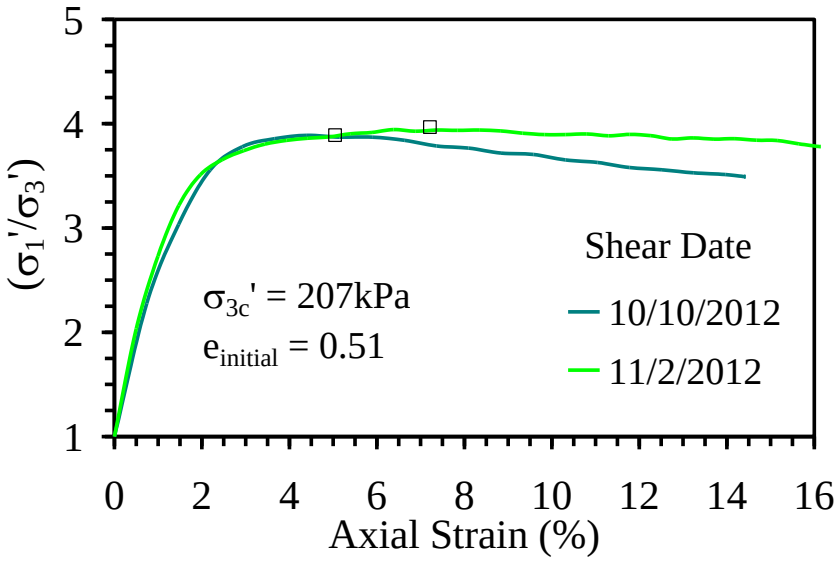

Figure 6.18: Principal stress ratio with axial strain for triaxial compression tests on saturated Boulder clay performed at a time to 15% axial strain of 10 minutes

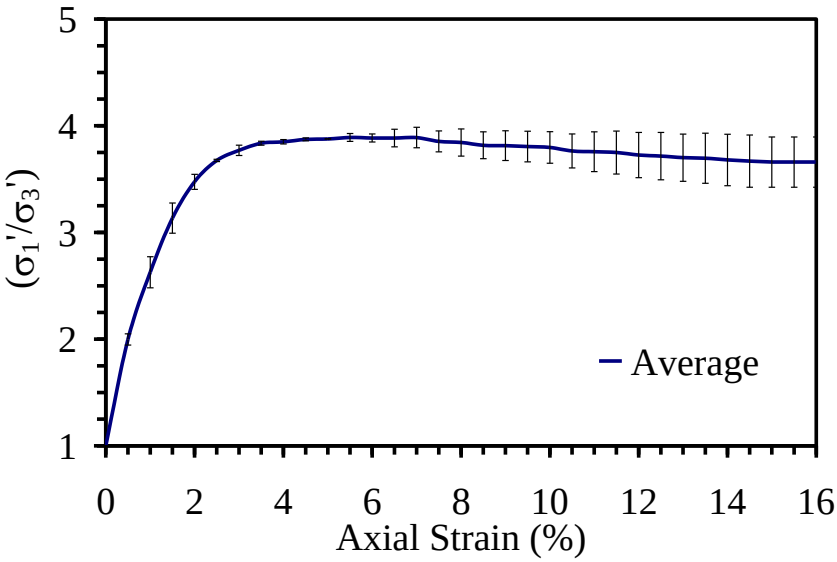

Figure 6.19: Average principal stress ratio and error bars with axial strain for all triaxial compression tests performed on saturated Boulder clay at a time to 15% axial strain of 10 minute

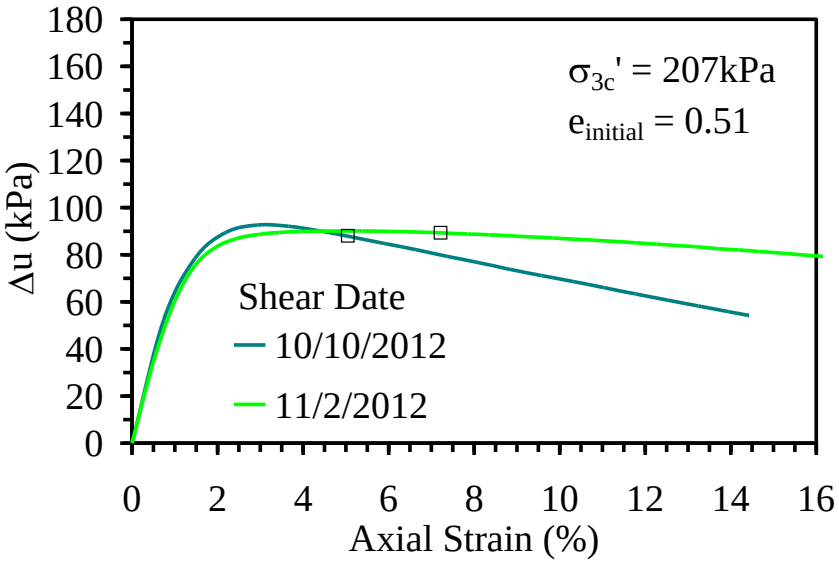

Figure 6.20: Excess pore water pressure with axial strain for triaxial compression tests on saturated Boulder clay performed at a time to 15% axial strain of 10 minutes

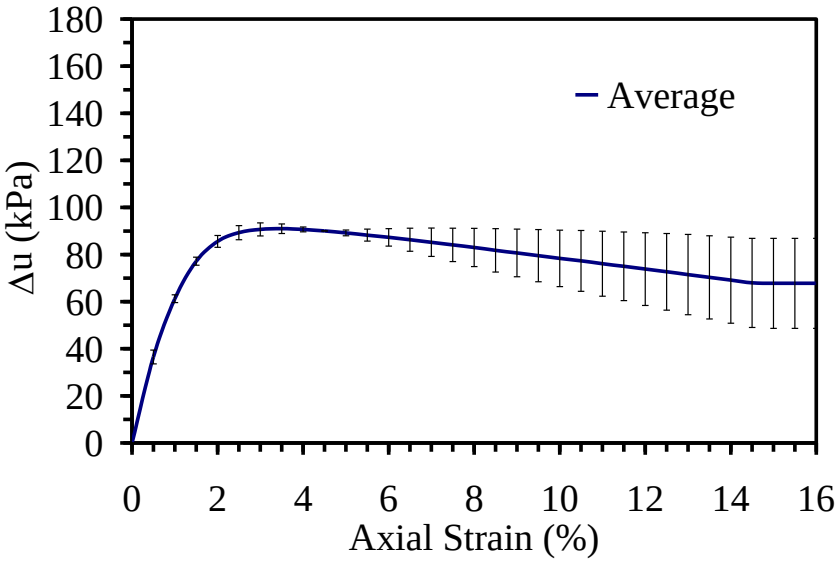

Figure 6.21: Average excess pore water pressure difference and error bars with axial strain for all triaxial compression tests performed on saturated Boulder clay at a time to 15% axial strain of 10 minute

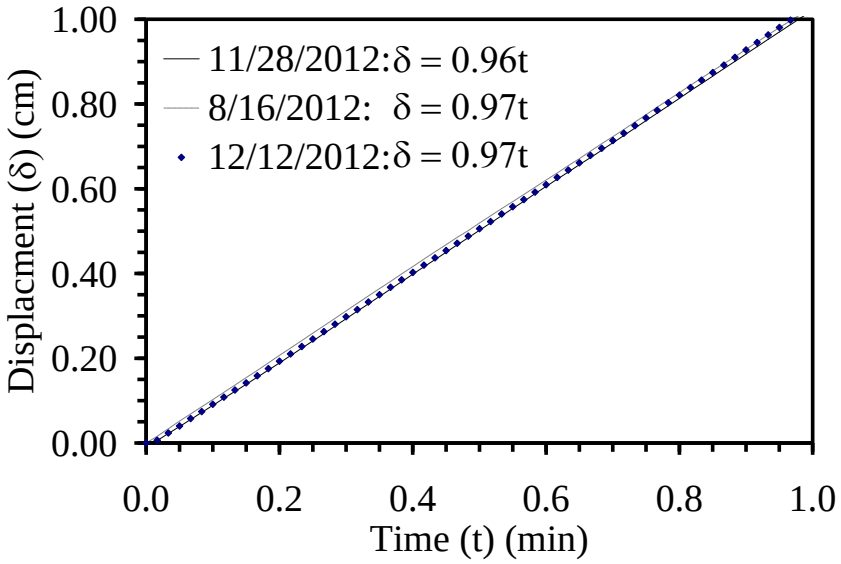

Figure 6.22: Axial displacement with time of testing for triaxial compression tests on saturated Boulder clay tests performed at a time to 15 % axial strain of 1 minute

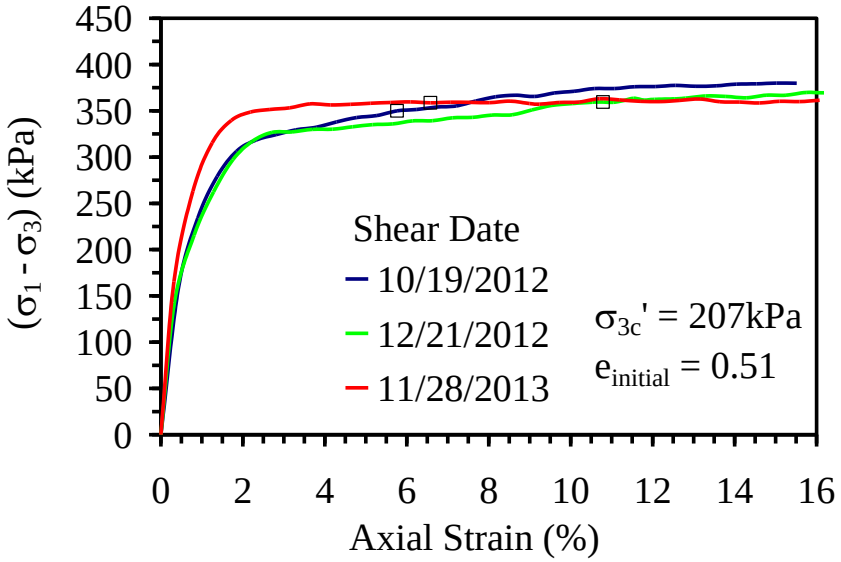

Figure 6.23: Principal stress difference with axial strain for triaxial compression tests on saturated Boulder clay tests performed at a time to 15% axial strain of 1 minute

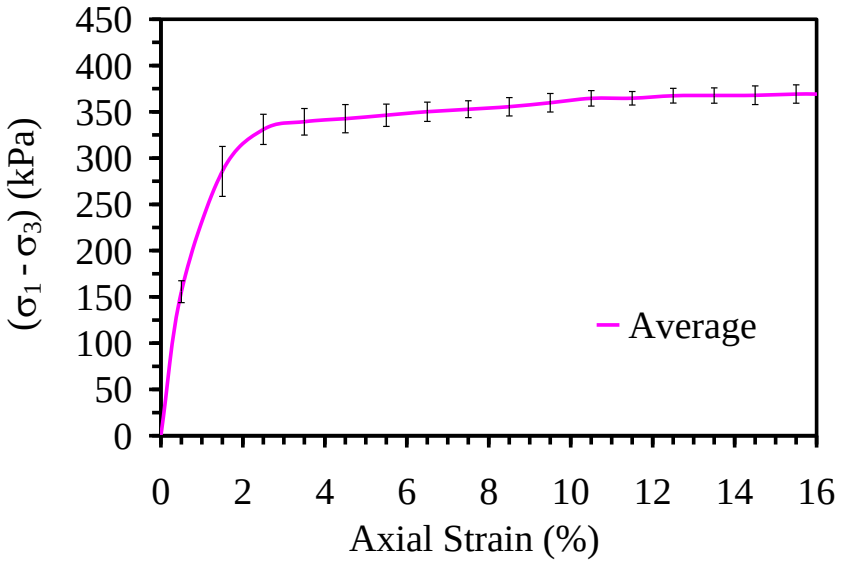

Figure 6.24: Average principal stress difference and error bars with axial strain for all triaxial compression tests performed on saturated Boulder clay at a time to 15% axial strain of 1 minute

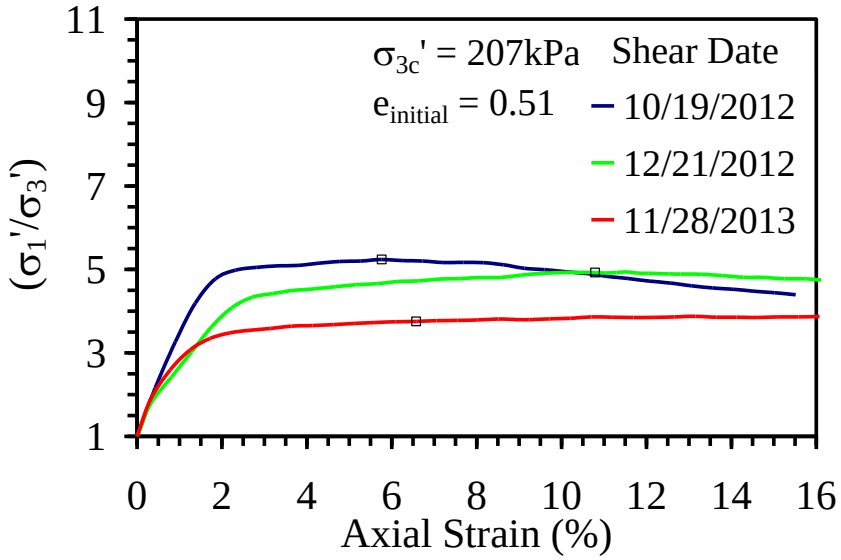

Figure 6.25: Principal stress ratio with axial strain for triaxial compression tests on saturated Boulder clay performed at a time to 15% axial strain of 1 minute

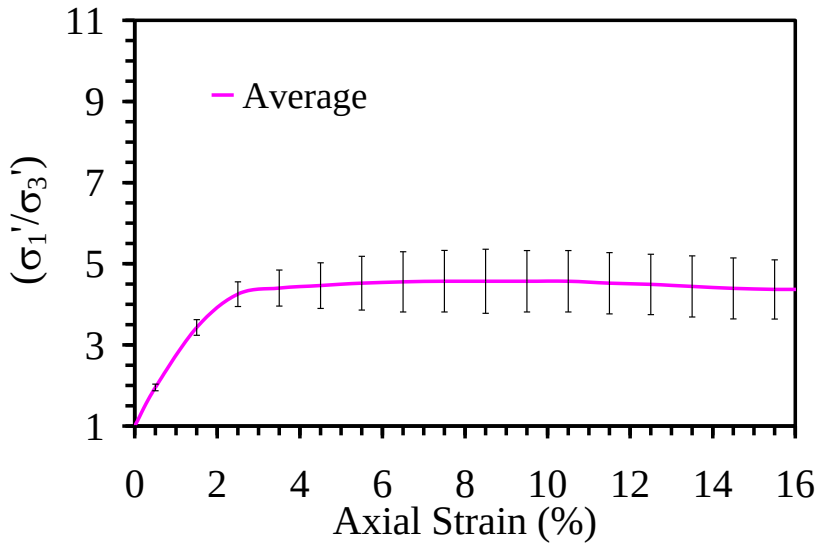

Figure 6. 26: Average principal stress ratio and error bars with axial strain for all triaxial compression tests performed on saturated Boulder clay at a time to 15% axial strain of 1 minute

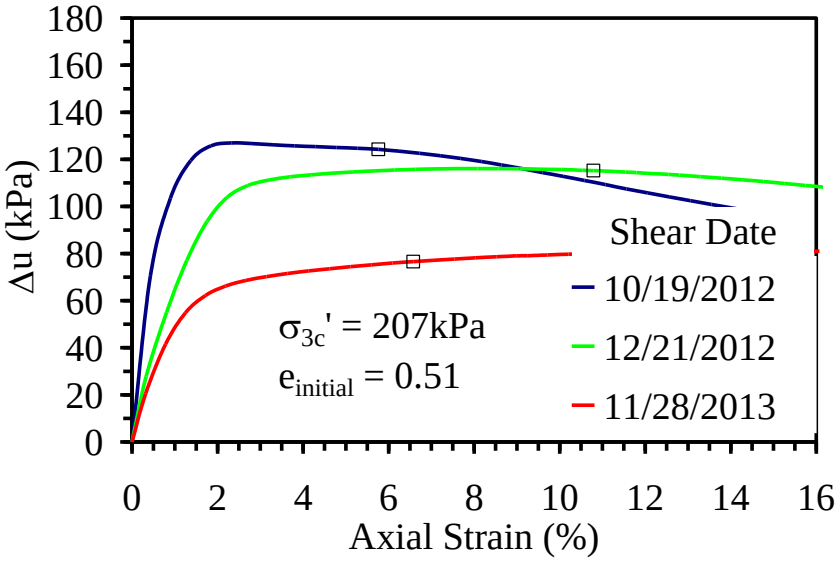

Figure 6.27: Excess pore water pressure with axial strain for triaxial compression tests on saturated Boulder clay performed at a time to 15% axial strain of 1 minute

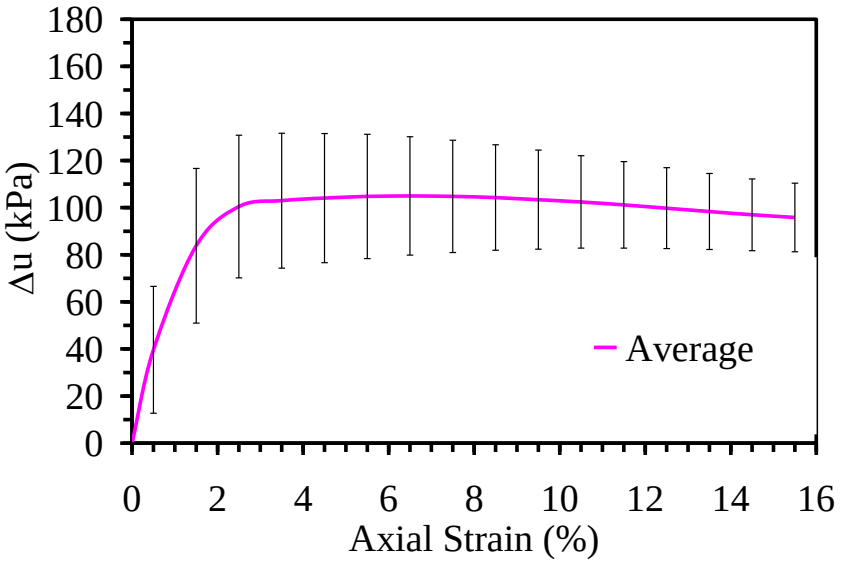

Figure 6.28: Average excess pore water pressure and error bars with axial strain for all triaxial compression tests performed on saturated Boulder clay at a time to 15% axial strain of 1 minute

6.4.2 Repeatability of Unsaturated Boulder Clay Tests

Figures 6.29 through 6.35 shows the axial displacement with time of testing, principal stress difference, average principal stress difference and error bars, principal stress ratio, average principal stress ratio and error bars, excess pore water pressure, and average excess pore water pressure and error bars with axial strain for multiple Boulder clay test with an applied matric suction of 34 kPa performed at a time to 15% axial strain of 1 minute.

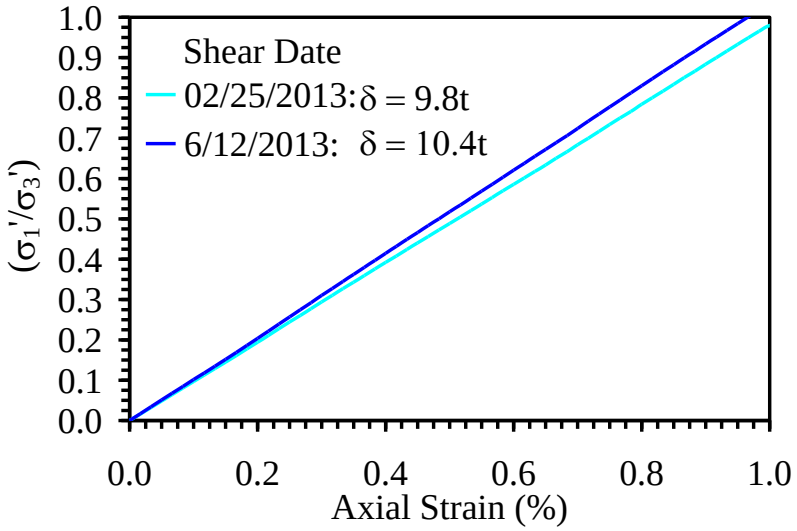

Figure 6.29: Axial displacement with time of testing for triaxial compression tests on unsaturated Boulder clay tests performed at a time to 15 % axial strain of 1 minute with an applied suction of 34 kPa

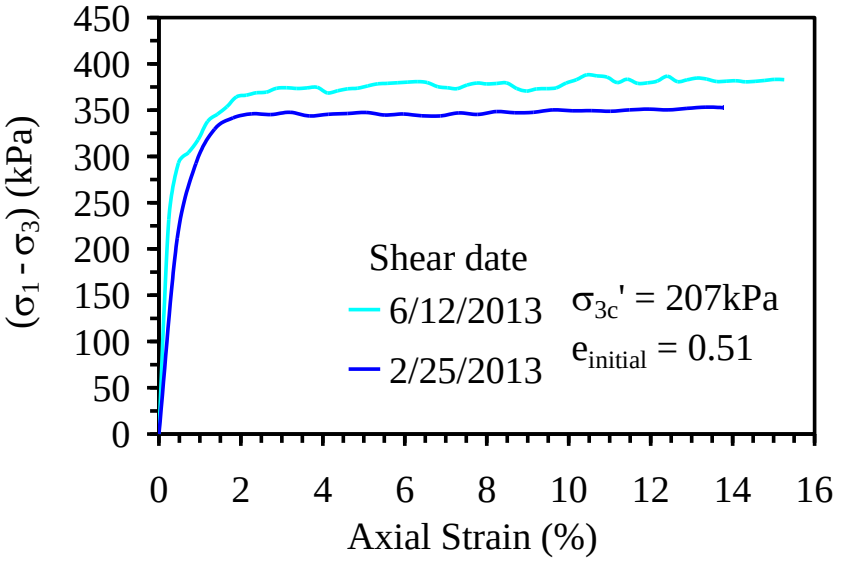

Figure 6.30: Principal stress difference with axial strain for triaxial compression tests on unsaturated Boulder clay tests performed at a time to 15% axial strain of 1 minute with an applied suction of 34 kPa

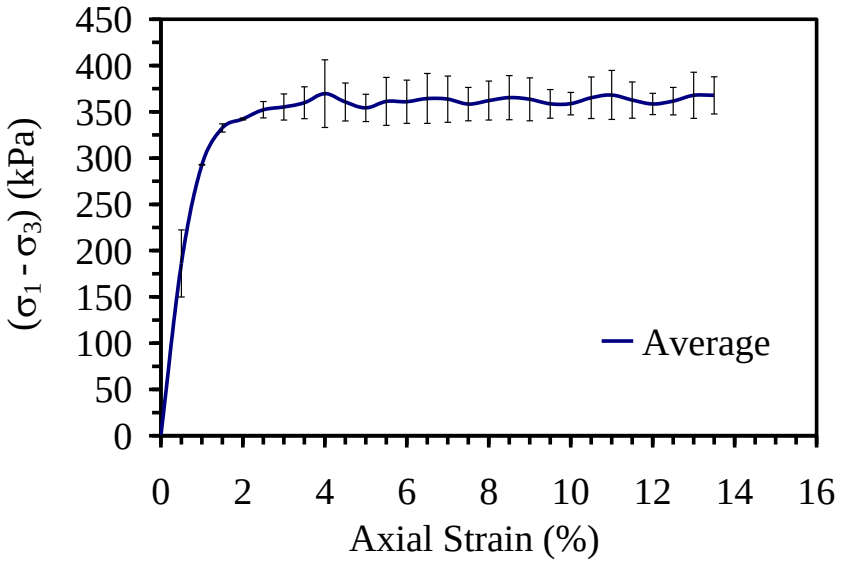

Figure 6.31: Average principal stress difference and error bars with axial strain for all triaxial compression tests performed on unsaturated Boulder clay at a time to 15% axial strain of 1 minute with an applied suction of 34 kPa

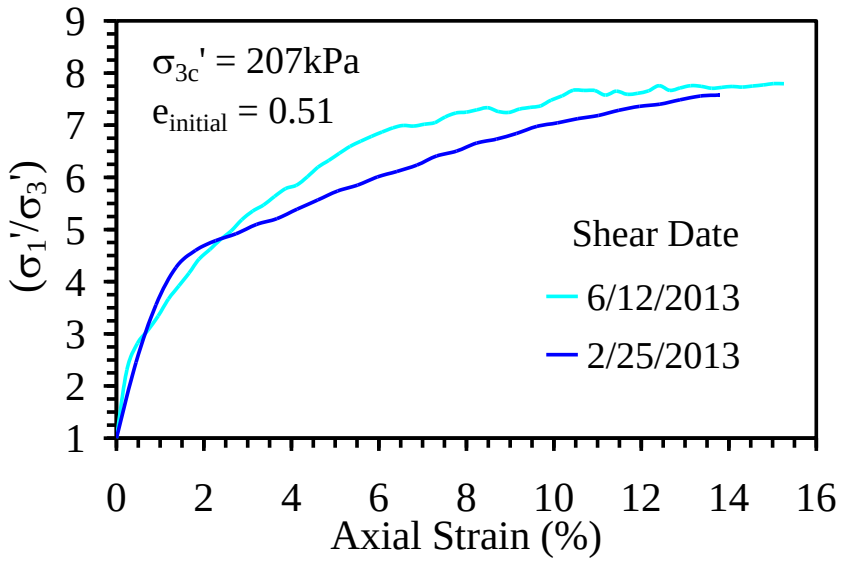

Figure 6.32: Principal stress ratio with axial strain for triaxial compression tests on unsaturated Boulder clay performed at a time to 15% axial strain of 1 minute with an applied suction of 34 kPa

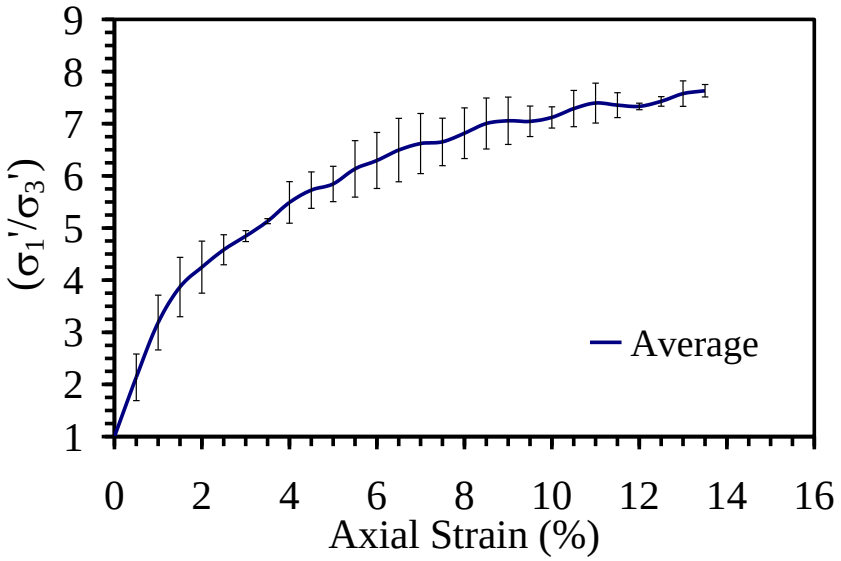

Figure 6.33: Average principal stress ratio and error bars with axial strain for all triaxial compression tests performed on unsaturated Boulder clay at a time to 15% axial strain of 1 minute with an applied suction of 34 kPa

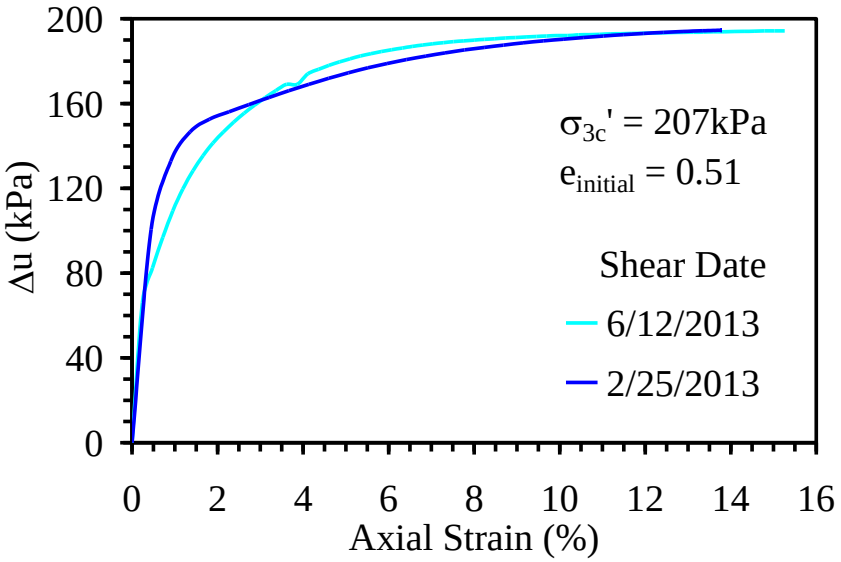

Figure 6.34: Excess pore water pressure with axial strain for triaxial compression tests on unsaturated Boulder clay performed at a time to 15% axial strain of 1 minute with an applied suction of 34 kPa

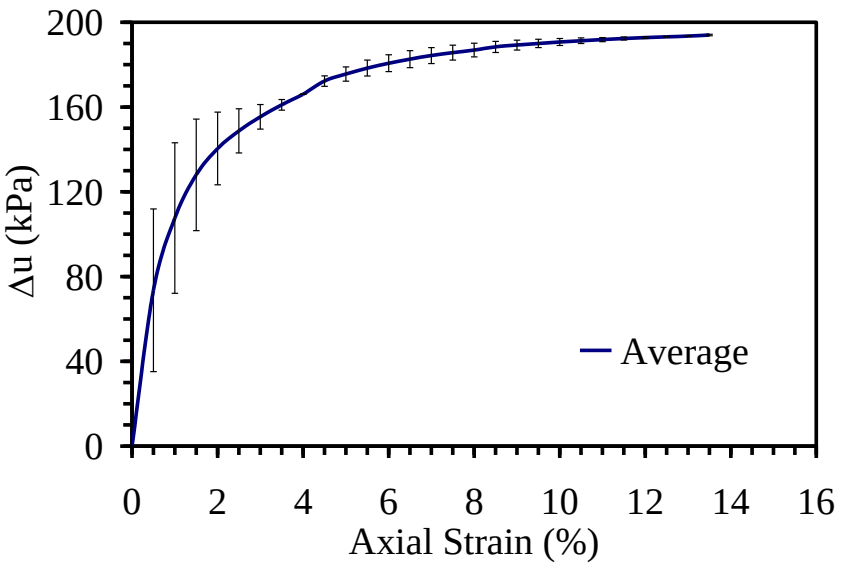

Figure 6.35: Average excess pore water pressure with axial strain for all triaxial compression tests performed on unsaturated Boulder clay at a time to 15% axial strain of 1 minute with an applied suction of 34 kPa

7.0 Analysis

This chapter presents the analysis of results for triaxial compression tests on Mason sand and Boulder clay. The first section analyzes the results for saturated and dry Mason sand tests. The second section analyzes the results for saturated and unsaturated CU tests as well as the unsaturated UU tests performed on Boulder clay.

7.1 Analysis of Mason Sand Results

7.1.1 Analysis of Saturated Mason Sand Results

The shear strength at failure for stress path tangency and maximum principal stress difference criterion are plotted versus axial strain rate in Figure 7.1 and time to reach 15% axial strain in Figure 7.2. The shear strength of Mason sand during undrained shearing increases on average by 33% per log cycle increase in strain rate using stress path tangency (SPT) failure criterion and about 11% per log cycle increase in strain rate using maximum principal stress difference (MPSD) failure criterion. These values were determined by calculating the percent increase in shear strength between each increase in strain rate and then taking an average.

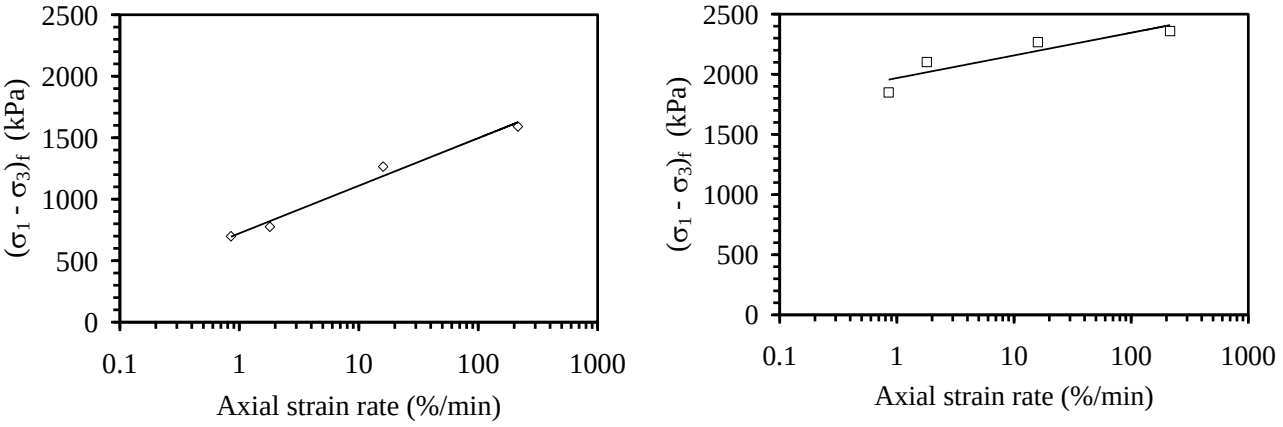

Figure 7.1: Variation of principal stress difference at failure with axial strain rate for triaxial compression tests on saturated Mason sand using (a) Stress path tangency failure criterion; and (b) Maximum principal stress difference failure criterion

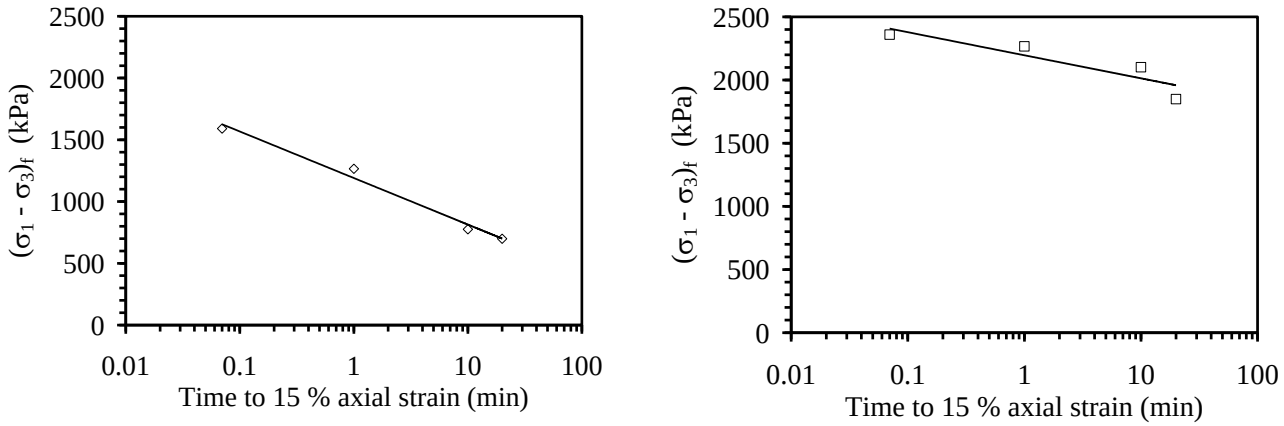

Figure 7.2: Variation of the principal stress difference at failure with the time to reach 15 % axial strain for triaxial compression tests performed on saturated Mason sand using the: (a) Stress path tangency failure criterion; and (b) Maximum principal stress difference failure criterion

The values of excess pore water pressure at the failure points defined using both failure criterions are plotted versus axial strain rate in Figure 7.3 and time to 15% axial strain in Figure 7.4. If failure is defined using the SPT failure criterion as in Figures 7.3(a) and 7.4(a), it is clear that the shear strength increases with increasing axial strain rate while the excess pore water pressure decreases with increasing axial strain rate. This observation indicates that as the soil is sheared at higher rates, the rate of dilation is also increasing. Subsequently, as the sand particles are forced to roll over each other and dilate at faster rates, larger suction will occur in the pore water between the particles and thus larger negative excess pore water pressures will be generated. The numerical values at failure for important parameters are summarized in Table 7.1 using the stress path tangency criterion and Table 7.2 using the maximum principal stress difference criterion. A summary of the values of the slope of the principal stress difference at failure with axial strain rate and percent increase in shear strength (principal stress difference) per log-cycle increase in strain rate is provided in Table 7.3.

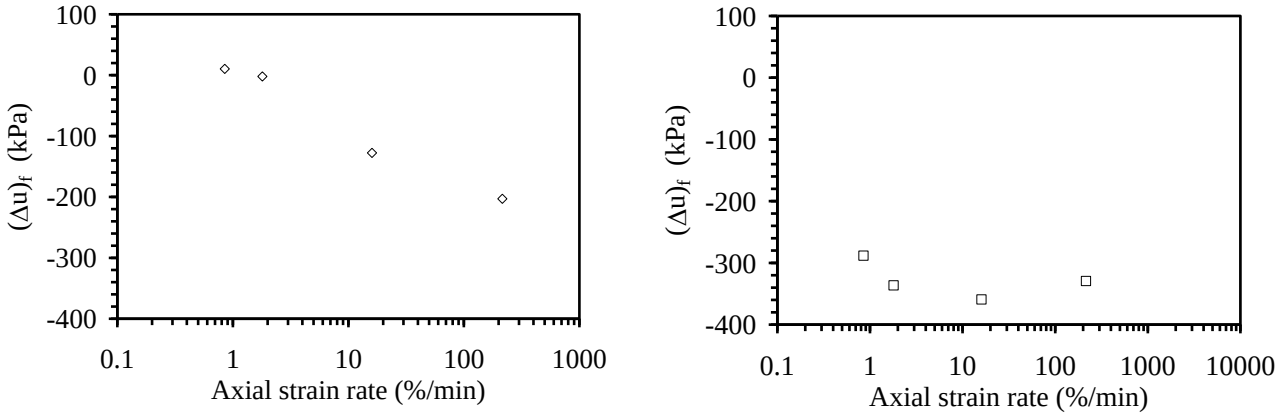

Figure 7.3: Variation of excess pore water pressure at failure with strain rate for triaxial compression tests performed on saturated Mason sand using the: (a) Stress path tangency failure criterion; and (b) Maximum principal stress difference failure criterion

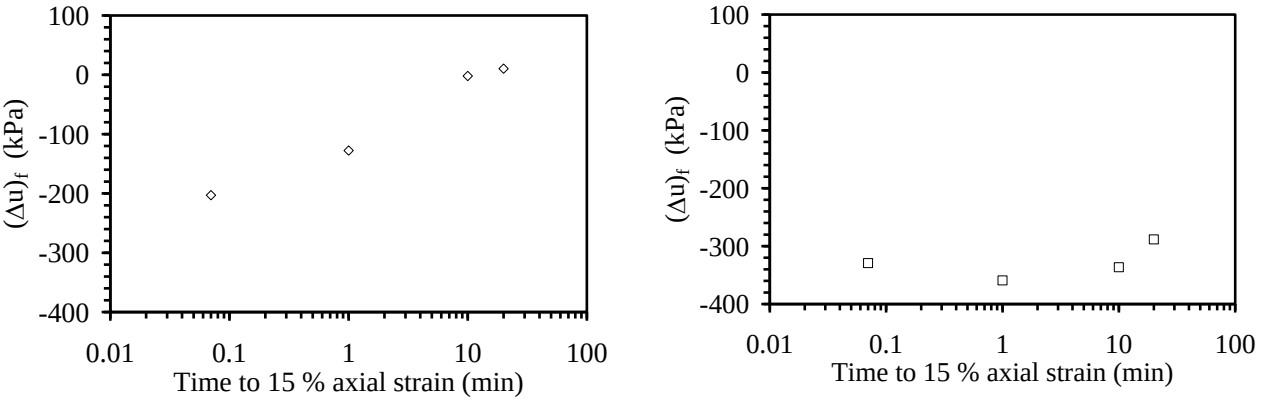

Figure 7.4: Variation of excess pore water pressure at failure with time to reach 15 % axial strain for triaxial compression tests performed on saturated Mason sand using the: (a) Stress path tangency failure criterion; and (b) Maximum principal stress difference failure criterion

Table 7.1: Summary of axial strain, effective confining pressure, excess pore water pressure, principal stress ratio and principal stress difference at failure determined using stress path tangency failure criterion for Mason sand.

Time to 15% axial strain (min)	Shearing Rate (mm/min)	Strain Rate (%/min)	ε_f (%)	σ_{3f}' (kPa)	Δu_f (kPa)	$(\sigma'_1/\sigma'_3)_f$	$(\sigma_1-\sigma_3)_f$ (kPa)
20.0	1.2	0.9	2.8	184.3	10.3	4.79	698.7
10.0	2.5	1.8	2.0	199.3	-2.1	4.89	775.6
1.0	28.0	16.0	2.8	334.6	-127.7	4.78	1265.33
0.1	367.0	215.0	3.4	409.8	-202.96	4.88	1590.67

Table 7.2: Summary of axial strain, effective confining pressure, excess pore water pressure, principal stress ratio and principal stress difference at failure determined using maximum principal stress difference failure criterion for Mason sand

Time to 15% axial strain (min)	Shearing Rate (mm/min)	Strain Rate (%/min)	ε_f (%)	σ_{3f}' (kPa)	Δu_f (kPa)	$(\sigma_1'/\sigma_3')_f$	$(\sigma_1-\sigma_3)_f$ (kPa)
20.0	1.2	0.9	10.2	483.0	-288.3	4.83	1848.7
10.0	2.5	1.8	7.9	533.7	-336.4	4.83	2101.5
1.0	28.0	16	6.9	566.2	-359.3	5.00	2266.6
0.1	367.0	215	7.2	536.2	-329.4	5.4	2359.0

Table 7.3: Summary of the log-linear slope of the principal stress difference with axial strain rate and average percent increase of the principal stress difference at failure per log cycle increase in strain rate for triaxial compression tests on saturated Mason sand

SPT		MPSD	
Log-linear slope	Average % increase in strength per log cyle of strain rate	Log-linear slope	Average % increase in strength per log cyle of strain rate
168	33	81.8	11

7.1.2 Analysis of Dry Mason Sand Results

The SPT failure points from Figure 5.8 are plotted as a function of strain rate in Figure 7.5. It is clear that the trend line is horizontal, indicating no relationship between axial strain rate and the shear strength of dry Mason sand.

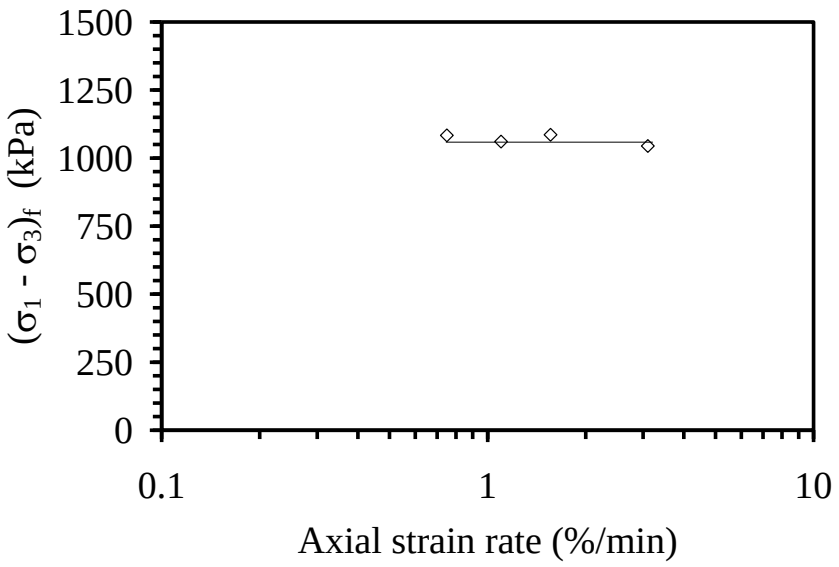

Figure 7.5: Variation of shear strength at failure with axial strain rate for triaxial compression tests performed on dry Mason sand

The principal stress ratio at failure marked in Figure 5.9 is plotted versus applied axial strain rate in Figure 7.6. As with the behavior of the shear strength at failure with increasing axial strain rate, there is no notable difference between the maximum principal stress ratio and axial strain rate. This observation indicates that the angle of internal friction, ϕ', does not change with increasing strain rate based upon the following equation

$$(\frac{\sigma_1'}{\sigma_3'})_{max} = \tan^2(1 + \frac{\phi_f'}{2}) \qquad 7.1$$

where $(\sigma_1'/\sigma_3')_{max}$ is the maximum principal stress ratio and ϕ_f' is the angle of internal friction at failure.

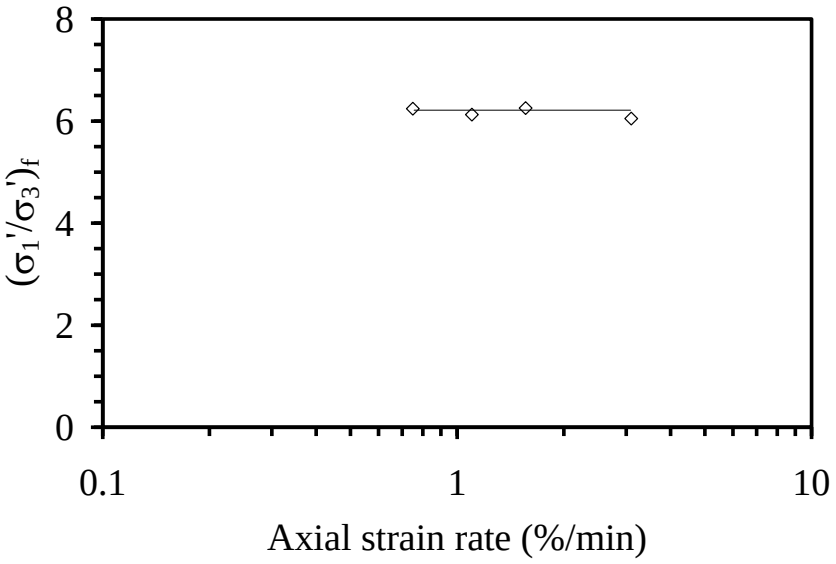

Figure 7.6: Variation of the principal stress ratio at failure with axial strain rate for triaxial compression tests performed on dry Mason sand

Traditionally, dilation is defined as the change in volumetric strain over the change in axial strain. The dilation surrounding SPT failure of dry Mason sand with axial strain rate is shown Figure 7.7(a). The dilation of the dry sand increases with axial strain rate, indicating that there is actually less dilation occurring as the specimen is sheared at higher rates. The rate of dilation for the purpose of this study was defined as the average change in dilation with time surrounding the point of SPT failure. For the dry mason sand tests, this was taken to between axial strains of approximately 2-6 % (See Figure 5.10). The rate of dilation is plotted versus the axial strain rate in Figure 7.7(b). From this figure, it is apparent that there is a distinct decrease in the rate of dilation with increasing strain rate. Even though the actual dilation of the sand at failure increases with increasing strain rate, the decreasing dilation rate with increasing axial strain rate implies that as the soil is sheared at faster rates, the particles are also pulling apart (dilating) at a faster rate. A summary of the axial strain, volumetric strain, principal stress ratio, shear strength and dilation rate at failure for the four different tests is provided in Table 7.4.

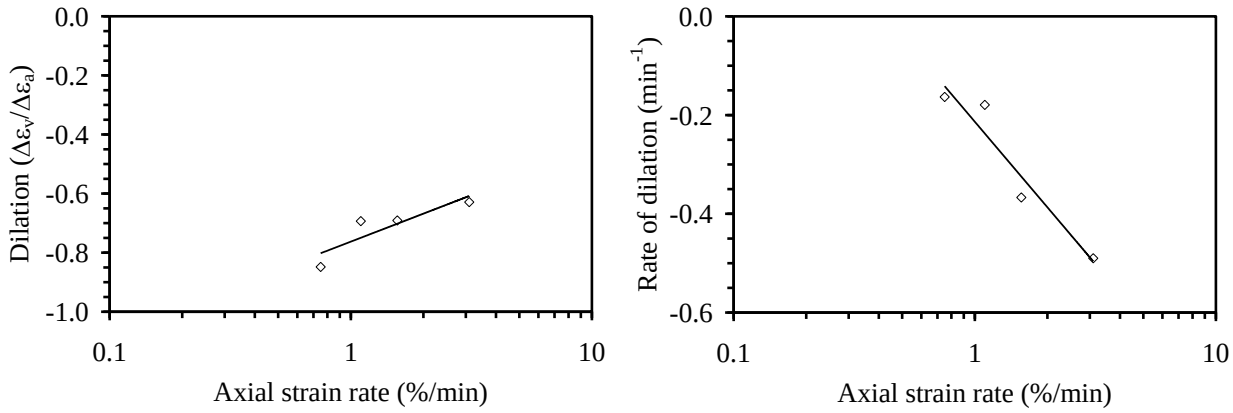

(a) (b)

Figure 7.7: Variation of the rate of dilation with axial strain rate for triaxial compression tests performed on dry Mason sand

Table 7.4: Summary of dry Mason sand shear strength parameters at failure

Time to 15 % axial strain (min)	Strain Rate (%/min)	ε_{af} (%)	ε_{vf} (%)	$(\sigma'_1/\sigma'_3)_f$	$(\sigma_1.\sigma_3)_f$ (kPa)	Dilation (%/%)	Rate of dilation (min^{-1})
20.0	0.75	4.4	-2.5	6.24	1084	-0.85	-0.16
15.0	1.10	5.2	-1.7	6.13	1061	-0.69	-0.18
10.0	1.56	4.9	-1.71	6.25	1086	-0.69	-0.37
5.00	3.10	4.9	-1.36	6.05	1044	-0.63	-0.49

7.1.3 Analysis of Results from Tests on Dry and Saturated Mason Sand

As discussed earlier and shown through Equation 7.1, the friction angle, ϕ', is directly related to the principal stress ratio. Accordingly, the principal stress ratio reflects the mobilization of friction in the triaxial specimen without the effects of excess pore water pressure on the stress state in the soil specimen. The use of the principal stress ratio as a failure criterion permits the effective shear strength parameters to be defined from an undrained test. If SPT failure criterion is used, then the shear failure of the specimens actually occurs at the point of maximum mobilization of friction that corresponds to the maximum principal stress ratio (see Equation 7.1). The friction angles calculated for the tests on dry and saturated Mason sand performed at

axial strain rates of 0.75 %/min and 1.56 %/min are shown in Table 7.4. When comparing the friction angles for both dry and saturated sand tests under the same moisture condition but different strain rates, the friction angle does not change with strain rate. However, the average friction angle of 46.4° for the dry tests is greater compared to the average friction angle for the saturated tests of 41.4°. This observation is further illustrated by comparing the stress paths taken during shear. The stress paths for the four tests in modified Mohr-Coulomb stress space are shown in Figure 7.8. It is apparent from this figure that the failure envelope for the dry sand is steeper than the failure envelope of the saturated sand. A summary table for the four tests detailing the time to 15% axial strain, axial strain rate, moisture condition, axial strain at SPT failure, principal stress ratio at SPT failure, principal stress difference at SPT failure and angle of internal friction is provided in Table 7.5.

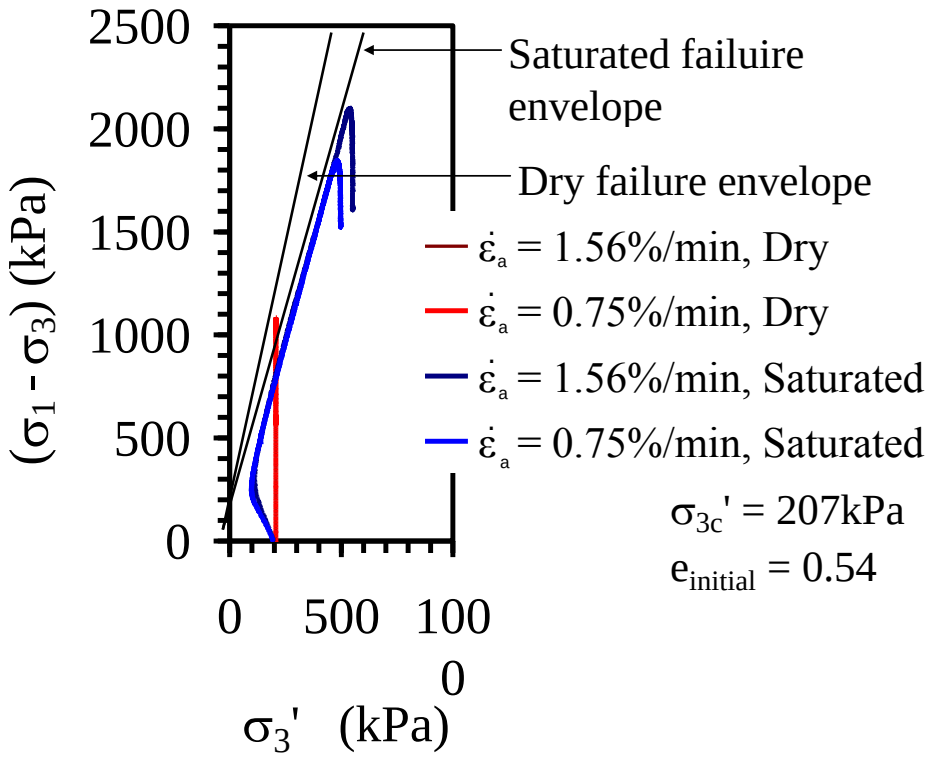

Figue 7.8: Stress paths in Modified Mohr-Coulomb stress space for triaxial compression tests performed on dry and saturated Mason sand at axial strain rates of 0.75 %/min and 1.56 %/min

Table 7.5: Summary of failure parameters for dry and saturated Mason sand tests performed at axial strain rates of 0.75 %/min and 1.56 %/min

Time to 15% axial strain (min)	Strain rate (%)	Moisture condition	ε_a (%)	σ_1'/σ_3'	$(\sigma_1 - \sigma_3)$ (kPa)	ϕ' (degrees)
20	0.77	dry	4.39	6.24	1084	46.4
20	0.75	saturated	3.31	4.81	819	41.1
10	1.48	dry	4.87	6.25	1086	46.4
10	1.50	saturated	2.46	4.97	1014	41.7

7.1.4 Discussion of Rate Effects on Mason Sand

Undrained, saturated triaxial tests on Mason sand show an increase in shear strength accompanied by a decrease in negative excess pore water pressures with increased strain rate. Drained, dry triaxial tests on Mason sand indicate that there is no correlation between greater shear strength and increased strain rate. However, it was also observed that the rate of dilation of dry Mason sand becomes more negative (greater dilation) with increased strain rate. From these findings, it can be concluded that the increase in shear strength with increasing strain rate of the saturated sand is solely the consequence of greater negative excess pore water pressure generated during shearing. Furthermore, the greater negative excess pore water pressure is due to the sand dilating at greater rates with increased strain rate.

Comparison of dry, drained triaxial tests to saturated, undrained triaxial tests on Mason sand indicate that the friction angle of the sand increases slightly when the sand is sheared in dry conditions for tests run at 20 and 10 minutes time to 15 % axial strain (Figure 7.8). There are a number of possible reasons for the increase in friction angle of the dry sand. Lee et al. (1967) showed a decrease in shear strength and increase in friction angle between saturated and dry sand due to small fractures in the sand particles that were filled with a clay-like material. When the sand was saturated, the clay-filled fractures decreased the particle-to-particle friction and allowed sliding. As a result, the sand's friction angle and shear strength decreased.

Another reason could be the mineralogy of the sand particles. Horne and Deere (1962) performed direct shear tests on a number of different minerals to determine the coefficient of friction of the minerals under dry and wet conditions. From this investigation, it was found that the presence of water reduces the coefficient of friction between layered-lattice silicate minerals such as Mica. Thus, it is potentially possible that the silicate particles in the Mason sand could reduce the friction angle and shear strength in a saturated state.

7.2 Analysis of Tests on Boulder Clay

7.2.1 Analysis of Tests on Saturated Boulder Clay

The shear strength (principal stress difference) at failure is plotted versus axial strain rate using stress path tangency criterion in Figure 7.9(a) and maximum principal stress difference criterion in Figure 7.9(b). The shear strength is plotted versus time to 15% axial strain in Figure 7.10(a) using stress path tangency criterion and Figure 7.10(b) using maximum principal stress difference criterion. From these figures, it is clear that the shear strength increases log-linearly with increasing strain rate or decreasing time to 15 % axial strain. The percent increase in shear strength for the Boulder clay is 13.8% per log cycle using the stress path tangency failure criterion and 8.8% per log cycle using the maximum principal stress difference failure criterion. The observed increase in shear strength is consistent with previous studies conducted by Casagrande and Shannon (1948), Richardson and Whitman (1963) and Olson and Parola (1967). From these classic studies, it was found that for normally consolidated clay, the shear strength increased by 10% on average per log cycle increase in strain rate.

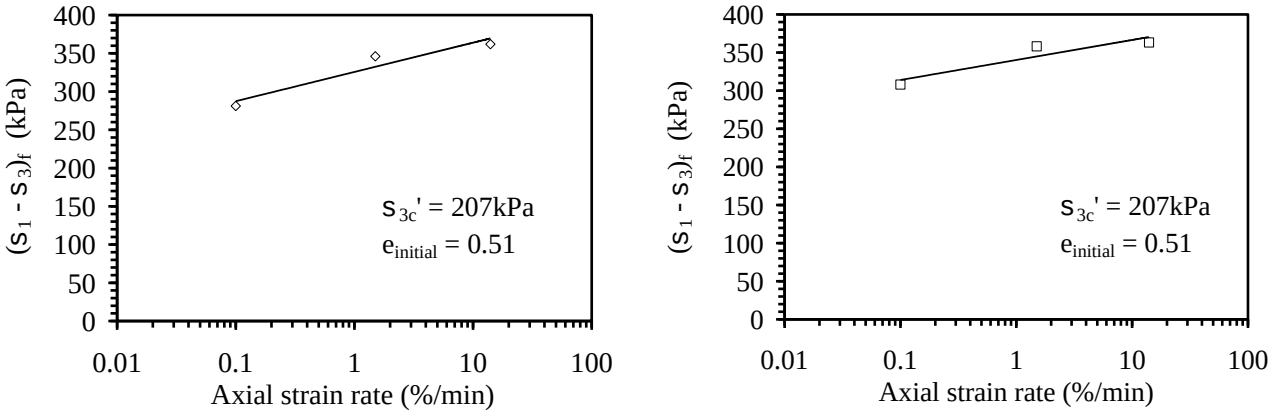

(a) (b)

Figure 7.9: Variation in undrained shear strength with axial strain rate for triaxial compression tests performed on saturated Boulder clay using the: (a) Stress path tangency failure criterion; and (b) Maximum principal stress difference failure criterion

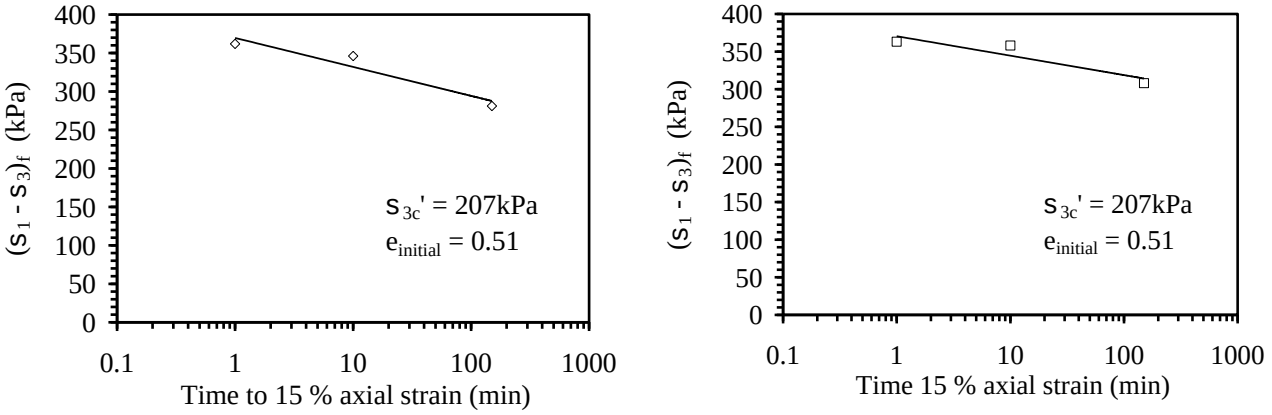

(a) (b)

Figure 7.10: Variation in undrained shear strength with time to 15% axial strain for triaxial compression tests performed on saturated Boulder clay using the: (a) stress path tangency failure criterion; and (b) maximum principal stress difference failure criterion

The excess pore water pressure versus axial strain rate using stress path tangency failure criterion is shown in Figure 7.11(a) and using maximum principal stress difference failure criterion is shown in Figure 7.11(b). Similarly, the excess pore water pressure at failure is plotted versus time to 15 % axial strain using stress path tangency failure criterion in Figure 7.12(a) and maximum principal stress difference failure criterion in Figure 7.12(b). From Figure 7.11 and Figure 7.12, it is apparent that excess pore water pressure decreases with increased axial strain rate and decreased time to 15% axial strain indicating that the compacted specimens have a

dilative response during shear. Thus, rather than contracting during the load application, the soil at higher rates dilates as the clay particles are forced to roll and climb on top of each other.

This observation is consistent with studies conducted by Richardson and Whitman (1963), Lefebvre and Leboef (1987) and Zhu and Yin (2000). These studies found that for normally consolidated clay the shear strength increased with increasing strain rate, and this strength increase was accompanied by a decrease in excess pore water pressure. Thus, it is concluded that the increase in Boulder clay shear strength with increasing strain rate is due to an increase in effective stress caused by the decrease in the magnitude of excess pore water pressure. All important numerical values at failure using the stress path tangency and maximum principal stress difference failure criteria are provided in Tables 7.6 and 7.7. A summary of the values of the slope of the principal stress difference at failure with axial strain rate and percent increase in shear strength (principal stress difference) per log-cycle increase in strain rate is provided in Table 7.8.

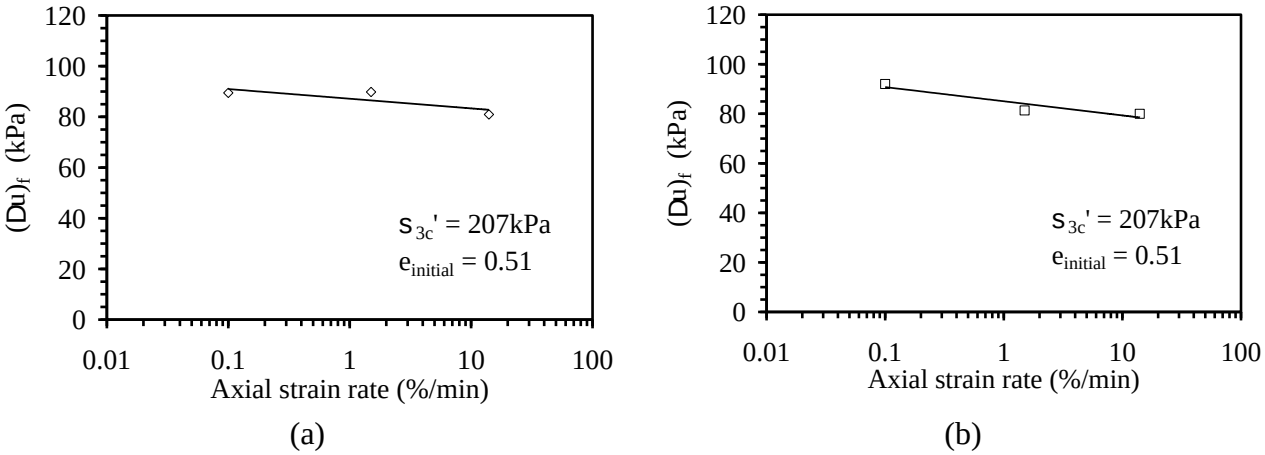

Figure 7.11: Variation in excess pore water pressure with axial strain rate for triaxial compression tests performed on saturated Boulder clay using the: (a) stress path tangency failure criterion; and (b) maximum principal stress difference failure criterion

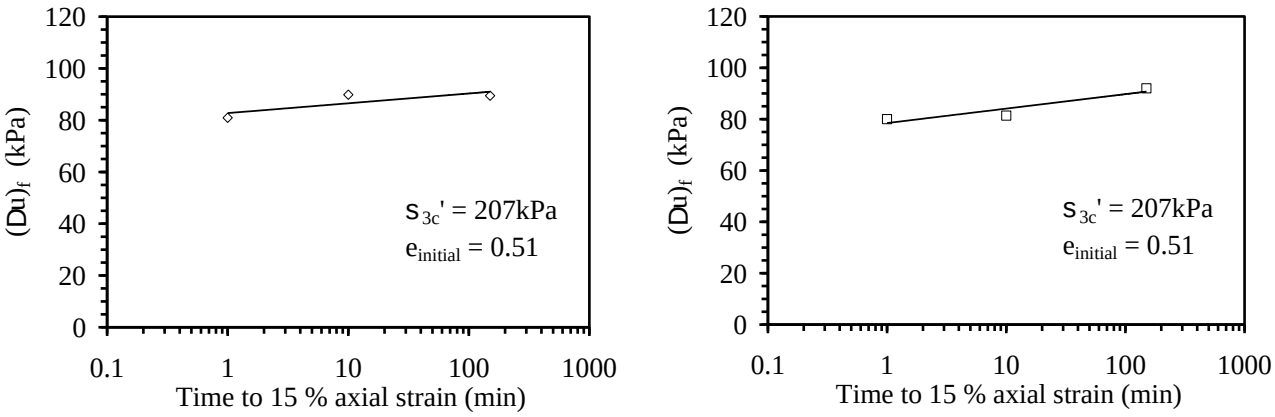

Figure 7.12: Variation in excess pore water pressure with time to 15 % axial strain for triaxial compression tests performed on saturated Boulder clay using the: (a) stress path tangency failure criterion; and (b) maximum principal stress difference failure criterion

Table 7.6: Values at failure for Boulder clay using stress path tangency criterion to identify the point of failure

Time to 15% axial strain (min)	Shearing Rate (mm/min)	Strain Rate (%/min)	ε_f (%)	σ_{3f}' (kPa)	Δu_f (kPa)	$(\sigma'_1/\sigma'_3)_f$	$(\sigma_1-\sigma_3)_f$ (kPa)
150	0.0702	0.1	3.4	117.4	89.5	3.40	281.2
10	1.11	1.5	6.3	117.0	89.8	3.97	346.2
1.0	10.40	14.0	13.9	125.9	80.9	3.88	362.0

Table 7.7: Values at failure for Boulder clay using maximum principal stress difference failure criterion to identify the point of failure.

Time to 15% axial strain (min)	Shearing Rate (mm/min)	Strain Rate (%/min)	ε_f (%)	σ_{3f}' (kPa)	Δu_f (kPa)	$(\sigma'_1/\sigma'_3)_f$	$(\sigma_1-\sigma_3)_f$ (kPa)
150	0.0702	0.1	9.9	114.9	92.0	3.68	308.0
10	1.11	1.5	14.7	125.5	81.3	3.85	358.1
1.0	10.40	14.0	10.7	126.9	80.0	3.86	363.2

Table 7.8: Summary of the log-linear slope of the principal stress difference with axial strain rate and average percent increase of the principal stress difference at failure per log cycle increase in strain rate for triaxial compression tests on saturated Boulder clay

SPT		MPSD	
Log-linear slope	Average % increase in strength per log cyle of strain rate	Log-linear slope	Average % increase in strength per log cyle of strain rate
16.6	13.8	81.8	8.8

The explanation for the increase in undrained shear strength with increasing effective stress is further confirmed by investigating the variation of the principal stress ratio with strain rate shown in Figure 7.13 and the stress paths taken during shear Figure 7.14. The principal stress ratio at failure using either SPT criterion or MPSD criterion changes very little with increasing strain rate. This finding implies that the angle of internal friction does not change with increased strain rate (Equation 7.1). Figure 7.14 shows the stress paths taken by the three tests in modified Mohr-Coulomb stress space, $(\sigma_1 - \sigma_3)$ versus effective minor principal stress (σ_3'). From the figure, it can be seen that the failure of the specimens occurs at points that lie on the same line or failure envelope as the static tests. This observation indicates that the increase in strength is due to a factor other than changes in the failure envelope such as increases in the angle of internal friction or apparent cohesion. Rather, the failure envelope remains unchanged, and the shear strength at failure increases because of an increase in effective stress due to a decrease in pore water pressure.

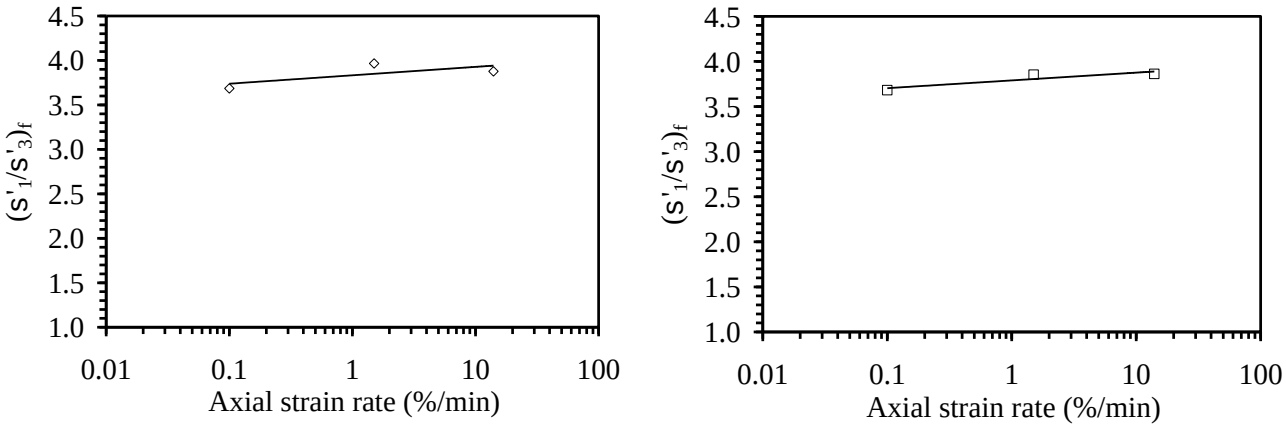

Figure 7.13: Variation of the principal stress ratio at failure versus axial strain rate for Boulder clay defined using: (a) stress path tangency failure criterion; and (b) maximum principal stress difference failure criterion

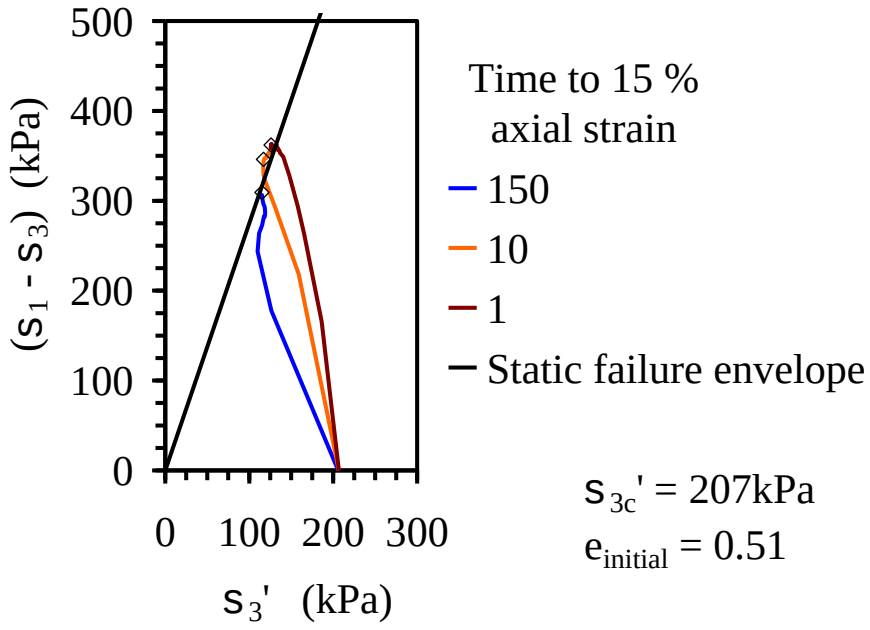

Figure 7.14: Stress paths for Boulder clay performed at times to an axial strain of 15% in 150, 10 and 1 minute. The failure point of each test defined using the stress path tangency criterion is identified with a hollow diamond.

Another helpful parameter for understanding the effect of strain rate on saturated Boulder clay is the initial tangent modulus. This parameter is defined as the ratio of the change in stress (principal stress difference) to axial strain from 0 and 1%. The relationship between the initial tangent modulus and increased strain rate is shown in Figure 7.15. The average increase in the initial tangent modulus was 15% per log cycle increase in strain rate. The increase in the tangent modulus indicates an increase in the initial stiffness of the Boulder clay.

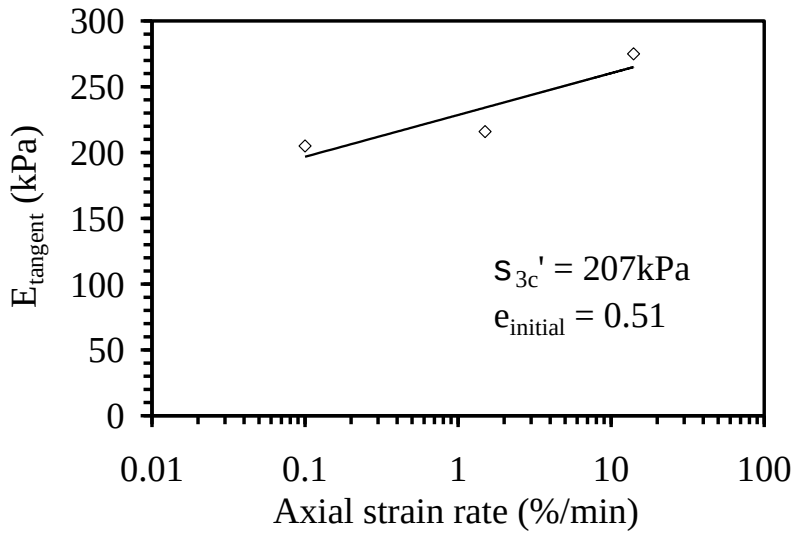

Figure 7.15: Variation of the initial tangent modulus with axial strain rate for triaxial compression tests performed on saturated Boulder clay

7.2.2 Analysis of Unsaturated Boulder Clay Results

The undrained shear strength (principal stress difference) defined by the stress path tangency failure criterion for saturated and unsaturated Boulder clay is plotted versus logarithm of strain rate in Figure 7.16. The shear strength for this soil in both saturated (0 kPa suction) and unsaturated conditions increases log-linearly with increasing strain rate. The slope of the strength versus strain rate plot decreases from the 0 and 34 kPa tests to 140 kPa tests indicating a decrease in the percentage of strength increase with strain rate as the soil becomes dryer. This could be due to decreased hydraulic conductivity which would inhibit the flow of water away from the shear plane as well as collapse of air voids during shear.

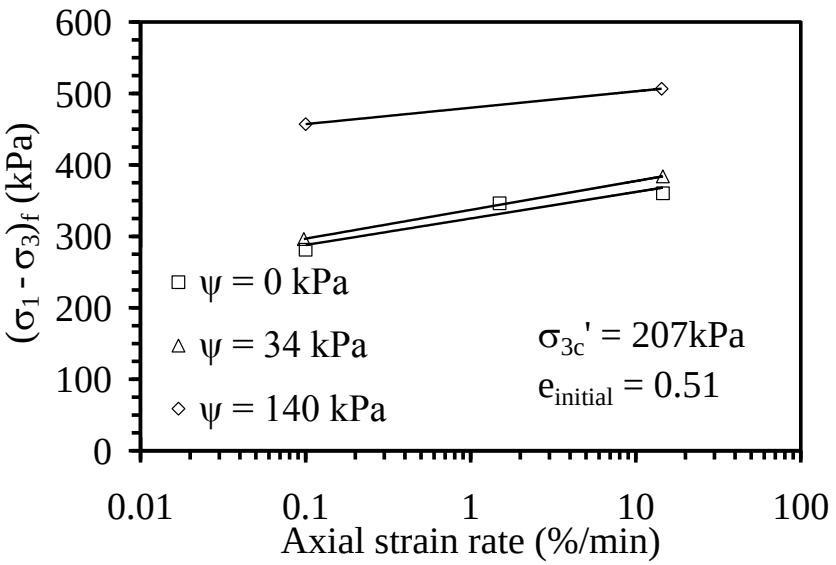

Figure 7.16: Variation in shear strength at the point of SPT failure with axial strain rate for triaxial compression tests on Boulder clay with suction values of 0, 34 and 140 kPa

Excess pore water pressures at the point of shear failure defined are shown in Figure 7.17. The excess pore water pressure at failure is positive for both saturated and unsaturated Boulder clay. As noted in the previous section, the excess pore water pressure at failure decreased with increasing axial strain rate for saturated clay. One interesting observation is that the pore water pressure at failure at a matric suction of 34 kPa is greater than both the tests with suctions of 0 and 140 kPa. This trend was confirmed with a second repeat test (see Chapter 6, Section 6.4.2). An explanation for this behavior may be that the decrease in hydraulic conductivity with suction may affect the rate at which water can redistribute in the specimen due to the excess pore water pressure generated on the shear plane.

Even in saturated specimens, the rate at which water redistributes spatially in the specimen in response to changes in excess pore water pressure on the shear plane will affect the magnitude of excess pore water pressure measured in the specimen (Gibson and Henkel 1955). The closer the specimen is to undrained conditions the greater the potential for generating excess pore water

pressures. At slower shearing rates, more time is available to allow for inter-pore redistribution of pore water throughout the specimen away from the shearing plane. However, at faster shearing rates, there may not be sufficient time available for this flow to occur.

The reason that the specimens at matric suction values of 34 and 140 kPa had different magnitudes of excess pore water pressure is that the specimen with a suction of 34 kPa had a much higher degree of saturation. For low suctions where the degree of saturation is high, it is possible that relatively high excess pore water pressures have the potential to be generated since the water may not be able to move away from the shear plane as easily due to decreased hydraulic conductivity. As the matric suction increases, rearrangement of the particles into predominantly air-filled pores spaces will not generate as high a magnitude of pore water pressures as observed with the fast tests with a matric suction of 140 kPa. Nonetheless, the specimen at a suction of 140 kPa still had a change in pore water pressure at the bottom of the specimen similar to that of the saturated specimen.

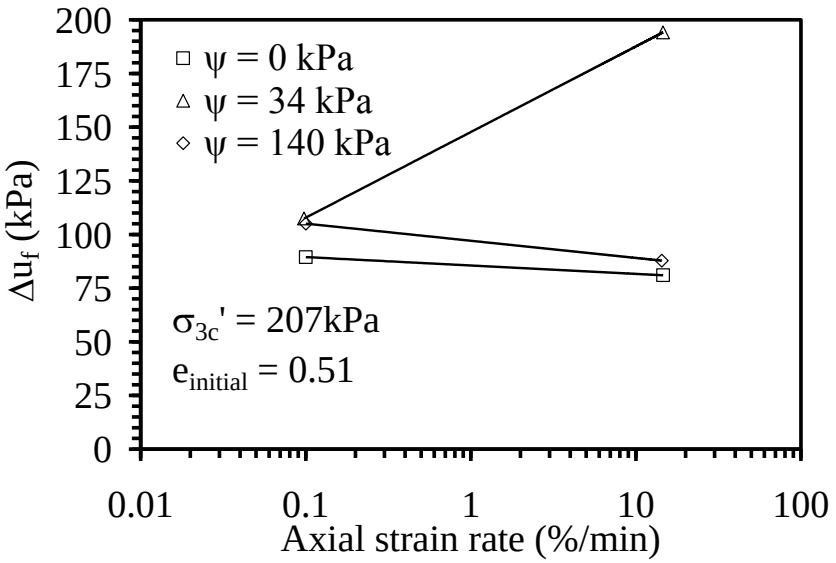

Figure 7.17: Variation of excess pore water pressure at that point of SPT failure with axial strain rate for triaxial compression tests performed on Boulder clay with suction values of 0, 34, and 140 kPa

The shear strength at the point of stress path tangency failure for tests run at 150 and 1 minute times to 15% axial strain is shown in Figure 7.18 as a function of matric suction. From Figure 7.18, it is clear that there is an increase in shear strength with increasing matric suction. This behavior is possibly due to both the role of the initial matric suction that serves to increase the initial effective confining pressure on the specimen. Lu et al. (2010) developed a closed form solution for the effective stress in unsaturated soil defining the effective stress as a function of the net stress ($\sigma - u_a$) and suction stress (σ_s) as shown in Equation 7.2. The suction stress is defined for two different cases: where the matric suction ($u_a - u_w$) is less than zero (saturated case) shown in Equation 7.3 or were the matric suction is greater than zero (unsaturated case) shown in Equation 7.4. For the unsaturated case, the suction stress is a function of the matric suction and the van Genuchten (1980) SWRC parameters, α_{vG} and n_{vG}.

$$\sigma_3' = (\sigma_3 - u_a) - \sigma_s \qquad 7.2$$

$$\sigma_s = -(u_a - u_w) \qquad (u_a - u_w) \leq 0 \qquad 7.3$$

$$\sigma_s = -S_e(u_a - u_w) = -\frac{(u_a - u_w)}{(1 + [\alpha_{vG}(u_a - u_w)]^{n_{vG}})^{(n_{vG}-1)/n_{vG}}} \qquad (u_a - u_w) \geq 0 \qquad 7.4$$

After determining the suction stress for a particular matric suction, the predicted shear strength and principal stress difference can be calculated by inserting the effective stress calculated with Equation 7.2 into the following equation:

$$(\sigma_1 - \sigma_3)_f = \sigma_3' \frac{2\sin(\phi')}{1 - \sin(\phi')} \qquad 7.5$$

The principal stress difference values predicted using Equation 7.5 are plotted in Figure 7.18 as a function of matric suction with hollow squares, while the measured principal stress difference values are plotted with hollow circles. A good correlation between the measured and predicted values of the principal stress difference at failure.

The excess pore water pressure versus matric suction is shown in Figure 7.19. From the results shown in this figure, it is apparent that there is a change in excess pore water pressure during shear for the unsaturated specimens, which increased with axial strain rate for the unsaturated specimens. This behavior is different from that of the saturated specimens.

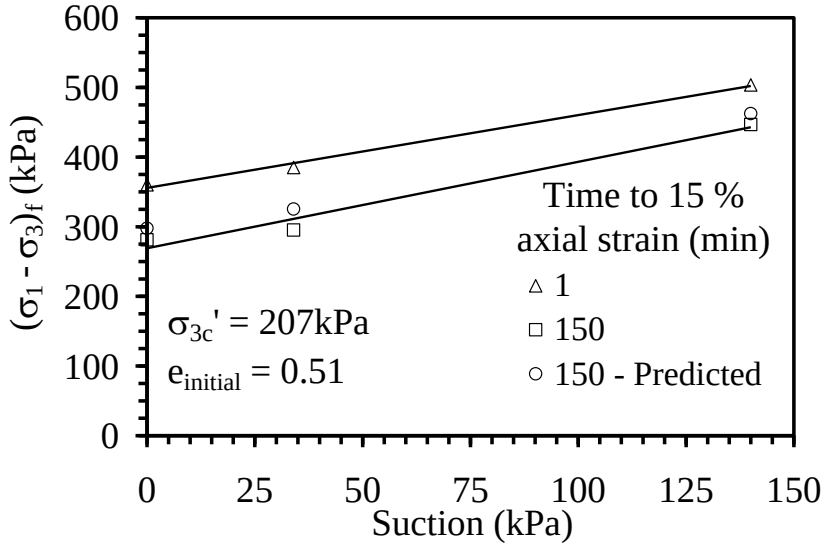

Figure 7.18: Variation of the undrained shear strength with suction for triaxial compression test performed on Boulder clay sheared to an axial strain of 15% axial in 150 minutes and 1 minute

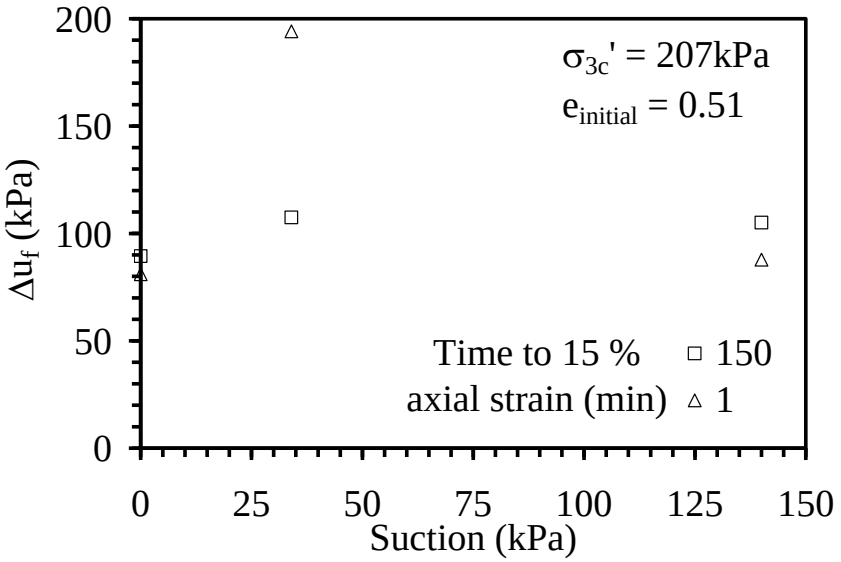

Figure 7.19: Variation of excess pore water pressure with suction for triaxial compression tests performed on Boulder clay sheared to an axial strain of 15 % axial strain of 150 minutes and 1 minute

7.2.3 Analysis of Results from Unconsolidated Undrained Tests

The undrained shear strength from UU triaxial tests at different compaction water contents versus axial strain rate is shown in Figure 7.20. From this figure it is clear that there is an increase in the shear strength with both increased strain rate and decreased water content. This observation is consistent with tests performed on consolidated undrained Boulder clay tests under unsaturated conditions where the degree of saturation and hence the water content was decreased due to the applied matric suction. The rate of increase in shear strength indicated by an increase in the slope of the best fit line shown in Figure 7.20 also increases with decreased suction. This behavior is opposite from that observed in unsaturated CU Boulder clay tests. Summary tables for all UU Boulder clay tests are provided in Tables 7.7 through 7.10.

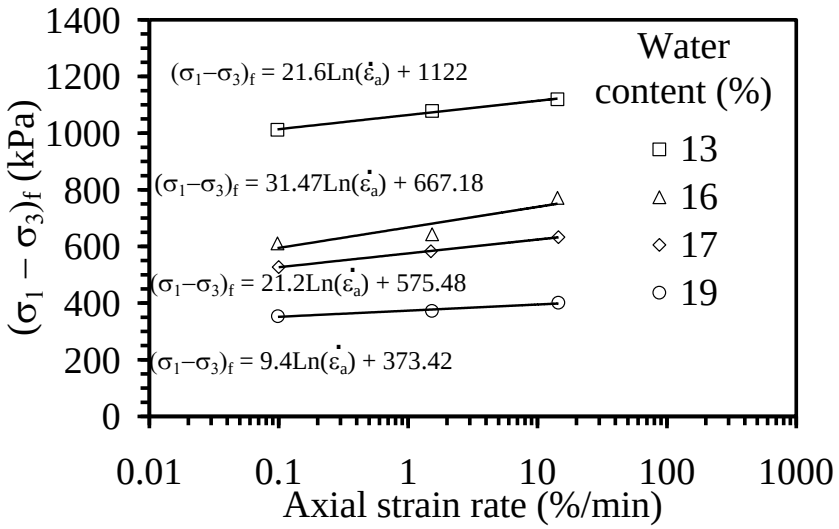

Figure 7.20: Variation in shear strength with axial strain rates for specimens prepared under compaction water contents of 13, 16, 17, and 19%

Table 7.9: Summary of testing details at failure for specimens prepared at an average compaction water content of 19.5 %

Time to 15% axial strain (min)	Strain rate (%/min)	w_f (%)	S_f (%)	e_f	$(\sigma_1-\sigma_3)_f$ (kPa)	$(\varepsilon_a)_f$ (%)
150	0.1	19.6	99.8	0.52	354	14.8
10	1.5	19.5	99.9	0.52	373	14.1
1	14.5	19.2	98.0	0.53	401	11.5

Table 7.10: Summary of testing details at failure for specimens prepared at an average compaction water content of 17 %

Time to 15% axial strain (min)	Strain rate (%/min)	w_f (%)	S_f (%)	e_f	$(\sigma_1-\sigma_3)_f$ (kPa)	$(\varepsilon_a)_f$ (%)
150	0.1	17.2	89.4	0.52	527	15.2
10	1.5	17.2	90.8	0.51	583	14.8
1	14.5	16.9	86.3	0.53	633	11.3

Table 7.11: Summary of testing details at failure for specimens prepared at an average compaction water content of 16 %

Time to 15% axial strain (min)	Strain rate (%/min)	w_f (%)	S_f (%)	e_f	$(\sigma_1-\sigma_3)_f$ (kPa)	$(\varepsilon_a)_f$ (%)
150	0.1	15.9	85.2	0.54	611	13.2
10	1.5	16.5	81.3	0.55	643	15.0
1	14.3	16.4	86.1	0.51	772	9.7

Table 7.12: Summary of testing details at failure for specimens prepared at an average compaction water content of 13 %

Time to 15% axial strain (min)	Strain rate (%/min)	w_f (%)	S_f (%)	e_f	$(\sigma_1-\sigma_3)_f$ (kPa)	$(\varepsilon_a)_f$ (%)
150	0.1	13.7	76.1	0.53	1011	8.8
10	1.5	12.7	67.3	0.51	1078	10.7
1	14.3	12.4	64.6	0.52	1119	6.8

7.2.4 Discussion of Rate Effects on Boulder Clay

The results from this study show that for saturated compacted clay there is an increase in undrained shear strength with increasing strain rate. Furthermore, the increase in undrained shear strength can be attributed to a decrease in excess pore water pressure and an increase in effective stress. The shear strength of unsaturated compacted clay also increases with increased strain rate as well as increases in matric suction. The pore water pressures at failure measured for unsaturated specimens at higher strain rates showed unexpected behavior, as they increased to a

value greater than that for saturated conditions for low suction magnitudes, then decreased to a value similar to saturated conditions for higher suction magnitudes.

Gibson and Henkel (1954) emphasized the fact that during drained triaxial compression testing of cohesive materials, the ability to maintain a truly drained state is impossible. However, they developed an equation based upon consolidation theory to determine the time to 15% axial strain at which a specimen should be sheared to maintain a "drained" state where the generated excess pore water pressure is low enough to not significantly affect drained shear strength. In other words, if shearing is slow enough then excess pore water pressures dissipate at a steady rate. This time to 15% axial strain provides the maximum rate that a soil specimen can be sheared that will lead to "drained" conditions. The equation Gibson and Henkel (1954) used to represent the time to 15% axial strain that should ensure a certain percentage of dissipation of excess pore water pressure during is given below:

$$t_{15\%} = \frac{H^2}{\eta c_v (1 - U_f)} \qquad 7.7$$

where $t_{15\%}$ is the time to 15% axial strain in a drained CD test corresponding to a given desired degree of consolidation, U_f, used to represent the percentage of dissipation of excess pore water pressure. A value of $U_f = 0.95$ is typically used in drained triaxial testing (ASTM D7181). H is the drainage distance (1/2 of the specimen height), c_v is the coefficient of consolidation for a given stress range, and η is a parameter that is based on the type of drainage.

For the first part of this analysis, the time to 15% axial strain actually used on the unsaturated Boulder clay specimens was compared to the calculated time to 15% axial strain developed by Gibson and Henkel (1954) with undrained conditions ($U_f = 0$). The value of η for this analysis was taken to be 3, which indicates drainage is allowed only at the specimen boundaries. It should also be noted that c_v is not only a function of a specific effective stress range but also hydraulic

conductivity and consequently suction. The values of c_v were determined through consolidation tests performed on a compacted, saturated specimen of Boulder clay and on a specimen of Boulder clay with an initial suction of 40 kPa. If the height of drainage is taken to be half the height of the specimen, the theoretical time to 15% axial strain ($t_{15\%}$) in an undrained case where the pore water pressure is allowed to equilibrate throughout the specimen can be calculated by setting the desired degree of saturation equal to zero.

The specific parameters and calculated values of $t_{15\%}$ are given in Table 7.11. The calculated time to 15% axial strain to allow for redistribution of the excess pore water pressure using the equation of Gibson and Henkel (1954) was 130 minutes for the saturated case and 325 minutes for the unsaturated case with an initial matric suction of 34 kPa. The actual time to 15% axial strain used in the unsaturated tests was 150 minutes. Comparing the calculated time to 15% axial strain ($t_{15\%}$) to the actual testing time to 15% axial strain (t_{test}) shows that for the saturated case the actual time testing time is greater than the calculated time indicating that adequate time was allowed for redistribution of the pore water pressure during undrained shearing. However, when comparing the actual testing time to the calculated time to 15% axial strain for the unsaturated soil, the calculated time was greater than the actual time used during shearing of the specimens. These results indicate that adequate time may not have been given to allow for complete redistribution pore water pressure during shear. This may have caused the greater magnitude of pore water pressure measured in the unsaturated specimens than in the saturated specimens (Figure 7.17).

Table 7.13: Calculation parameters and theoretical time to equilibration of pore water pressure in an undrained triaxial specimen ($U_f = 0$)

	ψ: 0 kPa	ψ: 34 kPa
H (m)	0.036	0.036
η	3	3
c_v (m^2/s)	5.26E-08	2.16E-08
k (m/sec)	7.0E-10	1.6E-11
$t_{15\%}$ (sec)	8013	19492
$t_{15\%}$ (min)	134	325
t_{test} (min)	150	150

The second part of this analysis focuses on the ability for water to flow away from the shear plan during faster shearing rates. Previous studies have shown that the excess pore water pressure is greatest along the shear plane. Huang et al. (1991) performed piezocone penetration tests on overconsolidated clay where the pore water pressure water was measured at various distances away from the piezocone. It was noted that the greatest initial pore water pressure occurred at the point of penetration along the shear zone and then decreased as the radial distance away from the piezocone increased.

In the case of triaxial compression tests, the greater increase in excess pore water pressure generated along the shear plane could create internal pressure gradients, which would consequently cause localized flow of water within the specimen. This conceptual idea is illustrated in Figure 7.21.

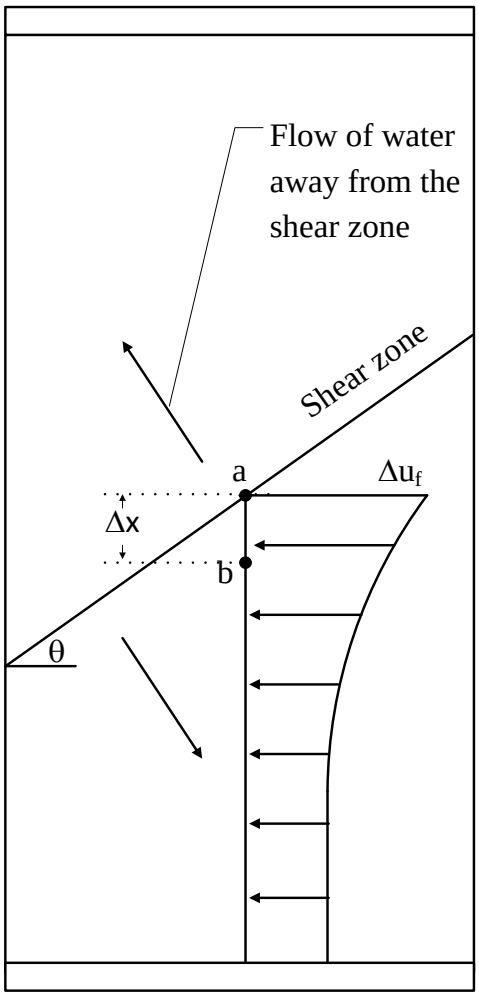

Figure 7.21: Idealized schematic of the localized shear zone pore water pressure response during triaxial compression

The time for water to flow (t_{flow}) some arbitrary distance, Δx, during testing between points a and b shown in Figure 7.21 can be calculated with the following equation:

$$t_{flow} = \frac{\Delta x}{v} = \frac{\Delta x}{ki} \qquad 7.8$$

where Δx is the length traveled by water subject to increased pressure gradient caused by shearing of the specimen and v is the flow velocity defined as the product of the hydraulic conductivity, k and the hydraulic gradient, i. The hydraulic gradient is defined as the change in hydraulic head, Δh, over the length traveled, Δx. The change in head from points *a* to *b* is defined as the sum of the change in pressure head and elevation head. Assuming that at the instance the

load is applied the change in pressure along the shear zone is equal to the excess pore water pressure and the change in the elevation head is equal to Δx. With these assumptions, the hydraulic gradient can be calculated as follows:

$$i = \frac{h_e + h_p}{\Delta x} = \frac{\Delta x + \frac{\Delta u}{\gamma_w}}{\Delta x} \qquad 7.9$$

where γ_w is the unit weight of water. Substituting Equation 7.9 into Equation 7.8, the time for water to flow from points *a* to *b* for a given a change in excess pore water pressure can be determined as follows:

$$t_{flow} = \frac{\Delta x^2}{k(\Delta x + \frac{\Delta u}{\gamma_w})} \qquad 7.10$$

The value of Δx was determined by setting t_{flow} equal to 60 seconds (the time used for the fastest shearing of Boulder clay) and solving for Δx using Equation 7.10. Δu was assumed to be the excess pore water pressure at SPT failure measured at the boundary of the specimen for the saturated Boulder clay test performed at a time to 15% axial strain of 1 minute. Realizing that a value of Δx is much smaller than $\Delta u/\gamma_w$, Equation 7.5 reduces to the following:

$$t_{flow} = \frac{\Delta x^2}{k(\frac{\Delta u}{\gamma_w})} \qquad 7.11$$

This time was calculated using the hydraulic conductivity for saturated specimens determined using the flow pump technique discussed in Section 3.3.9, and using the hydraulic conductivity of unsaturated specimens at a suction value of 34 kPa determined using the HCF presented in Section 3.3.9.

If the time required for a drop of water to flow away from the shear zone is greater than or nearly equal to the time required to equilibrate the pore water pressure using the equation of

Gibson and Henkel (1954) in fully drained conditions (U_f = 0.95) over the same time period, the inability of the water to flow away from the shear zone could potentially create a build-up of excess pore water pressure. This possibility is particularly likely for unsaturated soils where the hydraulic conductivity decreases exponentially with suction even though the degree of saturation could still be is relatively high. Table 7.12 shows the parameters and calculated values for a time to 15% axial strain of 1 minute using the equation of Gibson and Henkel (1954) (U_f = 0.95) and the time for a particle of water to flow a distance of Δx during a testing time of 1 minute.

From Tables 7.12 the time required to dissipate excess pore pressure at zero suction is nearly equal to the time for water to flow a distance Δx away from the shear zone. However, the time to dissipate the excess pore water pressure at 34 kPa suction is greater than the physical time for flow away from the shear zone. It is possible that other un-measurable factors, such as localized dilation, localized contraction, or collapse of air voids, also contribute to the generation of excess pore pressures. Accordingly, it seems reasonable to believe that the reduced ability for water to flow away from the shear zone could greatly affect the measured excess pore water pressure at the boundary of the specimen.

Table 7.14: Calculation parameters and theoretical time for water to flow away from the shear zone during triaxial compression

	ψ: 0 kPa	ψ: 34 kPa
H (m)	0.00062	0.00013
η	3	3
Δu (kPa)	90	180
Δx (m)	0.00062	0.00013
c_v (m^2/s)	5.26E-08	2.16E-08
k (m/sec)	7.0E-10	1.6E-11
$t_{15\%}$ (min)	0.81	0.09
t_{flow} (min)	1.00	0.98

8.0 Conclusions

8.1 Conclusions from Triaxial Compression Tests on Mason Sand

The following conclusions can be drawn from the experimental evaluation of the behavior of Mason sand during triaxial compression tests performed at different degrees of saturation and different shearing rates:

- An increase in undrained shear strength with increasing strain rate of 33% using SPT failure criterion was observed for saturated sand specimens. This rate of increase is solely the consequence of greater negative excess pore water pressure generated due to greater dilation during shearing.
- Drained, dry triaxial tests on Mason sand indicate that there is no correlation between greater shear strength and increasing strain rate. This confirms that excess pore water pressure generation is the cause of rate effects in the saturated sand.
- The rate of dilation of dry Mason sand was observed to becomes more negative (greater dilation) with increasing strain rate. The tendency for dilation was determined to be the main cause of the rate effects observed in saturated Mason sand tests, as they are related to the excess pore water pressure generation in the sand.
- Investigation of the effective stress paths from the undrained triaxial compression tests on saturated specimens indicates that the angle of internal friction does not change with increasing strain rate. However, the angle of internal friction was observed to be greater in tests on dry sand (46°) than in tests on saturated sand (41°). This was proposed to be due to mineralogical effects related to wetting of the particles.

8.2 Conclusions from Triaxial Compression Tests on Boulder Clay

The following conclusions can be drawn from the experimental evaluation of the behavior of Boulder clay during triaxial compression tests performed at different degrees of saturation and different shearing rates:

- For saturated, compacted clay an increase in undrained shear strength with increasing strain rate of 13.8% was observed. Similar to the sand, this trend was attributed to the observed decrease in excess pore water pressure with increasing strain rate, which corresponds to an increase in effective stress during shearing.
- Similar to the tests on Mason sand, investigation of the effective stress paths from the undrained triaxial compression tests on saturated Boulder clay indicates that the friction angle is not sensitive to the strain rate.
- The undrained shear strength of unsaturated compacted clay from CU triaxial tests was also observed to increase with increasing strain rate by 15% for tests performed with an initial matric suction of 34 kPa and 6% for tests performed with an initial suction of 140 kPa. The undrained shear strength was also observed to increase nonlinearly with matric suction.
- The excess pore water pressures at failure measured for unsaturated specimens at low suction magnitudes during tests at higher strain rates were greater than those measured for saturated conditions. However, the excess pore water pressures at failure measured for unsaturated specimens at high suction magnitudes were similar to those measured for saturated conditions. This change in excess pore water pressure with the matric suction was proposed to be due to a change in the time available for pore water pressures to equilibrate throughout the unsaturated specimens during undrained shearing.

- The undrained shear strength of unsaturated, compacted Boulder clay from UU triaxial compression tests was observed to increase by 5, 13, 10 and 6 for test performed with a target compaction water content of 13, 16.5, 17.5, and 19.5% respectively. The undrained shear strength was also observed to increase with decreasing compaction water content, consistent with the results from the CU triaxial compression tests.

References

ASTM D422. (2007). Standard Test Method for Particle-Size Analysis of Soils. Annual Book of ASTM Standards, American Society for Testing and Materials, West Conshohocken, NJ.

ASTM D698. (2003). Standard Test Method for Laboratory Compaction Characteristics of Using Standard Effort. Annual Book of ASTM Standards, American Society for Testing and Materials, West Conshohocken, NJ.

ASTM D854. (2002). Standard Test Method for Specific Gravity of Soil Solid by Water Pycnometer. Annual Book of ASTM Standards, American Society for Testing and Materials, West Conshohocken, NJ.

ASTM D2435. (2004). Standard Test Methods for One Dimensional Consolidation Properties of Soil Using Incremental Loading. Annual Book of ASTM Standards, American Society for Testing and Materials, West Conshohocken, NJ.

ASTM D2850. (1987). "Test method for unconsolidated undrained compressive strength of cohesive soils in triaxial compression." Annual Book of ASTM Standards, American Society for Testing and Materials, West Conshohocken, NJ.

ASTM D4318. (2000). Standard Test Method Liquid Limit, Plastic Limit and Plasticity Index of Soil. Annual Book of ASTM Standards, American Society for Testing and Materials, West Conshohocken, NJ.

ASTM D4546. (2003). Standard Test Methods for One Dimensional Swell or Settlement Potential of Cohesive Soils. Annual Book of ASTM Standards, American Society for Testing and Materials, West Conshohocken, NJ.

ASTM D4767. (2002). Standard Test Method for Consolidated Undrained Triaxial Compression Test for Cohesive Soils. Annual Book of ASTM Standards, American Society for Testing and Materials, West Conshohocken, NJ.

ASTM D 6836. (2003). Standard Test Methods for Determination of the Soil Water Characteristic Curve for Desorption using a Hanging Column, Pressure Extractor, Chilled Mirror Hygrometer, and/or Centrifuge. Annual Book of ASTM Standards, American Society for Testing and Materials, West Conshohocken, NJ.

ASTM D7181. (2011). Standard Test Method for Consolidated Drained Triaxial Compression Test for Soils, Annual Book of ASTM Standards, American Society for Testing and Materials, Easton, MD

ASTM D7664. (2010). Standard Test Methods for Measurement of Hydraulic Conductivity of Unsaturated Soils, Annual Book of ASTM Standards, Vol. 4.09, ASTM International, West Conshohocken, PA.

Bishop A. W. (1959). The principle of effective stress. Teknisk Ukeblad, 106, 859–863.

Bowden, F.P., & Tabor, D. (1956). Friction and Lubrication, Methuen & Co. Ltd., London.

Casagrande, A. & Shannon, W.L. (1948). "Stress-Deformation and Strength Characteristics of Soils under Dynamic Loads." In Proc. 2nd ICSMFE, Volume V, 29–34.

Casagrande, A. & Wilson, S.D. (1951). "Effect of rate of loading on the strength of clays and shales at constant water content." Géotechnique, 2(3), 251-263.

Delage, P., Romero, E., & Tarantino, A. (2008). Recent developments in the techniques of controlling and measuring suction in unsaturated soils. In *Proceedings 1st European Conference on Unsaturated Soils, Durham, CRC Press* (pp. 33-52).

Gibson, R.E. & Henkel, D.J. (1954). "Influence of duration of tests at constant rate of strain on measured "drained" strength." Géotechnique, 4(1), 6-15.

Horn, H.M., & Deere, D.U. (1962). "Frictional characteristics of minerals." Géotechnique, 12(4), 319-335.

Huang, A.B., Bunting, R.D., & Carney, T.C. (1991). "Piezoblade tests in a clay calibration chamber." Calibration Chamber Testing, 161-173.

Huy, N.Q., van Tol, A.F., & Holscher, P. (2006). Laboratory Investigation of the Loading Rate Effects in Sand. Report to TU-Delft.

Lefebvre, G. & LeBoeuf, D. (1987). "Rate effects and cyclic loading of sensitive clays." Journal of Geotechnical Engineering, 113, 476-489.

Leroueil, S. & Marques, M.E.S. (1996). "Importance of strain rate and temperature effects in geotechnical engineering." Measuring and Modeling Time Dependent Soil Behaviour. Proc. of the ASCE Convention, Number 61, Washington, DC, USA, pp. 1–60. ASCE.

Mitchell, J.K. (1964). "Shearing resistance of soils as a rate process." Journal of the Soil Mechanics & Foundations Division. 90(SM1), 29-61.

Mitchell, J.K. (1976). Fundamentals of Soil Behavior. John Wiley and Sons. NYC.

Olson, R.E. & Parola, J.F. (1967). "Dynamic shearing properties of compacted clay." In Proc. Int. Symposium on Wave Propagation and Dynamic Properties of Earth Materials. 173–182.

Olson, R.E. (1974). "Shearing strengths of Kaolinite, Illite, and Montmorillonite." Journal of the Geotechnical Engineering Division. ASCE. 100(GT11), 1215-1229.

Omidvar, M., Iskander, M., & Bless, S. (2012). "Stress-strain behavior of sand at high strain rates." International Journal of Impact Engineering. 49, 192-213.

Pereira, J.M., & De Gennaro, V. (2010). "On the time-dependent behaviour of unsaturated geomaterials." In Unsaturated Soils, Proc. Fifth Int. Conf. on Unsaturated Soils. Vol. 2, pp. 921-925.

Richardson, A.M. & Whitman, R.V. (1963). "Effect of strain-rate upon undrained shear resistance of a saturated remolded fat clay." Géotechnique, 13(4), 310–324.

Seed, H.B., Dunlop, P., & Lee, K.L. (1969). "Effect of transient loading on the strength of sand." Proc. of the 7th ICSMFE, 1, pp. 239-247.

van Genuchten, M.T. (1980). "A closed-form equation for predicting the hydraulic conductivity of unsaturated soils." Soil Science Society of America Journal. 44(5), 892-898.

Whitman, R.V. (1970). The Response of Soils to Dynamic Loadings; Report 26, Final Report. Massachusetts Institute of Technology, Cambridge, MA. Dept. of Civil Engineering.

Yamamuro, J.A., Abrantes, A.E., & Lade, P.V. (2011). "Effect of strain rate on the stress-strain behavior of sand." Journal of Geotechnical and Geoenvironmental Engineering. 137(12), 1169-1178.

Zhu, J. and Yin, J. (2000). "Strain-rate-dependent stress strain behavior of overconsolidated Hong Kong marine clay." Canadian Geotechnical Journal. 37, 1272-1282.